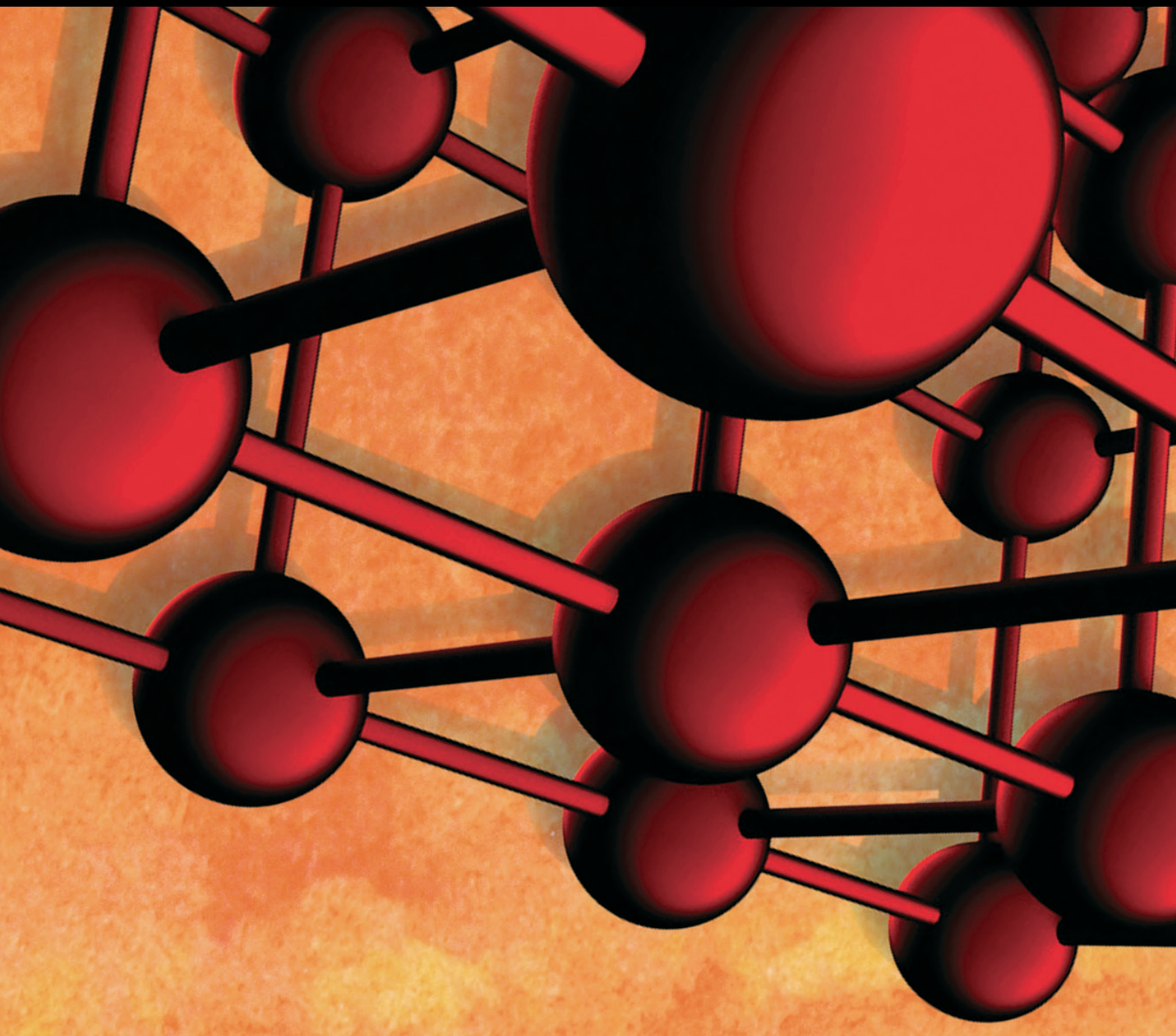


Advances in Materials Science and Engineering

Advanced Building Materials for Passive House and Energy Storage

Guest Editors: Sumin Kim, Jae D. Chang, and Jae-Han Lim





Advanced Building Materials for Passive House and Energy Storage

Advances in Materials Science and Engineering

Advanced Building Materials for Passive House and Energy Storage

Guest Editors: Sumin Kim, Jae D. Chang, and Jae-Han Lim



Copyright © 2017 Hindawi Publishing Corporation. All rights reserved.

This is a special issue published in “Advances in Materials Science and Engineering.” All articles are open access articles distributed under the Creative Commons Attribution License, which permits unrestricted use, distribution, and reproduction in any medium, provided the original work is properly cited.

Editorial Board

- Michael Aizenshtein, Israel
Jarir Aktaa, Germany
K. G. Anthymidis, Greece
Santiago Aparicio, Spain
Renal Backov, France
Markus Bambach, Germany
Amit Bandyopadhyay, USA
M. Barletta, Italy
Mikhael Bechelany, France
Bernd-Arno Behrens, Germany
Avi Bendavid, Australia
Jamal Berakdar, Germany
Jean-Michel Bergheau, France
Giovanni Berselli, Italy
Patrice Berthod, France
Susmita Bose, USA
H.-G. Brokmeier, Germany
Steve Bull, UK
Peter Chang, Canada
Daolun Chen, Canada
Gianluca Cicala, Italy
Gabriel Cuello, France
Narendra B. Dahotre, USA
João P. Davim, Portugal
Angela De Bonis, Italy
F. Delogu, Italy
S. B. Desu, USA
A. M. Díez-Pascual, Spain
Guru P. Dinda, USA
Yong Ding, USA
Nadka Tzankova Dintcheva, Italy
Frederic Dumur, France
Kaveh Edalati, Japan
Philip Eisenlohr, USA
Claude Estournès, France
Paolo Ferro, Italy
Massimo Fresta, Italy
G. Garcia-Belmonte, Spain
S. Garcia-Granda, Spain
C. Garcia-Mateo, Spain
Daniel Guay, Canada
Gianluca Gubbiotti, Italy
- Hiroki Habazaki, Japan
David Holec, Austria
Satoshi Horikoshi, Japan
David Houivet, France
Rui Huang, USA
Michele Iafisco, Italy
Ilia Ivanov, USA
Katsuyuki Kida, Japan
Akihiko Kimura, Japan
Soshu Kirihara, Japan
Hongchao Kou, China
Luciano Lamberti, Italy
Marino Lavorgna, Italy
Pavel Lejcek, Czech Republic
Cristina Leonelli, Italy
Ying Li, USA
Jun Liu, China
Meilin Liu, Georgia
Yunqi Liu, China
Manuel Lopez-Amo, Spain
Fernando Lusquiños, Spain
Eric Maire, France
Peter Majewski, Australia
Bobby Kannan Mathan, Australia
Philippe Miele, France
A. E. Miroshnichenko, Australia
Hossein Moayed, Iran
Jose M. Monzo, Spain
Alfonso Muñoz, Spain
Rufino M. Navarro, Spain
Miguel Navarro-Cia, UK
Luigi Nicolais, Italy
Hiroshi Noguchi, Japan
Chérif Nouar, France
Tutomu Ohzuku, Japan
Olanrewaju Ojo, Canada
Gianfranco Palumbo, Italy
Anna Maria Paradowska, Australia
Matthew Peel, UK
Gianluca Percoco, Italy
Claudio Pettinari, Italy
Giorgio Pia, Italy
- Candido Fabrizio Pirri, Italy
Simon C. Potter, Canada
Francisca Puertas, Spain
Manijeh Razeghi, USA
Yuri Ribakov, Israel
Anna Richelli, Italy
Antonio Riveiro, Spain
Marco Rossi, Italy
Pascal Roussel, France
Francesco Ruffino, Italy
Antti Salminen, Finland
Paolo Samorì, France
Hélder A. Santos, Finland
Carlo Santulli, Italy
Fabrizio Sarasini, Italy
Fridon Shubitidze, USA
Donato Sorgente, Italy
C. C. Sorrell, Australia
Andres Sotelo, Spain
Costas M. Soukoulis, USA
Damien Soulat, France
Antonino Squillace, Italy
Manfred Stamm, Germany
Sam-Shajing Sun, USA
Kohji Tashiro, Japan
Miguel Angel Torres, Spain
Laszlo Toth, France
Achim Trampert, Germany
Luca Valentini, Italy
Hanoch Daniel Wagner, Israel
Rui Wang, China
Lu Wei, China
Jörg M. K. Wiezorek, USA
Wei Wu, USA
Hemmige S. Yathirajan, India
Wenbin Yi, China
Belal F. Yousif, Australia
Michele Zappalorto, Italy
Li Zhang, China
Ming-Xing Zhang, Australia
Wei Zhou, China

Contents

Advanced Building Materials for Passive House and Energy Storage

Sumin Kim, Jae D. Chang, and Jae-Han Lim
Volume 2017, Article ID 5792427, 1 page

Evaluation of Materials in a Biomechanical System for Uses in Industrial Lifting Activities

Roberto L. Avitia, Gustavo L. Badilla, Rubén C. Martínez, Jose A. Cárdenas-Haro,
Marco A. Reyna, and Miguel E. Bravo-Zanoguera
Volume 2017, Article ID 3658161, 9 pages

Experimental and Stress-Strain Equation Investigation on Compressive Strength of Raw and Modified Soil in Loess Plateau

Youchao Zhang, Yihong Wang, Nana Zhao, and Tianya Wang
Volume 2016, Article ID 2681038, 10 pages

Development of an Efficient Steel Beam Section for Modular Construction Based on Six-Sigma

Tae-Hyu Ha, Bong-Ho Cho, Hongjin Kim, and Dae-Jin Kim
Volume 2016, Article ID 9687078, 13 pages

Structural Behavior of Reinforced Self-Compacted Engineered Cementitious Composite Beams

Bashar S. Mohammed, M. F. Nuruddin, Muhammad Aswin, Nursyuhada Mahamood, and Hashem Al-Mattarneh
Volume 2016, Article ID 5615124, 12 pages

Effect of Water-Cement Ratio on Pore Structure and Strength of Foam Concrete

Zhongwei Liu, Kang Zhao, Chi Hu, and Yufei Tang
Volume 2016, Article ID 9520294, 9 pages

Editorial

Advanced Building Materials for Passive House and Energy Storage

Sumin Kim,¹ Jae D. Chang,² and Jae-Han Lim³

¹*Soongsil University, Seoul, Republic of Korea*

²*The University of Kansas, Lawrence, KS, USA*

³*Ewha Womans University, Seoul, Republic of Korea*

Correspondence should be addressed to Sumin Kim; skim@ssu.ac.kr

Received 26 January 2017; Accepted 26 January 2017; Published 20 March 2017

Copyright © 2017 Sumin Kim et al. This is an open access article distributed under the Creative Commons Attribution License, which permits unrestricted use, distribution, and reproduction in any medium, provided the original work is properly cited.

Buildings are responsible for more than 40 percent of global energy use and one-third of global greenhouse gas emissions, both in developed and developing countries (UNEP, 2009). Therefore building sector has the largest potential to reduce the significant greenhouse gas emissions. Nowadays passive house and nearly zero-energy building have been a hot issue for the sustainable building design and construction (Jurgen Schnieders, 2006). To do this, it is necessary to reduce the energy requirement during construction and operation periods. To reduce the energy consumption in buildings without discomfort, advanced building materials, including high-performance concrete, insulation materials, wood-based materials, thermal energy storage, high-insulated windows, and air-tight wall constructions, should be developed and applied to the building components (Feist, 2005). And thermal energy storage systems (i.e., phase change materials (PCM)) can be used to reduce energy consumption of buildings. It means that the application of PCM in buildings not only saves energy but also decreases the temperature fluctuation. By utilizing these technologies, it is also much easier to achieve that the architect and engineers can reduce energy demand in buildings. By stimulating energy efficiency in existing and new buildings, significant reductions in energy demand can be achieved in passive house and zero-energy buildings. During the wide propagation of the advanced building technologies, governmental subsidies can be more attractive to individual construction projects and the effective way to promote at a large scale (Audenaert, 2008).

This special issue aims to publish high quality research articles and review articles addressing recent advances on advanced building materials for saving energy. During the

past few months, we reviewed 14 research papers submitted by international distinguished scholars. During the intensive blind-peer-review process and in-depth discussions, 5 articles were accepted for the publication, even if the other papers were rejected mainly due to the discrepancy in scope of this special issue. Accepted papers were ended up with a useful review and edit process to improve the quality of paper. The related topics of accepted papers include the soil in the Loess Plateau region as one of traditional building materials, an efficient steel beam structure for modular construction, foam concrete materials with good thermal insulation performance, the biomechanical system in an industrial manufacturing process, and the reinforced self-compacted engineered cementitious composite beams. Some article analyzed the compressive behavior of raw soil and modified soil specimens through experiments and proposed the generalized stress-strain equations for the widespread application. Some article investigated the structural behavior of large-scale reinforced self-compacted engineered cementitious composite beams via theoretical models. Some article dealt with a systematic design approach for the development of an efficient steel beam section for modular construction based on Six-Sigma. And some article proposed a biomechanical system for the emulation of the movement of human arm, leg, and spine movements, as an industry alternative to manage heavy operations in a manufacturing process.

*Sumin Kim
Jae D. Chang
Jae-Han Lim*

Research Article

Evaluation of Materials in a Biomechanical System for Uses in Industrial Lifting Activities

Roberto L. Avitia,¹ Gustavo L. Badilla,² Rubén C. Martínez,³ Jose A. Cárdenas-Haro,⁴ Marco A. Reyna,¹ and Miguel E. Bravo-Zanoguera¹

¹*Bioengineering and Environmental Health Department, Universidad Autónoma de Baja California, Mexicali, BC, Mexico*

²*Tecnologico Nacional de Mexico, Mexicali, BC, Mexico*

³*Instituto Tecnológico de Rehabilitación, Mexicali, BC, Mexico*

⁴*Computer Science Department, California State University, Bakersfield, CA, USA*

Correspondence should be addressed to Roberto L. Avitia; ravitia@uabc.edu.mx

Received 23 September 2016; Revised 12 December 2016; Accepted 5 January 2017; Published 19 February 2017

Academic Editor: Sumin Kim

Copyright © 2017 Roberto L. Avitia et al. This is an open access article distributed under the Creative Commons Attribution License, which permits unrestricted use, distribution, and reproduction in any medium, provided the original work is properly cited.

A biomechanical system is proposed for the emulation of the movement of human arm, leg, and spine movements, as an industry alternative to manage heavy operations in a manufacturing process. The Matlab® programming environment is used as a simulation tool for the analysis and validation of this proposed biomechanism. This machine would reduce the accidents due to human exposure to risky industry environments like the particular one at the host company that we are using as a model for our research. They claim that the accidents in this area alone arise to around thirty percent of the total, causing a decrease in the productivity of the company and other economic losses derived from the worker injuries and insurances.

1. Introduction

The materials science is an area of high interest in bioengineering and in the subfield of biomechanics. Any material required in the operations of a biomechanical system has to be evaluated carefully. There is a technological revolution in the medical sciences triggered by the biomechanics and bioengineering in general, used mainly in the design and manufacturing of systems that can replace the functions of human organs and muscles. The main motivation has been supplying the high demand generated by the people with disabilities around the world that depend on this kind of technological developments to live a better quality of life. The use of this kind of biomechanical systems is very uncommon in industry where the use of robots and automated equipment is the norm. The aim of this research is the design of a biomechanical system for its use in an industrial manufacturing process. The host company for this research and analysis is the “Industrial Metal, SA De CV” located in Mexicali, BC, Mexico. In this industry, the operation of interest for our

study consists of an activity that require the lifting of heavy objects (over one hundred kilograms in weight) to a height up to two meters. This operation has been performed so far only by humans.

The most important factors in the fabrication of a biomechanical system are the design requirements and the materials that will be used for that. Some analysis is required prior to the selection of the materials to determine the mechanical resistance, stress, and strain levels as well as the presence of any possible corrosion phenomena. This system could improve the lives of people with some specific needs or at least give some comfort to many others. For example, when a limb is lost completely or partially by either birth defect, illness, or accident, this system could bring some relief for these people. Biomechanical engineering has been used largely to develop systems to support people with disabilities. This branch of bioengineering rarely has sparked interest in developing systems that could prevent injuries in the industrial plant areas where heavy duties and human endurance are demanded, lowering at the same

time the consumption levels of energy. In order to fulfill the standards Newtonian mechanics is applied to materials science to obtain the adequate biomechanical systems that can be used in some specific industrial processes. The human-body systems are too complex; thus numerical and graphical simulation methods are applied in all the biomechanical studies performed. In the design of the biomechanical systems the materials to be used can be evaluated according to the specific needs and applications of the work environment. In some ways, these systems are similar to the equipment and machinery used for lifting heavy objects. This work and research were carried out using an iterative approach of hypothesis and verification including multistage modeling, computer simulations, and experimental measurements. A model of the simulated biomechanical systems was previously developed based on the human kinetics to determine the mechanical, electrical, and electromechanical characteristics required for the controlling of the movements in the systems. The industrial kinesiology is of great importance in the design and development of biomechanical systems for heavy duty activities, including the lifting of heavy objects. The industry is eager in the adoption of this kind of systems since these decrease energy costs and avoid any type of air pollutant and heat that contribute to the global warming. The relationship between the biomechanics and material science is of great interest to determine the types of materials that can be used in the biomechanical systems fulfilling the standards required in the manufacturing processes of the industrial plants. The most used materials on these cases are chromium, nickel, niobium, titanium, tungsten, vanadium, and derivatives of iron (as alloy of steel with copper). The characteristics of mechanical strength, strain, stress, and corrosion effects of these materials are analyzed to determine if at some point they could cause a decrease in the functionality of the biomechanical system in the proposed working conditions. This is also a way to set the lifespan. These systems are more often used in the electronic and metalworking industry. There are several specialized computer programs for evaluation of biomechanical systems and devices functionality. The most commonly used programs are the Matlab, SolidWorks®, and Catia®. They are supported by functions to develop simulations with block diagrams and graphs. In these computer programs the biomechanical systems operation stages and its operability predictions are evaluated in real time. The evaluation of the corrosion effect on the biomechanical systems is very important because it can cause material fatigue that originates fractures or fissures that could generate mechanical and electrical failures that lead to potential accidents. There are various types of process control simulations appearing in computer programs to evaluate the functionality of a biomechanical system, as it is in the case of Matlab. One of these control processes is the *PID* controller, which consists of a proportional section (*P*) without modification and two more sections defined as the integrative (*I*) and the derivative (*D*), which change according to the operation under analysis, in periods of time. Together the three sections generate similar required functions based on mathematical algorithms, represented in a block diagram with input and output simulations.

The steels are a large family of metals, with iron alloys in mixtures of carbon and other elements, being softened with different percentages of carbon at high levels (from 0.45% to 1.5% at most), medium levels (from 0.25% to 0.45%), and low levels (under 0.25%). The carbon steel is the most widely used, being an important alloy of iron and carbon that is commonly used in building constructions and other industrial applications due to their mechanical resistance and hardness. The typical carbon steel alloys may contribute up to 2.1% of its atomic weight. By varying the number of alloying elements or other process factors we get the consistency of the steel. Either varying the elements of the solute and the precipitation phase or by slowing the dislocation movements we can control the hardness and ductility of the produced metal (Tunil H. et al., 2002). In order to avoid the corrosion phenomena, protection films are used developed with the metals mentioned above. All these factors are considered in the design of the biomechanical systems, especially for those to be performing in the harsh environments of industrial activities. The properties of a steel are closely related to the percentages of the metals that compose it. For example, there is a large difference in the hardness between the carbon steel used in structures of buildings and the carbon steel utilized in an ornamental structure [1]. The rapid cooling of carbon steel with cold water when it is in red state generates more fragility, so it must be cooled slowly. Carbon steel heat treatment is another method that determines the physicochemical properties, which must match the standards required in industries [2]. Metallic materials are the most used for industrial plants, house structures, buildings, bridges, cars, and appliances. Artifacts exposed to aggressive environments in arid areas such as the city of Mexicali [3] suffer a high deterioration generated by the effect of corrosion mainly in carbon steel components. Another big factor in Mexicali is due to the presence of sulfurs emitted in the city mainly by the geothermal energy plant which supplies electricity to Mexicali, its valley, and some cities of Sonora and southwestern United States. It is located 20 km from the Mexicali city, emitting high levels of hydrogen sulfide (H_2S); this air pollutant reacts with the atmosphere and generates sulfur dioxide (SO_2). Other sulfurs emission sources are from the vehicular traffic and the oxidation ponds in this city of Mexicali. To ensure the quality and protection of the products made of carbon steel, this metallurgy plant "Industrial Metal, SA De CV" located in Mexicali city is using different types of metallic coatings [4]. Two different metal coatings are applied: one is a protection against corrosion and the other is the appropriate decorative polished layer [5].

2. Methodology

Currently, there are several models of biomechanical systems, they were developed using mathematical algorithms, and the functionality is evaluated by steps. In this case the first stage of this work is the design of the system and the second and final stage corresponds to the fabrication of the biomechanical system. Subsequently, an evaluation of materials for use in devices and biomechanical systems is

performed, and parameters of hardness, mechanical strength, mechanical elasticity, and the effect of corrosion phenomena are analyzed. Furthermore, as a part of the evaluation we include the manufacturing costs of each metallic component, materials alloyed with steel. This research was suggested by the “Industrial Metal, SA De CV” as part of their industrial needs and requirements to increment the security standards. The analysis of the biomechanical system and the corresponding mathematical model and simulation was developed from 2014 to 2015. The next stage will be the manufacturing of this biomechanical system.

In this study the descriptive statistical technique called ANOVA is applied, with assessments and simulations in Matlab; also a statistical computer program is applied. Moreover, this same process is used to evaluate the materials and corrosions according to the ASTM standards as ASTM G1 (ASTM G1-03), G4 (ASTM G4-01), and G31 (ASTM G31-72). And for the analysis of indoor corrosivity levels in this metallurgy company evaluation, we use the ISO standards as ISO 11844 (ISO11844, 2005), ISO 11844 (ISO11844, 2006), and the method AHRAE (AHRAE, 1999). The study is conducted in two stages as mentioned below.

(1) *Evaluation of Biomechanical Models.* Analyzing mathematical algorithms to obtain the most suitable ones for the fabrication of the biomechanical system, in accordance with the operations and standards required for heavy lifting in this “Industrial Metal, SA De CV” metallurgy company, located in Mexicali. This model could be also used in other companies or industries with similar needs.

(2) *Analysis of Materials.* Evaluation of some types of alloys with different metals to obtain the material required for the fabrication of the biomechanical system, for the particular operations required in this industry evaluated.

The analyses and assessments of the biomechanical systems operation help in the predictions related to their functionality. These analyses assist in the evaluation of the types of materials to be used in the biomechanical systems as well as in the mechanical, electrical, and electromechanical parameters required, along with the pollution and the climate variables that may affect its operation [6, 7]. The steels are a large family of metals, with iron alloys in which it is mixed with carbon and other elements, being soft with different percentages of carbon at high level (0.45% to 1.5%), medium (0.25% to 0.45%), and low (0.35%), but are never greater than 1.5%. The carbon steel is the most widely used, being an important alloy of iron and carbon that is widely used in construction and other applications due to their mechanical resistance and hardness. The most common metal coatings are as follows.

(a) *Copper Plating.* The copper coating is the process in which a copper film is deposited on the metal material to be protected by using an electric current.

(b) *Chrome Plating.* This process is used with the technique of electroplating, where the thin protective film is deposited on the metal to be protected. The chrome film can be decorative

and to increase the corrosion resistance, facilitate cleaning procedures, or increase the hardness of the surface.

(c) *Nickel Plating.* In this process the electroplating is used to deposit very thin films to have metallic surface protected. The nickel film may be for decorative aspects, corrosion resistance, or wear resistance, mainly [2].

3. Results and Discussion

The required models were developed and tested in a simulated environment as a way to evaluate its operation. This biomechanical model means to be part in a manufacturing process in the “Industrial Metal, SA De CV” company in an area requiring the lifting of heavy objects. The information obtained indicates that the carbon steel alloyed with chromium is the material that fits best in costs and functionality the requirements for the fabrication of this biomechanical system. Furthermore, the mathematical algorithms and graphs show the relation of the physical properties of the materials, which are correlated with climatic and air pollution parameters in the first graph and the bidirectional motor speed control used to lift the heavy objects. In addition, some analyses are conducted with the Matlab software, using mathematical algorithms to verify the optimal operation of the biomechanical system before the fabrication of it, saving this way time and money.

3.1. *Design of the Biomechanical System.* The design of the biomechanical system was carried out based on the requirements of the manufacturing processes area in the “Industrial Metal, SA De CV” company, where our study was developed for that purpose. Figure 1 shows a schematic diagram of the system used for the evaluations and simulations in the design of the final model fulfilling all the characteristics and standards demanded in the work environment of this metals industry.

3.2. *Mathematical Modeling of Biomechanical Systems.* We used the load supporting modeling process of Matlab software for the tensile stress analysis in our system. This is the force applied to the load to be lifted and the deformation occurs simultaneously at different points on the measured system. As shown in Figure 2, this modeling includes gain (P), voltage (I), and deformation (D) as a part of the PID (Proportional-Integrative and Derivative) system.

Figure 2 shows a diagram of the PID controller; there we can observe the control processes of the main parameters involved, in the analysis of the functionality of the biomechanical system for industrial activities. These parameters are autoregulated by the feedback stage, and the system behavior is according to the mathematical algorithms it depends on, which is displayed in the graphs. This contributed in obtaining information on how the devices and the control mechanisms are activated by the movements of the biomechanical system. The signals representing these operations are shown in Figure 3.

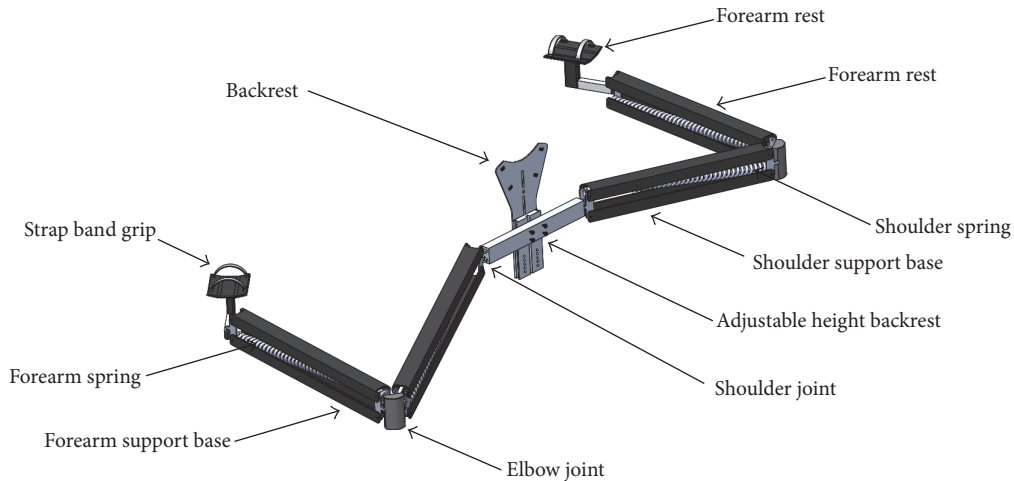


FIGURE 1: Schematic diagram of the system used in the evaluation and design of the final biomechanical model for the industrial activities.

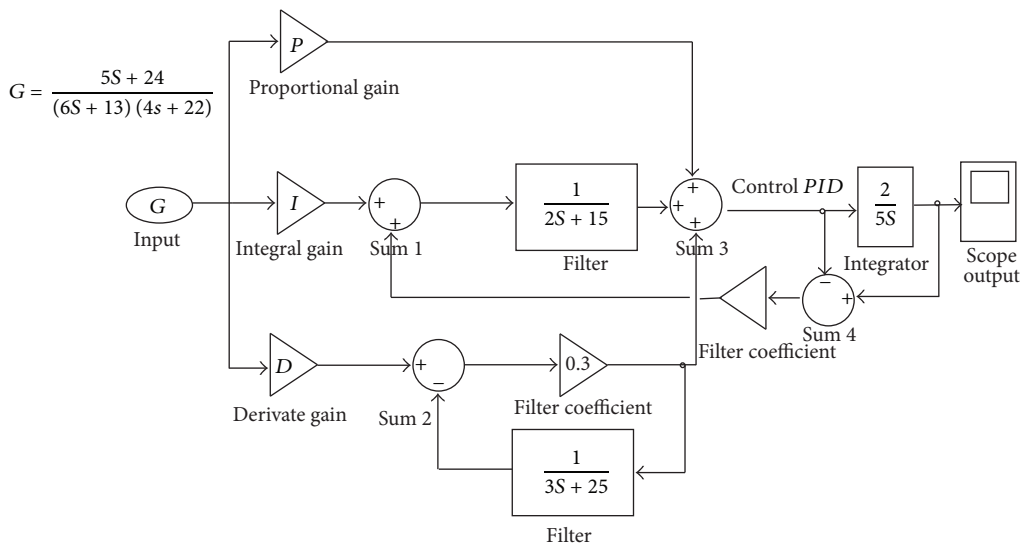


FIGURE 2: Diagram of the functionality of the proposed material for the manufacturing of the biomechanical system.

The *P* stage, which represents the frequency of the input signal that is related to cycle time of the operation of the biomechanical system, is evaluated manually without the mathematical algorithms. The stage of integrative and derivative activity indicates how the actions can be autoregulated; the block of actions is controlled by an electromechanical device coupled to an electronic device, which are part of the mechanisms of the proposed biomechanical system. These mechanisms as a part of the simulation analysis are activated at the same frequency of the input signal. This generates an operation to determine the mechanical stress and deformation properties which are the most important ones based on the movements produced by the electromechanical and electronic devices. The results from the process described above can be seen in Figure 3, where the four essential activities of the *PID* controller are shown. The sinusoidal input signal is represented in Figure 3(a), which is the most commonly used in electromechanical and electronic systems

that require high power levels for the operation, as it is the case of this heavy duty biomechanical system. These high power levels of energy are applied in industrial activities such as in the lifting of heavy objects, which is the case in the industrial plant evaluated, where we carried out this research analyzing the work cycles under different conditions.

Figure 3(b) illustrates the signal in a time period of 10 cycles; this input signal is required for the biomechanical system bidirectional motor to carry out the heavy lifting. This is done at minimum speed in a continuous movement to avoid any risk of injury for the workers performing these activities. Figure 3(c) is the result of the stress analysis in the same period of time. It represents the integrative section that indicates the voltage levels correlation from the proposed material (carbon steel with an alloy of chromium). The functionality of the mechanisms mentioned above for the heavy lifting operation is evaluated based on these results. The feed for the analysis of the initial operation of this

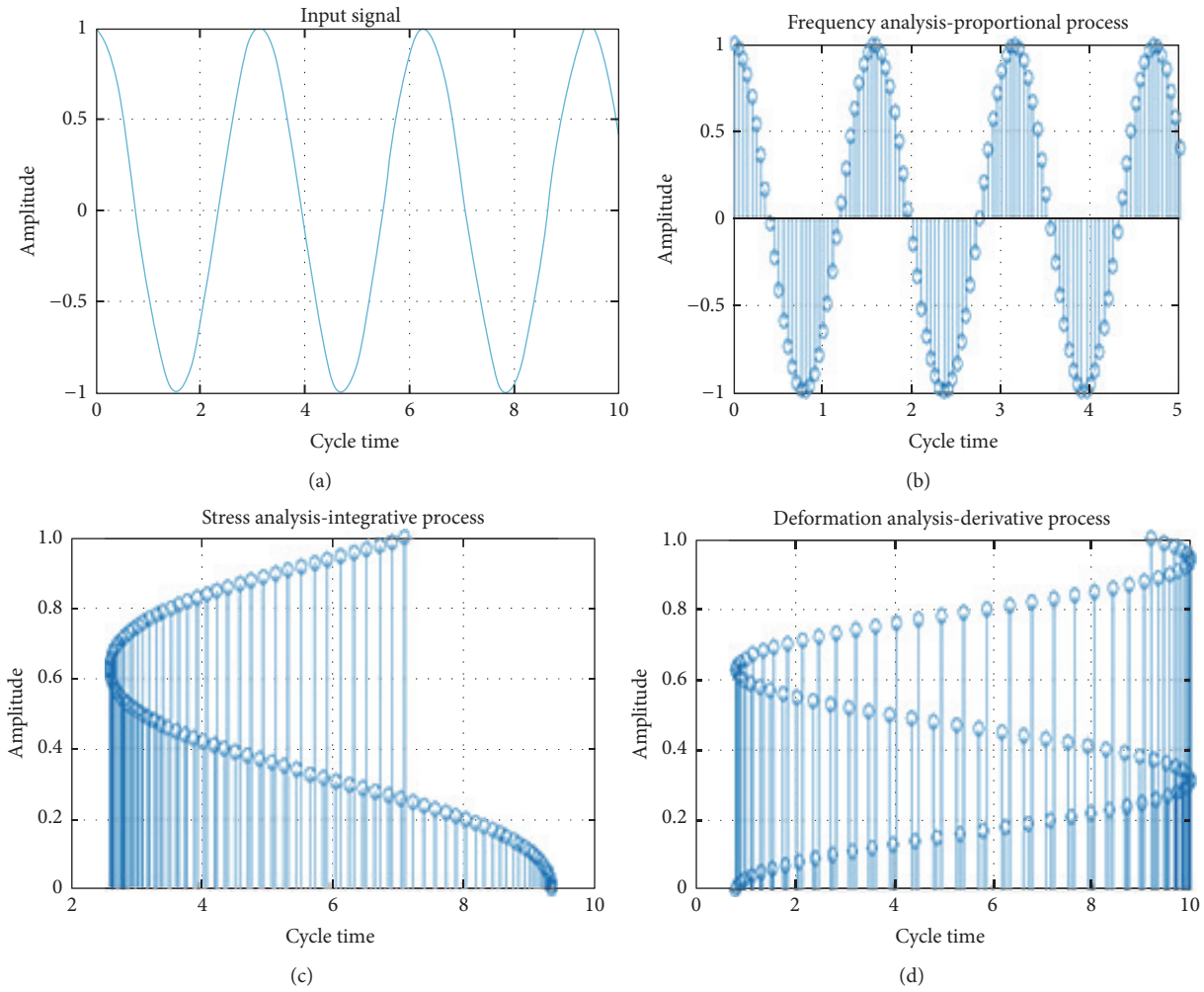


FIGURE 3: Simulation of operation of the SS 304 material for the biomechanical system.

function starts with a delay of two seconds from the process activity in the *PID* controller. Figure 3(c) illustrates the stress analysis in the proposed material. The evaluation process starts at the end of the tenth cycle, and the obtained values are returned after about two seconds of operation of the biomechanical system. That is, after almost ten seconds in total of operation of the biomechanical system, it begins to exert the first tension force; the appropriate levels of tension for the optimal functionality of this system are determined through the feedback of the mechanisms involved.

As the feedback function is processed, it is observed that the cycle restarts about every two seconds. This is because the coupling of the electrical signals in the *PID* feeds the electromechanical and electronic devices, and a time delay is required to begin the operations. The simulation analysis shows that the process under evaluation is optimal and that this design can be implemented in the manufacturing of the biomechanical system.

The material stress is evaluated every two seconds looking for the possibility of a fracture and a consequent failure in the mechanisms constructed with this metal. The increased tension in each analysis period in the integrative process was

exactly after 9.5 seconds from the beginning of each stage in the controlled evaluation environment.

Figure 3(d) indicates a similar evaluation at the same cycles of time compared to that in the other figures, which shows that from one second exactly the evaluation starts and finishes in the tenth cycle. After that the process starts all over again, providing again the feedback after one second and finishing after another ten cycles, completing another full period for the biomechanical system. Figure 3(d) represents the deformation of the material under evaluation; the outcome means that this material fulfills perfectly the requirements of the biomechanical system. Another mechanical property of serious importance is the corrosion resistance, since it causes material deterioration and damage by fatigue. This can lead to a faster breakage than expected with even chances of a fatal accident. The mechanical property is assessed in Table 1. The importance of this kind of analysis is clear, to avoid any event that would put at risk the life or health of any of the workers in the company. As is indicated in Figure 3, the material chosen for this is the Stainless Steel 304 (or SS 304).

Table 1 shows the values of the evaluated parameters, which indicate the greater number of cycles per unit of

TABLE 1: Mechanical properties and function analysis of the electromechanical and electronic mechanisms.

Time, cycles by minute	Correlation rate mg·m ² /year	Stress KPa	Deformation %	Observations
2	12	10	0.3	Materials do not present negative effect
4	23	15	0.5	Materials do not present negative effect
6	38	20	0.8	Materials present small stains and can be a negative effect
8	45	25	1.0	Materials present small stains and can be a negative effect
10	62	30	1.4	Materials present big stains and can be a negative effect as fracture

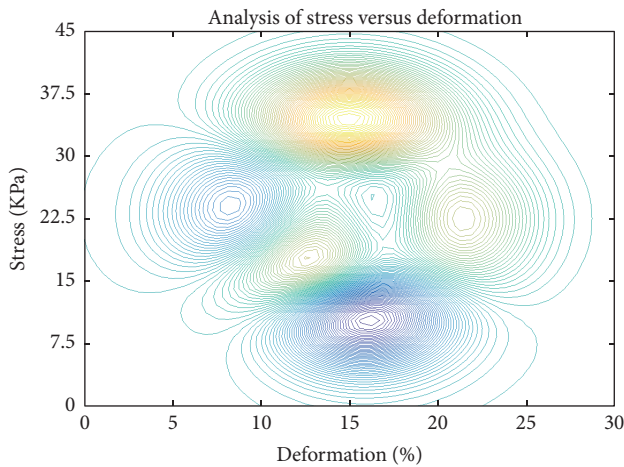


FIGURE 4: SS 304 stress and deformation correlation analysis in the ten cycles per minute period.

time and the presence of corrosion, together with high strain indices, can degenerate the properties of the carbon steel without the alloy, causing a fast deformation and the possibility of a fracture. Figure 4 shows a correlation at different levels of stress and strain processes of the simulation performed with the mathematical algorithms. As expected, the mechanical properties have influence in the operation of the entire biomechanical system. As shown in Figure 4, the deformation process starts at about 10 KPa and the different levels of stress are represented with different indices of colors, where the blue and green together show the first point of deformation, and stress levels near 35 KPa are in yellow tone. This is a big negative impact on the functionality of the proposed material, where deformation can be up to 10% or even slightly higher. This could generate a lack of confidence in the use of the biomechanical system when performing the activities of heavy lifting in the company evaluated. As a solution, we recommend the use of carbon steel with alloy of chrome to avoid the presence of the corrosion phenomena.

Furthermore, an analysis of the speed control for the bidirectional motor was carried out to avoid quick and drastic movements that can cause a damage in the arms, spine, or legs of the workers in charge of the operation of this biomechanical system. This is represented in Figure 5 as a block diagram with two input signals (square and

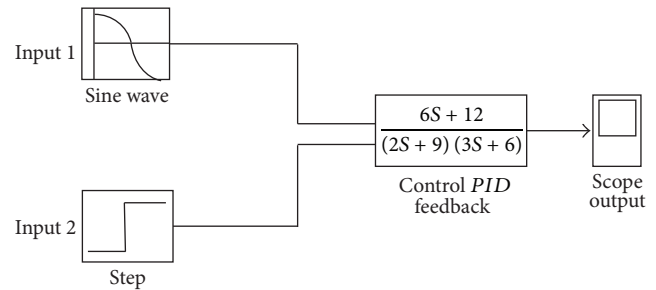


FIGURE 5: Diagram of the speed control for the motor in the biomechanical system.

sinusoidal waves) and the feedback for the speed control of the bidirectional motor. The coupling of the two signals is necessary to have a constant and immediate acceleration through the electronic control devices that can maintain a fixed speed as required. The input and output signals are shown in Figure 6.

In Figure 6 the two waves (square and sinusoidal) are shown used as input signals and the resulting output signal for the controlled speed. This is based on the mathematical algorithm that supports the optimal performance of the full biomechanical system.

The two input signals are represented in Figures 6(a) and 6(b), with 100 cycles per time unit; these signals are fed to the mathematical algorithm giving a single output signal illustrated in Figure 6(c), where control is 80 cycles per time unit, showing a slight delay in response due to the operations of the electronic devices (transistors and relays, coupled to integrated circuits). The control signal is represented in Figure 6(c), where the start of the operation of the motor is observed, with the negative cycle indicating the movement in one direction, reaching the level of 0 and is increased to the positive level that represents the movement in the other direction.

3.3. The Use of Carbon Steel Coating. The materials evaluated to be applied as coatings on the carbon steels metal were analyzed according to the costs and functionality, at a theoretical level by the Density Functional Theory (DFT) program used for molecular modeling, obtaining the results through the processes analysis, as shown in Table 2. The testing of different

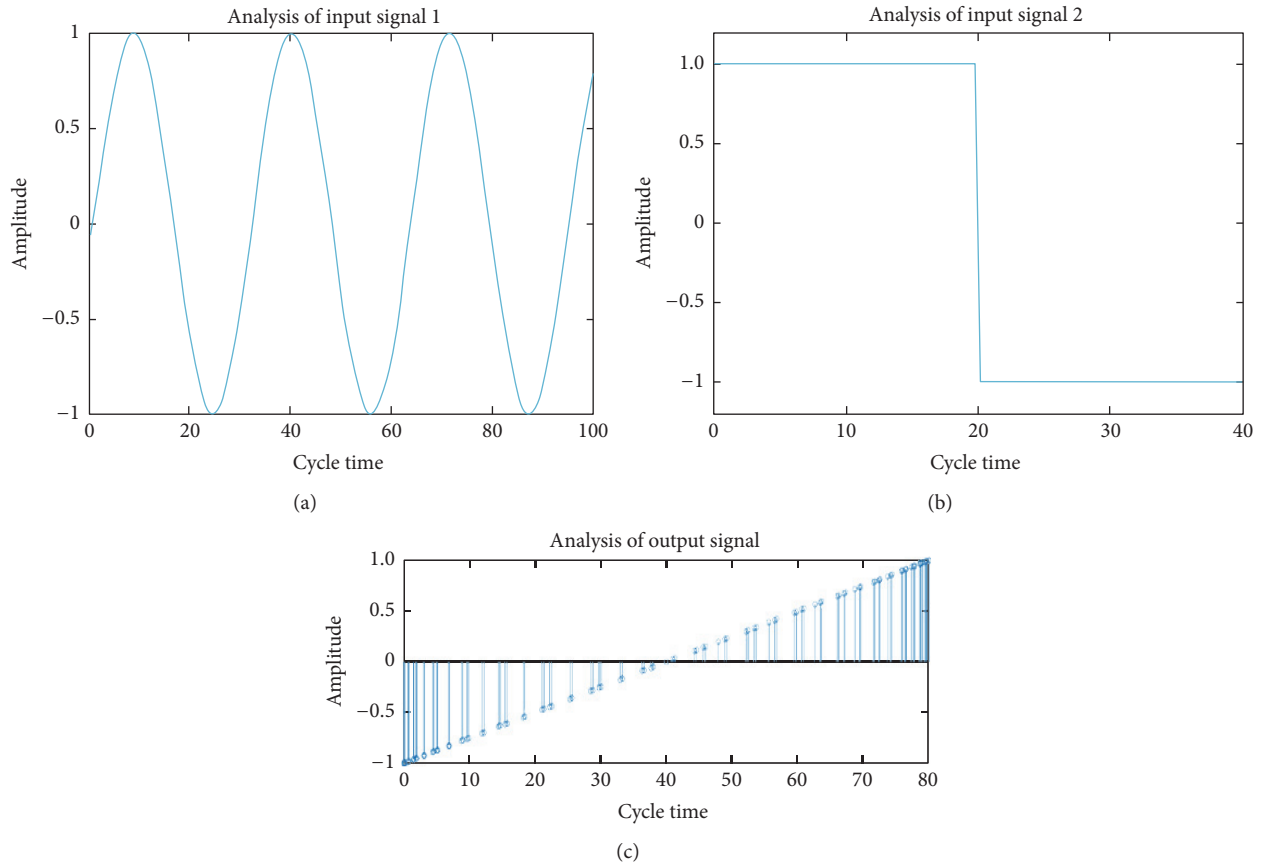


FIGURE 6: Simulation of the motor speed control for the biomechanical system made of SS 304.

TABLE 2: Characterization of phases of alloys for coatings in carbon steels.

Alloy	Percentage of affinity (%)	Change of phase	Crystal parameters
Fe-C-Cu-Cr	80%	FT	$a = 5.455, c = 5.145$
Fe-C-Cu-Ni	75%	FT	$a = 5.615, c = 5.325$
Fe-C-Cr	80%	FM	$a = 5.785, b = 5.150, c = 5.360$
Fe-C-Cu-Cr-Ni	85%	FM	$a = 5.660, b = 5.235, c = 5.345$

Monoclinic phase change (FM) to tetragonal (FT) = FMFT; tetragonal phase change (FT) to monoclinic (FM) = FTFM.

alloys of metals is with the goal of obtaining the required functionality within the standards and at the lower cost.

Table 3 shows the configuration of the observed phases in the process of forming the alloys; the three with the higher affinity are the ones that we propose for the coatings, since those have more binding or adherence properties. The monoclinic and tetragonal phases are the most common in the manufacturing processes of carbon steels with body centered crystalline structures. The best material out of this study is the alloy of carbon steel with chrome.

3.4. Costs of Coatings. The costs of the metals (copper, chromium, and nickel) used in the coating processes of the steel manufactured by the company evaluated fluctuated in the period of one year (2014), as indicated in Table 3 based on public international data from a global metal analysis company.

TABLE 3: Analysis of copper, chromium, and nickel prices in US dollars (2014).

Months	Cost of metals, dollars/pounds		
	Copper	Chrome	Nickel
January	3.12	1.02	7.84
February	3.15	1.04	8.12
March	3.18	1.05	8.25
April	3.23	1.08	8.36
May	3.26	1.06	8.30
June	3.32	1.03	8.35
July	3.36	1.07	8.87
August	3.26	0.98	6.67
September	3.22	1.03	6.89
October	3.17	1.05	7.43
November	3.25	1.06	7.65
December	3.36	1.08	7.79

Source: Kitco Gold index, <http://www.kitco.com>.

TABLE 4: Correlation of costs, manufacturing process, and time of deposition (coating).

Specifications of coatings		Copper			Metals Chrome			Nickel		
		M.gr.	<i>t</i>	C	M.gr.	<i>t</i>	C	M.gr.	<i>t</i>	C
<i>D</i> , cm	<i>e</i> , mm									
2.00	0.0025	0.14	1426	0.95	0.11	4191	1.17	0.14	1532	1.43
2.50	0.0030	0.21	2139	1.22	0.17	6288	1.30	0.21	2298	1.67
3.00	0.0035	0.30	2994	1.45	0.24	8803	1.44	0.29	3218	1.88
3.50	0.0040	0.39	3993	1.63	0.32	11737	1.59	0.39	4290	2.11
4.00	0.0045	0.50	5133	1.79	0.41	15091	1.72	0.50	5515	2.34
4.50	0.0050	0.63	6417	1.88	0.51	18863	1.88	0.63	6895	2.78
5.00	0.0055	0.77	7843	2.07	0.62	23055	1.99	0.77	8427	3.13
5.50	0.0060	0.93	9411	2.13	0.75	27666	2.23	0.92	10112	3.67
6.00	0.0065	1.10	11122	2.22	0.88	32696	2.85	1.09	11951	4.23
6.50	0.0070	1.30	12976	2.33	1.03	38146	3.67	1.27	13943	4.89

[*D*, cm] diameter in centimeters of the steel to be covered; [*e*, mm] coating thickness in millimeters; [M.gr.] grams of metal used for the coating; [*t*] time in seconds for the deposition; [C] cost in pesos for coating process per meter.

As we can see the costs of the metals did not change much. In Table 3 the costs of obtaining the raw material for the manufacturing stages of the coatings are added, plus the costs of the manufacturing processes with the steel protection methods. Moreover, in this evaluation the amounts of each metal are considered in grams for the coating of the steel, in addition to the process cycles required in applying each material deposition.

Table 4 shows the effect of the coating process after each round, obtaining the respective geometric figure, according to their physical and chemical characteristics correlated with the costs of the deposition process. As the diameter of the area to be covered and the coating thickness increase, the amount in grams of the metal to be used for the covering, the deposition time, and the costs of the coating process for each metal increase as well.

4. Conclusions

The aim of this research is to solve the problem of human injuries mainly in the spine caused by the lifting of heavy objects as a part of the operations required in one particular station at the host industry supporting this study. Our analysis concluded that by its cost and mechanical properties the carbon steel alloyed with chrome is the adequate material to use in this particular case. Other results worth pointing out are the motor function regulation for its use in the biomechanical system and the development of the mathematical functions for the analysis of the stress and deformation correlation.

Furthermore, a corrosion resistance evaluation is performed according to the input signals from the mechanical, electromechanical, and electronic devices required in the operations; this is to assure for a long time the quality of the functionality of all the biomechanical system proposed to the company for the lifting of objects up to one hundred kilograms.

The support from the company is mainly to replace some obsolete machinery and equipment and reduce the power consumption and the use of fuels that generate high levels of pollution and heat, which is a big problem in the city of Mexicali in particular and in the world in general due to the climate change and greenhouse effect. The relevance of this research is the design and analysis of biomechanical systems that can be used directly in the industry production lines to make all the process more efficient and less prone to accidents which in both ways save a lot of money by increasing also the productivity and performance of the workers. Analyzing the Matlab simulation tool and its mathematical functions, we found that there is a high level of confidence and acceptance in that software that has been used in similar researches as a validation tool. In the information provided as a part of this document the coupling of the mechanical, electromechanical, and electronic systems to integrate the biomechanical system is observed.

Competing Interests

The authors declare that there is no conflict of interests regarding the publication of this paper.

Acknowledgments

The authors thank the “Industrial Metal, SA De CV” that opened its doors to all the participating institutions as well as the full support provided that made this research possible.

References

- [1] M. Fernández, *Preparación Mecánica y Química de Minerales*, Editorial Dossat SA, 2006.
- [2] A. Reardon, “Metallurgy for the non-metallurgist,” in *ASTM Standards Book*, ASM International, 2nd edition, 2011.

- [3] L.-B. Gustavo, V.-S. Benjamín, and S.-W. Michael, "Atmospheric corrosion in the sea food industry in the Northwest of México," *Revista Científica Instituto Politécnico*, vol. 16, no. 2, pp. 67–73, 2012.
- [4] G. L. Badilla, B. V. Salas, and M. S. Wiener, "Micro and nano corrosion in steel cans used in the seafood industry," in *Scientific, Health and Social Aspects of the Food Industry*, InTech, 2012.
- [5] M. Anthony, D. Jones, and H. Rayner, "An introduction to microstructures, processing and design of steels," *Materials, Methods and Treatments Journal*, vol. 3, no. 2, pp. 56–63, 2002.
- [6] A. Tsouknidas, S. Savvakis, Y. Asaniotis, K. Anagnostidis, A. Lontos, and N. Michailidis, "The effect of kyphoplasty parameters on the dynamic load transfer within the lumbar spine considering the response of a bio-realistic spine segment," *Clinical Biomechanics*, vol. 28, no. 9-10, pp. 949–955, 2013.
- [7] J. S. Temenoff and A. G. Mikos, *Biomaterials: The Intersection of Biology and Materials Science*, Pearson/Prentice Hall, Upper Saddle River, NJ, USA, 2008.
- [8] ASTM Standards, *Standards to Technical Experiments*, ASTM, 2000.

Research Article

Experimental and Stress-Strain Equation Investigation on Compressive Strength of Raw and Modified Soil in Loess Plateau

Youchao Zhang, Yihong Wang, Nana Zhao, and Tianya Wang

School of Civil Engineering, Chang'an University, Xi'an 710061, China

Correspondence should be addressed to Yihong Wang; zycgodgod@163.com

Received 1 September 2016; Revised 22 November 2016; Accepted 7 December 2016

Academic Editor: Sumin Kim

Copyright © 2016 Youchao Zhang et al. This is an open access article distributed under the Creative Commons Attribution License, which permits unrestricted use, distribution, and reproduction in any medium, provided the original work is properly cited.

As a special kind of soil is widely distributed in Loess Plateau of northwest China, it is difficult to use for growing crops and has poor structural property. According to local arid climate, the best utilization of the soil is as earthen construction material and it has been used for thousands of years. To research and improve the mechanical properties, the study investigates the response of soil with cement, lime, sand, and straw as admixtures to compressive loading. The influence on compressive strength and ductility of additives in different proportions is compared and analysed. The experimental data is also used for the formulation of dimensionless and generalized models describing the raw soil and modified soil's full stress-strain response. The models can be applied to soil and modified soil in Loess Plateau with variable strength and deformation characteristics and therefore may be exploited for earthen construction design and nonlinear structural analyses.

1. Introduction

It is estimated that 30 percent of the world's population currently live or work in earthen structures [1, 2] and the proportion rises to 36 percent in China. As an environmental friendly material, with superior thermal performance, lower cost, and abundant availability, earthen materials have been used in construction of shelters for thousands of years [3]. Earthen construction is also a part of the world's cultural heritage. The world-famous cave-houses and Hakka residential architecture are typical examples in China, and the unique building culture also influences folk art. Nowadays, the promotion of sustainable development has put pressure on all industries, including the construction industry to use suitable methods to protect the environment. Due to current global concerns for sustainable development that have arisen from extensive environmental problems such as climate change and the impoverishment of resources coupled with the rapid pace of technological advancement within the building sector, interest in alternative building materials such as earth has developed [4–6]. Researches on earthen construction and local soil as building material have received growing attention from the scientific community in the past 20 years.

As one of traditional building materials, the soil in the Loess Plateau region which is widely distributed in the northwest of China, different from soil in other regions of China (northeastern black soil, northern rocky mountain soil, southeastern red soil, etc.), is difficult to be used for growing crops. This kind of soil is highly collapsible, which will lead to serious distortion and asymmetrical settlement, so that the Loess Plateau became one of the most serious soil erosion regions all over the world. And this is another reason why this kind of soil has been used as building material for thousands of years. However, the characteristics of soil in Loess Plateau also lead to poor structural properties and adversely affect the seismic performance of local earthen constructions. For seeking sustainable development, one of the key issues is how to make use of the loess resource in northwest China and improve the mechanical property as building material.

A reliable assessment of the material's compressive strength, as well as of its stress-strain response, is required in efficient design and appraisal of earthen structures. For many centuries, construction based on unbaked earth had developed to take advantage of the material's relatively high compressive strength. Though other parameters, such as density, frost resistance, and water absorption, may be

TABLE 1: Mass ratio of additives in specimens.

Admixture	Cement	Sand	Lime	Straw
	4%	5%	5%	0.5%
Mass ratio	8%	15%	10%	1%
	12%	25%	15%	

specified in design, compressive strength has become a basic and generally accepted unit of measurement to specify the quality of materials [7]. Minke suggested that, for dry building elements made of earth, a compressive strength of 2–5 MPa should be required [8]. Significant researches have been conducted to examine the possibility of improving the mechanical properties of soil modified by adding varying percentages of admixtures [3, 9, 10]. However, different from other building materials, there is a distinct lack of formal technical guidance concerning the laboratory testing of compression test procedures for soil material [11, 12]. The mechanical properties of materials are affected by the method of specimen fabrication, dimensional effects, the chosen loading system, and whether specimens are tested wet or dry.

According to the dry climate of northwest China, to obtain the best performance of soil materials, the soil in Loess Plateau was traditionally compacted into walls at optimum moisture content (OMC) nearby. In the past, the soil material might be mixed with a little additive in some cases that maybe wheat straw, lime, or even sand which depend on local conditions. This paper investigates experimentally compressive behaviour of raw soil and modified soil specimens produced at OMC. The modified soil specimens include soil with cement, lime, sand, and straw in different proportion independently. The results are used to formulate nondimensionalized models which are capable of describing the full stress-strain response. Based on that, the generalized stress-strain equations are proposed for design purpose and widespread application. The outcomes of this work are deemed particularly useful to researchers and practitioners working in the field of earthen construction and soil material.

2. Materials and Methods

2.1. Materials. For the specimens' production, the soil materials are obtained from the suburb of Yan'an city located in Loess Plateau which is the typical sample of Chinese northwest loess and often used locally as construction material. Besides the traditional additives (lime, sand, and straw), Ordinary Portland Cement was also adopted for this study. The mass ratio of every additive is under three different proportions and determined by related researches or traditional ways (shown in Table 1). Among them, the specimens of soil with 1.5% straw cannot be fabricated due to unconsolidated materials. Thus, there are 12 groups of raw soil and modified soil specimens and each group consisted of 10 specimens. Cement was grade OPC 32.5 (Yaoxian Cement Plant) and other materials were sourced locally. The straw was dried wheat straw and chopped into lengths of 20 mm to 30 mm before mixed.

2.2. Preparation of Test Specimens. Before mixed, the natural soil constituents were prepared by initially being air-dried and then the lumps of dried soil were broken down manually and then sieved to remove particles exceeding 4.75 mm in laboratory. To obtain a stabilised soil, a homogeneous mixture was made by blending the required amount of additive with sifted soil in a tray before adding water. The required amount of water was obtained based on the OMC of raw soil and modified soil which was evaluated by test (Table 2).

Based on the current geotechnical engineering test method and criteria (GB/T 50123-1999) [13], the well-blended mixture was poured into three layers to be compacted in a mould of internal diameter 102 mm and height 116 mm with a collar of 70 mm attached thereto (Figure 1). The compaction energy was $604 \text{ kJ}\cdot\text{m}^{-3}$, which was consistent with Chinese and other international standards. After that, the collar was removed and the extra soil was trimmed to make it level with the top of the mould. Then the specimens were demoulded and air-dried under the laboratory conditions at 20–25°C for 60 days before testing the compressive strength (Figure 2). The size of the cylindrical specimens was 102 mm in diameter and 116 mm in height.

2.3. Testing of Compressive Strength. The compressive tests were undertaken in the Building Material Laboratory at Chang'an University. A universal compression testing machine (YA-300) with a maximum load of 300 kN was used in the testing procedure to apply stress at a rate of $0.1 \text{ kN}\cdot\text{s}^{-1}$. The load-displacement curves were output by the electrohydraulic servocontrol system (GTC350).

3. Experimental Results and Discussion

3.1. Modes of Failure in Compression. Compressive failure of cylinders was characterized by bulging and formation of near-vertical surface cracks [11]. Accordingly, the failure modes can be divided into three categories: raw soil, sand soil, and straw soil. Those of cement soil and lime soil are basically similar with raw soil (Figure 3). In this category, cracks occurred at the top of the specimens and then extended to the middle. At maximum compressive stress, several vertical cracks ran through the whole specimen and the blocks between vertical cracks spalled off (Figure 3(a)). The remains of the specimen were similar and in the shape of an hourglass (Figure 3(b)). Besides, cement soil specimens were of better quality and the cracks therein appeared later than those in specimens of raw soil and lime soil.

For sand soil, after cracks appeared, there were more vertical cracks which were distributed evenly over the sample surface. While at maximum compressive stress, there were obviously more vertical cracks than raw soil at the sample surface (Figure 4(a)). But the exfoliation of specimens was less than raw soil specimens during failure process, and the diameter of failure specimens is larger (Figure 4(b)).

Differing from other groups, straw specimens had a larger deformation at maximum compressive stress. And the specimens did not instantly fail after that, and they were subjected to significant additional deformation before structural collapse (Figure 5(a)). The wheat straw in specimens snapped

TABLE 2: OMC of raw soil and modified soil.

Modified soil	Raw soil	Cement			Lime			Sand		Straw		
		4%	8%	12%	5%	10%	15%	5%	15%	25%	0.5%	1%
Optimum moisture content/%	18.2	19.8	20.4	21.4	22.0	22.1	22.2	17.4	17.4	17.2	18.3	18.4
Maximum dry density/g cm ⁻³	1.72	1.69	1.67	1.67	1.58	1.57	1.56	1.75	1.78	1.79	1.68	1.65

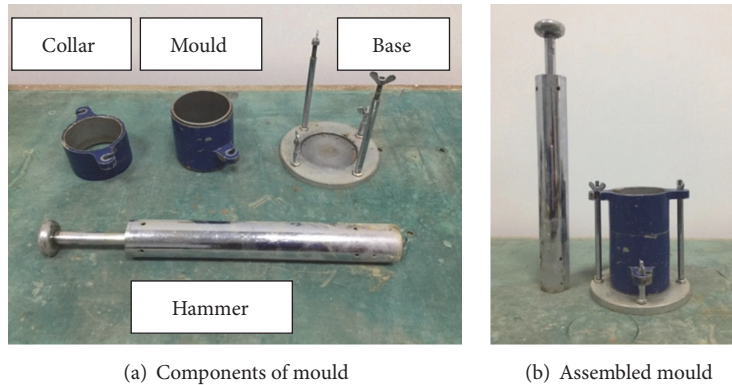


FIGURE 1: Mould of specimens.



FIGURE 2: Air-cured specimens.

and could be heard in all loading process. Following the completion of the compression tests, the specimens had not fully disintegrated (Figure 5(b)). This can be justified, to some extent: straw fibres held together some significant parts of the soil matrix, delaying failure.

3.2. Stress-Strain Behaviour and Ultimate Compressive Strength. Test results are summarized in Table 3. Compression stress-strain curves were plotted and one typical curve for raw soil and each kind of additive are picked up and shown in Figure 6, to contrast the effects of different additive.

The compressive strength of raw soil reached 3.10 MPa and the peak strain was 0.00202. Actually, the strength is generally acceptable but of high discreteness with the variation coefficient 0.1947. It means, as building material, raw soil has an unstable mechanical property, while the variation coefficient of other modified soil groups all decreased significantly that is around 0.1 basically.

There is obvious effect of cement to improve the compressive strength and specimens of soil with 12% cement had the best compressive strength in the test (6.55 MPa, an increase of up to 111.3% compared with raw soil). Data produced by various researchers show linear correlation between compressive strength and cement content [7] which also exists in this test. The peak strain was unaffected by cement content and kept 0.020 around same as raw soil (not exceed 5%). As a typical inorganic cementitious mineral, the cement reacts with active silica and alumina in loess microspheres and then converted them into calcium silicate hydrate (CSH) gel and calcium aluminate hydrate (CAH) gel [14]. These water-stable compounds can improve the compressive strength of earthen materials by increasing the bond strength between internal structures.

Sand added to the loess can improve the gradation and the quality of the earthen construction material and then improved its compressive strength. The effect, in magnitude, ranked second to that of cement, and the strain increased by sand content. Similar to coarse aggregate in concrete, there is an optimal proportion for improving the degree of density. Therefore, in the test, the compressive strength first increases and then decreases with the increase of sand content and soil with 15% sand got the highest strength.

The straw added to the soil cannot increase the compressive strength but, as a reinforcing agent, the deformability of specimens was better than any other groups. As the cracks are growing, straw hindered relative slippage of damaged sections and prevented soil block deformation, thus restraining crack development and improving the ultimate strain. The peak strain of soil with 1.0% straw was 0.0423 which has an increase of 109.4% compared with raw soil.

The lime reacts with the moisture in the soil and the compounds created in hydration reaction can improve the



FIGURE 3: Raw soil, cement soil, and lime soil specimens.



FIGURE 4: Sand soil specimens.

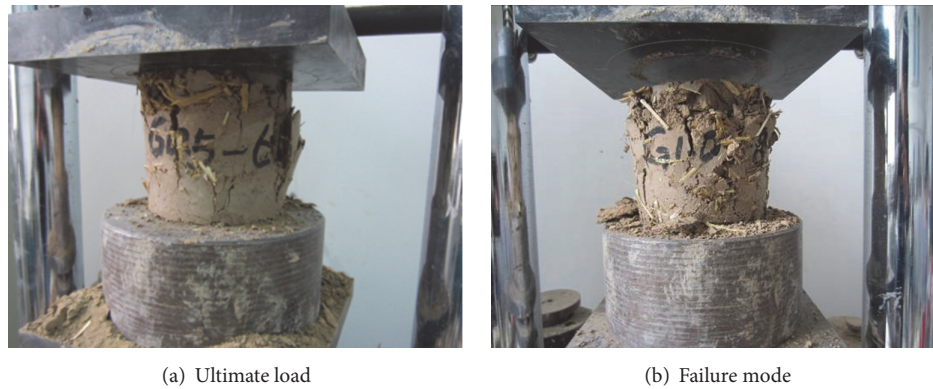


FIGURE 5: Straw soil specimens.

TABLE 3: Mean compressive strength and peak strain.

Modified soil	Raw soil	Cement			Lime			Sand			Straw	
		4%	8%	12%	5%	10%	15%	5%	15%	25%	0.5%	1.0%
Cracking load/kN	13.82	18.13	32.54	33.29	12.95	12.67	11.98	15.47	16.26	15.33	10.89	10.24
Ultimate load/kN	25.32	34.88	43.86	53.49	25.32	25.24	25.40	37.00	37.65	36.91	25.56	24.99
Ultimate compressive strength/MPa	3.10	4.27	5.37	6.55	3.10	3.09	3.11	4.53	4.61	4.52	3.13	3.06
Variation coefficient/%	19.47	9.94	12.89	8.11	11.43	9.07	6.15	10.85	7.39	3.77	7.45	8.04
Peak strain/%	2.02	2.04	2.08	1.90	1.67	2.08	2.63	2.12	2.33	2.69	2.97	4.23

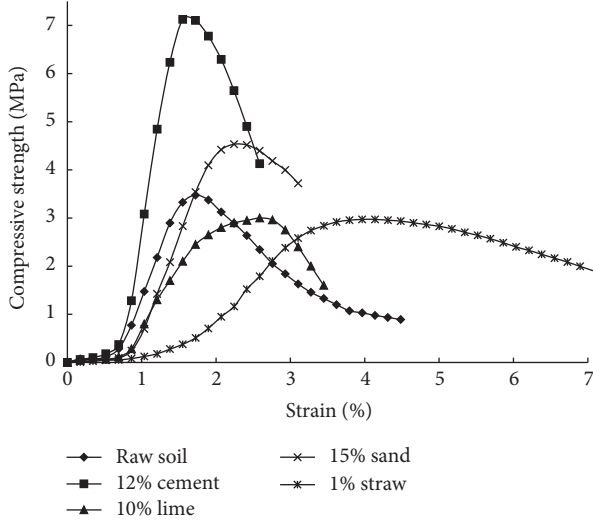


FIGURE 6: Stress-strain curves: specimens with different admixtures.

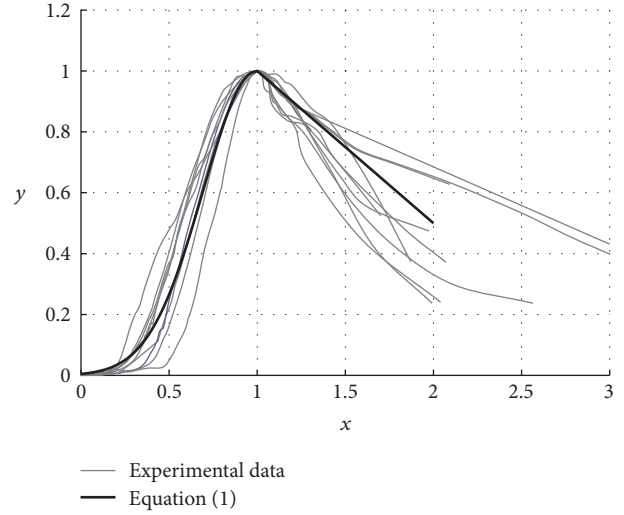


FIGURE 7: Dimensionless stress-strain curves: raw soil.

bonding with soil particles [15]. But, in this test, no matter specimens with 5%, 10%, and 15% lime, the mean compressive strength shows no increasing and the peak stain has no obvious regularity, either. It might be related to low levels of moisture content in soil sample. It is shown that the lime is not suitable for being added in soil in Loess Plateau as building materials, at least, as additive alone.

4. Stress-Strain Relationship under Uniaxial Compression

4.1. Nondimensionalized Stress-Strain Equation. Using results obtained from tests, stress-strain relations describing raw soil and soil with cement, sand, and straw responses to compressive loading were developed. To propose equations applicable to soil of Chinese northwest loess with varying load-bearing and deformation capacities, stress and strain values were normalised. Hence, the stress and strain of each specimen were dealt with by a dimensionless method: the normal stress σ_c was divided by the peak stress σ_0 ($y = \sigma_c/\sigma_0$) and the axial strain ϵ_c was divided by the peak strain ϵ_0 ($x = \epsilon_c/\epsilon_0$).

In previous researches on soil material or adobe, third-order polynomials were often adopted to capture the non-linear behaviour in the rising step [11, 16]. But, in this test, polynomial function was found not to accurately describe the concave down at the beginning of loading. Therefore, in this paper, a quadratic exponential function was used to fit the rising step of soil and modified soil curves. To ensure the validity of the equations, the following constraints were imposed: (a) the curves passed through the origin ($x = y = 0$), (b) the curves passed the point at which $\sigma_c = \sigma_0$ and $\epsilon_c = \epsilon_0$ ($x = y = 1$), and (c) the ascending branch and descending branch were considered as two separate strain intervals and the continuity of the curve is enforced at their common point ($x = y = 1$). The optimization problem was solved using standard MATLAB optimization routines, which yield the following fitted curves.

(1) Raw Soil and Cement Soil

$$y = \begin{cases} e^{-5.3(x-1)^2} & (x \leq 1) \\ 1.5 - 0.5x & (x \geq 1). \end{cases} \quad (1)$$

By comparing (1) with experimental data from raw soil, a satisfactory R^2 of 0.90 was achieved, which indicated that stresses are well predicted by (1), as is graphically verified in Figure 7.

With the different percentage of cement, the cement soil specimens were showed to be similar to the raw soil during the load process (Section 3.1). By the calculation, (1) was also applied to cement soil and, compared with experimental data, R^2 of 4%, 8%, and 12% cement soil was 0.96, 0.88, and 0.92, respectively. It indicated that the stress-strain relationship of cement soil was matched well with (1), especially for the rising step. An excellent correspondence similar to Figure 8 was obtained.

(2) Sand Soil. The dimensionless stress-strain curves of sand soil and straw soil were inapplicable with (1). Parameter m_s of the rising part is brought into the model and (2) derived as follows:

$$y = \begin{cases} e^{(-5.3+0.02m_s) \times (x-1)^2} & (x \leq 1) \\ 1.5 - 0.5x & (x \geq 1). \end{cases} \quad (2)$$

m_s is the mass percentage of sand in the specimen. Here, m_s in 5%, 15%, and 25% sand soil specimens was 5, 15, and 25, respectively. For $m_s = 0$, (2) is transformed into (1). The graphical representation of (2) and normalised stress-strain experimental data are shown in Figure 9. The determination coefficient R^2 reached 0.96, 0.88, and 0.91 for 5%, 15%, and 25% sand soil, respectively.

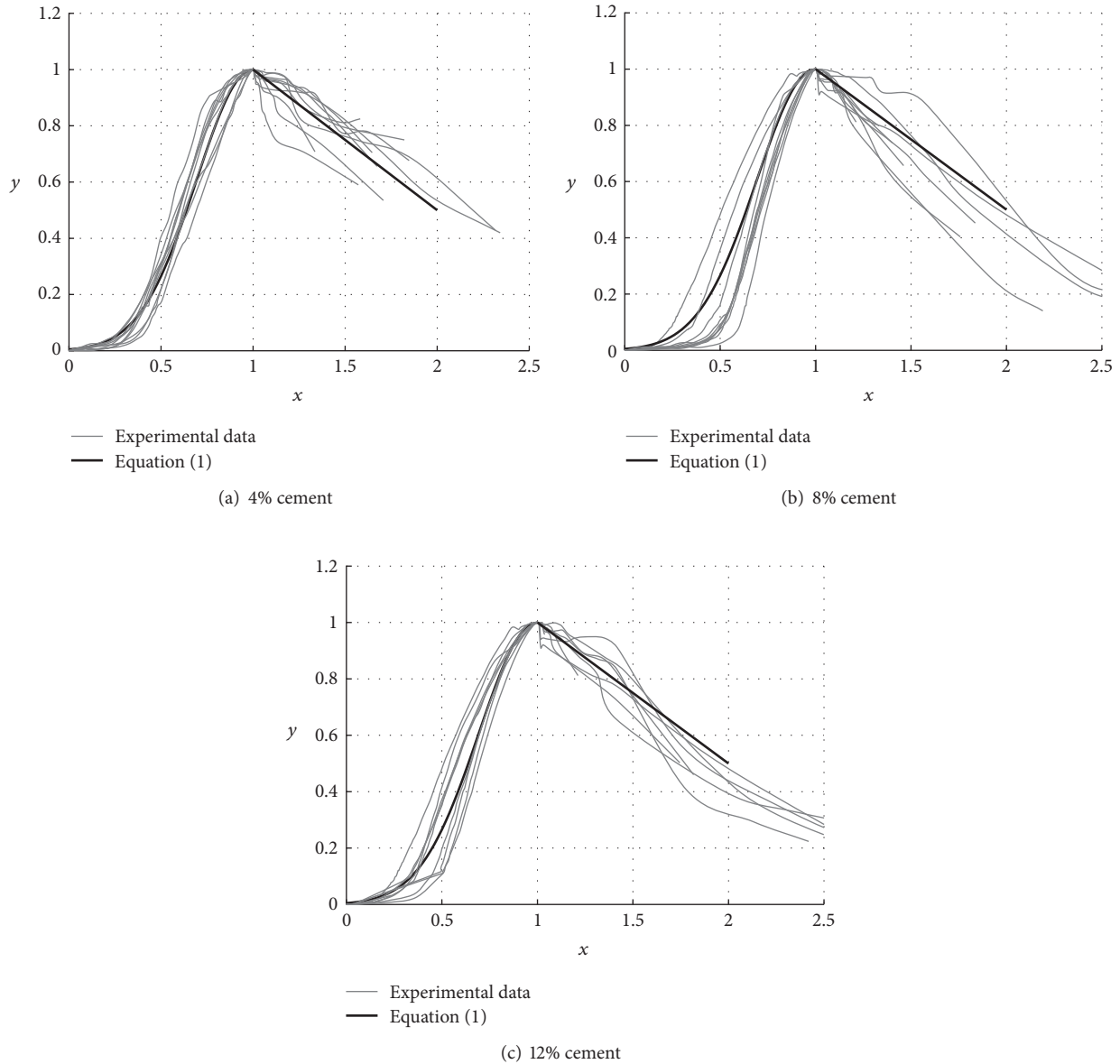


FIGURE 8: Dimensionless stress-strain curves of cement soil.

(3) *Straw Soil*. For straw soil specimens, besides that parameter m_{st} is brought into the rising part, the descending branch also needed to be adjusted. Equation (3) is as follows:

$$y = \begin{cases} e^{(-5.3+m_{st}) \times (x-1)^2} & (x \leq 1) \\ 1.4 - 0.4x & (x \geq 1), \end{cases} \quad (3)$$

where m_{st} is the mass percentage of straw in a specimen. In this test, m_{st} of 0.5% and 1.0% straw soil specimens was 0.5 and 1.0. Equation (3) matched the experimental data (Figure 10) and a satisfactory R^2 which reached 0.90 and 0.85 was achieved.

It can be inferred that the rising step of stress-strain curves of soil and modified soil in the test had an increasing tendency which slowed down first and then became faster under compression. The proposed equations can reflect the

mechanical properties of soil in Loess Plateau well and support references for other earthen construction materials.

4.2. Generalized Stress-Strain Equations. For design purposes and widespread application, it is necessary to predict the peak compressive strength and strain for raw soil and various modified soil cases. The generalized stress-strain equations for raw soil in Loess Plateau and feasible modified soil are proposed based on the general regularity analysed in Section 3.2 and nondimensionalized equation in Section 4.1.

As mentioned, the peak strain ε_0 of raw soil and cement soil with different proportions remains stable and around 0.020. And according to the linear correlation between compressive strength and cement content in the test and other researches, the parameters of cement soil equation were determined (Figure 11). The generalized stress-strain

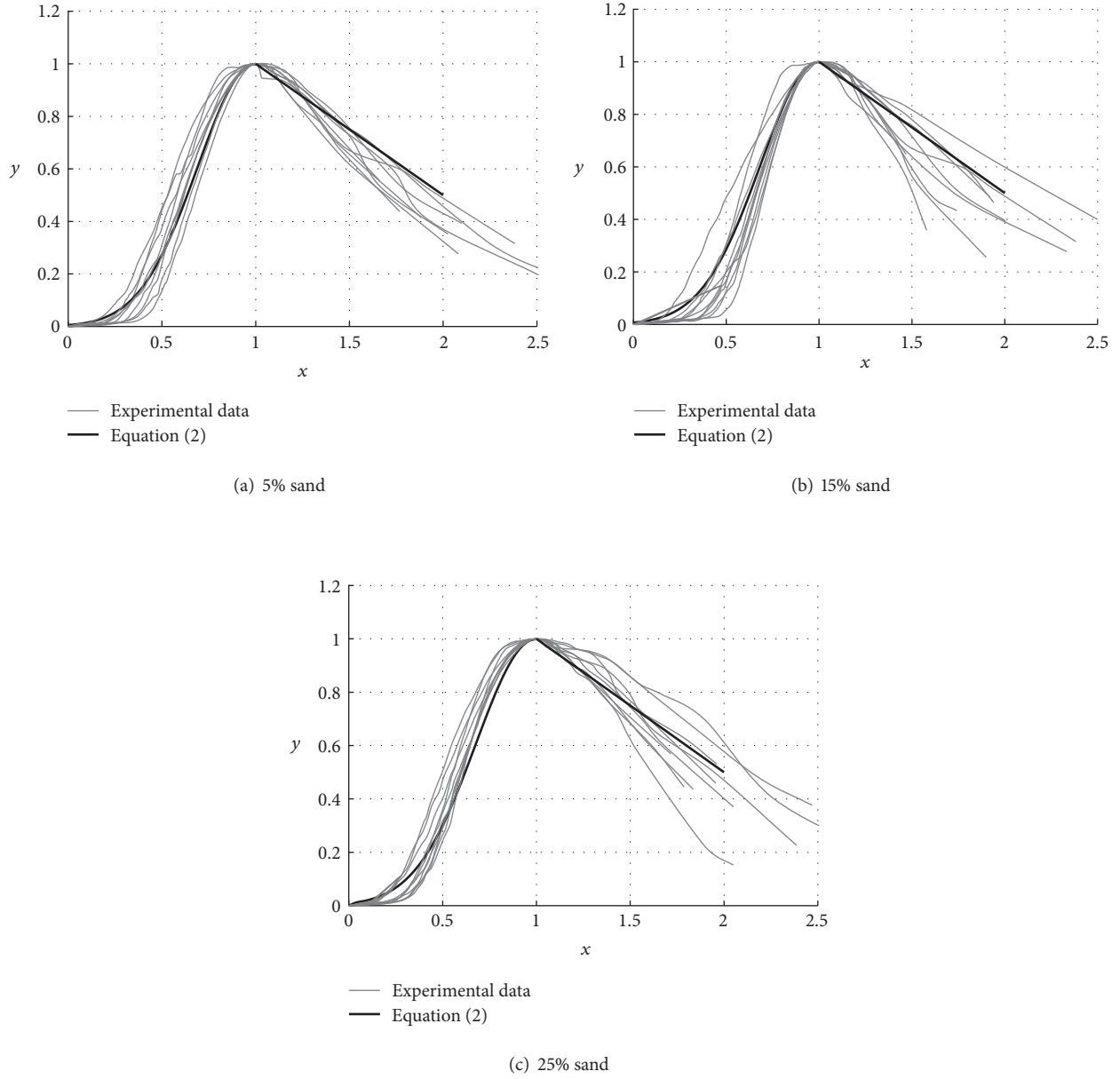


FIGURE 9: Dimensionless stress-strain curves of sand soil.

equations for raw soil and cement soil are shown in (4)–(6). As m_s and m_{st} , m_c is the mass percentage of cement in specimens. m_c of the 4%, 8%, and 12% cement soil specimens is 4, 8, and 12. For $m_c = 0$ which means for soil without cement, (6) is turned into (4).

(1) Raw Soil

$$\sigma_r = \begin{cases} 3.1e^{-5.3(\epsilon/\epsilon_0-1)^2} & (\epsilon \leq \epsilon_0) \\ 4.65 - 1.55 \frac{\epsilon}{\epsilon_0} & (\epsilon \geq \epsilon_0), \end{cases} \quad (4)$$

$$\epsilon_{0,r} = 0.020. \quad (5)$$

(2) Cement Soil

$$\sigma_c = \begin{cases} (3.1 + 0.29m_c) e^{-5.3(\epsilon/\epsilon_0-1)^2} & (\epsilon \leq \epsilon_0) \\ (3.1 + 0.29m_c) \left(1.5 - 0.5 \frac{\epsilon}{\epsilon_0}\right) & (\epsilon \geq \epsilon_0), \end{cases} \quad (6)$$

$$\epsilon_{0,c} = 0.020. \quad (7)$$

For sand and straw soil, at maximum compressive stress, the peak strain increased with additive content. According to the experimental data, the peak strain of sand soil ($\epsilon_{0,s}$) and straw soil ($\epsilon_{0,st}$) both have linear correlation with additive content (Figure 12). Therefore, the equation of $\epsilon_{0,s}$ and $\epsilon_{0,st}$

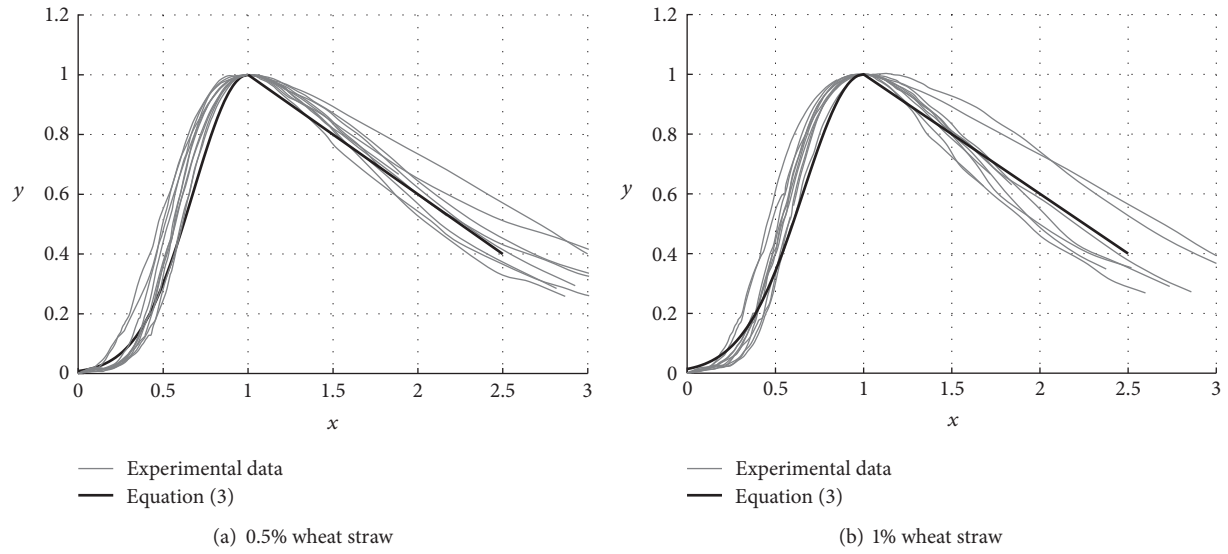


FIGURE 10: Dimensionless stress-strain curves of straw soil.

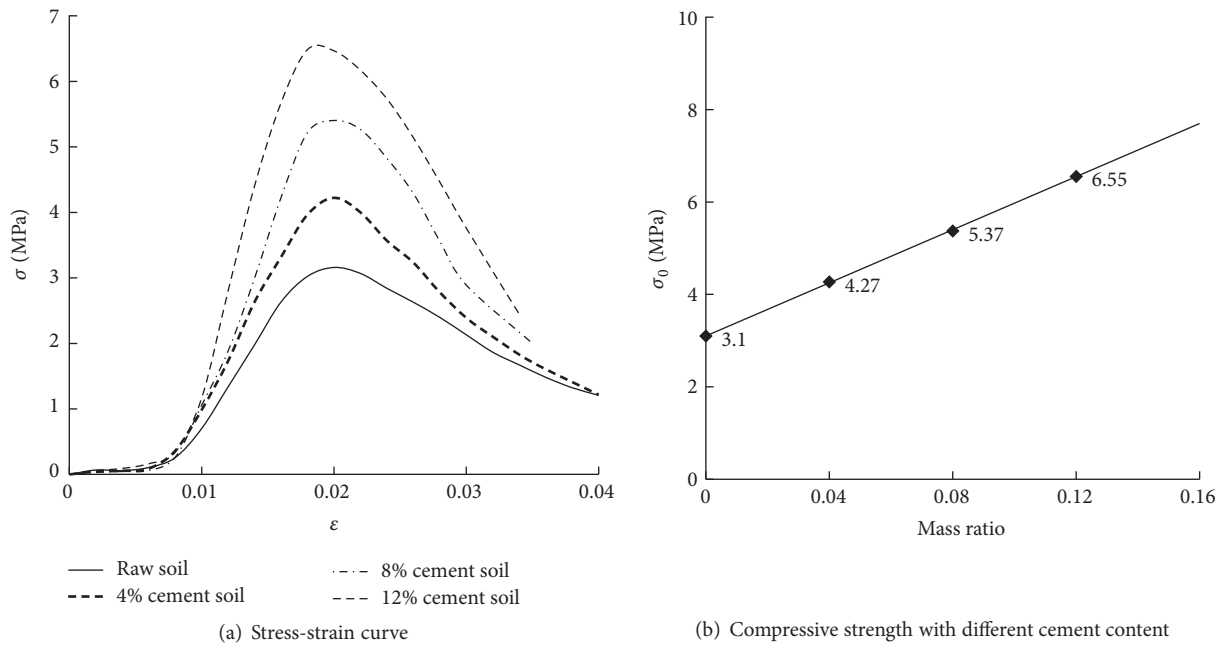


FIGURE 11: Relationships between stress-strain and cement content.

needs to be adjusted by bringing parameter m_s and m_{st} in (9) and (11). The ultimate compressive strength of straw soil remains unchanged by adding straw content and (10) was given based on (3). For stress-strain equation of soil with sand, as mentioned in Section 3.2, the relationship between stress and sand content does not match the linear trend and the changing laws cannot be convincible determined by three proportions of sand and soil; (8) is given useable only for soil with 15% sand as it is recommended.

(3) Sand Soil

$$\sigma_{s,15\%} = \begin{cases} 4.6e^{(-5.3+0.02m_s)(\epsilon/\epsilon_0-1)^2} & (\epsilon \leq \epsilon_0) \\ 6.9 - 2.3 \frac{\epsilon}{\epsilon_0} & (\epsilon \geq \epsilon_0), \end{cases} \quad (8)$$

$$\epsilon_{0,s} = (0.020 + 0.3 \times 10^{-3} m_s). \quad (9)$$

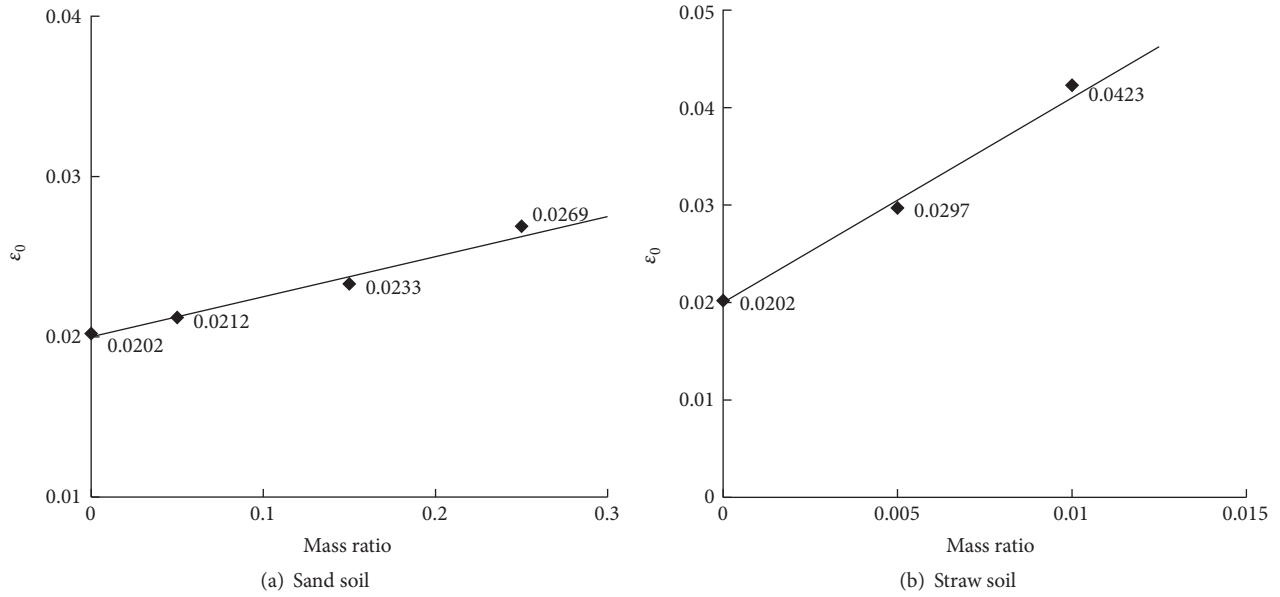


FIGURE 12: Relationships between stress and additive content of sand soil and straw soil.

(4) Straw Soil

$$\sigma_{st} = \begin{cases} 3.1e^{(-5.3+m_{st})(\varepsilon/\varepsilon_0-1)^2} & (\varepsilon \leq \varepsilon_0) \\ 4.34 - 1.24 \frac{\varepsilon}{\varepsilon_0} & (\varepsilon \geq \varepsilon_0), \end{cases} \quad (10)$$

$$\varepsilon_{0,st} = (0.020 + 0.021m_{st}). \quad (11)$$

5. Conclusions

To improve the mechanical property of soil in Loess Plateau as building material, the experimental research of 120 raw soil and modified soil specimens that were under compression test was carried out. Based on the characteristics of soil and local conditions, specimens were made at OMC and fully dried (8 to 10 weeks) in the laboratory. The method and results offer references for the modification of loess and soil in other regions considering the lack of internationally accepted standardised testing procedures specifically referring to unfired clay materials.

The mechanical properties under compression of soil in Loess Plateau and modified soil were obtained. It indicated that cement can significantly improve compressive strength, while the straw fibres were used to improve the ductility of soil material, but the mass ratio of straw should not exceed 1.0%. Sand was added to improve the particle distribution and soil with 15% sand achieved the best results in the test. Lime is not suitable for being added in this kind of soil as additive alone.

The constitutive model developed for describing the stress-strain behaviour under compression is well-fitted to the experimental data. The dimensionless and generalized model is based on a quadratic exponential function with parameters adjusted for additive content. It is anticipated that the proposed model can have applications in earthen

construction designs and analytical nonlinear engineering computations.

Disclosure

Any opinions, findings, and conclusions or recommendations expressed in this paper are those of the authors and do not necessarily reflect those of the funding agency.

Competing Interests

The authors declare that they have no competing interests.

Acknowledgments

The work presented herein was performed with a financial grant from the National Natural Science Foundation of China (51478043).

References

- [1] H. Nirroumand, M. F. M. Zain, and M. Jamil, "Various types of earth buildings," *Social and Behavioral Sciences*, vol. 89, pp. 226–230, 2013.
- [2] R. W. Salim, J. M. Ndambuki, and D. A. Adedokun, "Improving the bearing strength of sandy loam soil compressed earth block bricks using Sugercane Bagasse Ash," *Sustainability*, vol. 6, no. 6, pp. 3686–3696, 2014.
- [3] F. Pacheco-Torgal and S. Jalali, "Earth construction: lessons from the past for future eco-efficient construction," *Construction and Building Materials*, vol. 29, pp. 512–519, 2012.
- [4] I. Demir, "Effect of organic residues addition on the technological properties of clay bricks," *Waste Management*, vol. 28, no. 3, pp. 622–627, 2008.

- [5] X. Dong, V. Soebarto, and M. Griffith, "Strategies for reducing heating and cooling loads of uninsulated rammed earth wall houses," *Energy and Buildings*, vol. 77, pp. 323–331, 2014.
- [6] M. Bouasker, N. Belayachi, D. Hoxha, and M. Al-Mukhtar, "Physical characterization of natural straw fibers as aggregates for construction materials applications," *Materials*, vol. 7, no. 4, pp. 3034–3048, 2014.
- [7] J.-C. Morel, A. Pkla, and P. Walker, "Compressive strength testing of compressed earth blocks," *Construction and Building Materials*, vol. 21, no. 2, pp. 303–309, 2007.
- [8] G. Minke, *Building with Earth*, DE GRUYTER, Berlin, Germany, 2009.
- [9] P. Walker and T. Stace, "Properties of some cement stabilised compressed earth blocks and mortars," *Materials and Structures*, vol. 30, no. 203, pp. 545–551, 1997.
- [10] B. V. V. Reddy and A. Gupta, "Strength and elastic properties of stabilized mud block masonry using cement-soil mortars," *Journal of Materials in Civil Engineering*, vol. 18, no. 3, pp. 472–476, 2006.
- [11] R. Illampas, I. Ioannou, and D. C. Charmpis, "Adobe bricks under compression: experimental investigation and derivation of stress–strain equation," *Construction and Building Materials*, vol. 53, pp. 83–90, 2014.
- [12] S. A. Lima, H. Varum, A. Sales, and V. F. Neto, "Analysis of the mechanical properties of compressed earth block masonry using the sugarcane bagasse ash," *Construction and Building Materials*, vol. 35, pp. 829–837, 2012.
- [13] "Soil testing methods of Chinese standards," Tech. Rep. GB/T50123-1999, Standards China, Beijing, China, 1998.
- [14] P. Walker, "Compressive strength of cement stabilized pressed earth blocks," *Building Research and Information*, vol. 30, pp. 545–551, 1997.
- [15] A. Aldaood, M. Bouasker, and M. Al-Mukhtar, "Geotechnical properties of lime-treated gypseous soils," *Applied Clay Science*, vol. 88–89, pp. 39–48, 2014.
- [16] N. Augenti and F. Parisi, "Constitutive models for tuff masonry under uniaxial compression," *Journal of Materials in Civil Engineering*, vol. 22, no. 11, pp. 1102–1111, 2010.

Research Article

Development of an Efficient Steel Beam Section for Modular Construction Based on Six-Sigma

Tae-Hyu Ha,¹ Bong-Ho Cho,² Hongjin Kim,³ and Dae-Jin Kim⁴

¹POSCO, Seoul, Republic of Korea

²Department of Architecture, Ajou University, Suwon, Republic of Korea

³Department of Architectural Engineering, Kyungpook National University, Daegu, Republic of Korea

⁴Department of Architectural Engineering, Kyung Hee University, Yongin, Republic of Korea

Correspondence should be addressed to Bong-Ho Cho; bhcho@ajou.ac.kr

Received 28 September 2016; Accepted 24 October 2016

Academic Editor: Jae-Han Lim

Copyright © 2016 Tae-Hyu Ha et al. This is an open access article distributed under the Creative Commons Attribution License, which permits unrestricted use, distribution, and reproduction in any medium, provided the original work is properly cited.

This study presents a systematic approach for the development of an efficient steel beam section for modular construction based on Six-Sigma. Although the Six-Sigma is frequently implemented in manufacturing and other service industries, it is a relatively new concept in the area of building design and construction. As a first step in this approach, market studies and surveys are conducted to obtain the opinions of potential customers. Then the opinions of customers are converted into quality characteristics for the steel beam using the quality function deployment methodology. A steel hollow flanged channel is chosen as the main modular beam shape, and the design concept is derived and developed by applying the Pugh matrix methodology. A pilot test was performed to validate the effectiveness of the developed beam section. The results indicated that the developed channel beam section showed excellent performance and retained high accuracy in fabrication, thus resulting in a significant reduction of steel consumption.

1. Introduction

Modular construction is an industrialized construction system, with a process that mainly consists of the factory production of preengineered building units, the delivery of the fabricated units to the construction site, and their fast assembly [1]. The structural system of steel frame modular buildings can be largely classified into two types. The first is the beam-column frame system and is suitable for use in school buildings or military barracks, which require relatively large open space [2]. The second is the load-bearing wall system, and dormitories or bachelor officer quarters are good applications of this type as they can be built with a series of transportable unit room modules [3, 4].

In general, the modular unit of the beam-column frame system is constructed by connecting structural members such as corner columns, internal columns, floor beams, and ceiling beams by bolting or welding. Figure 1 illustrates an example of standard modules for elementary schools in Korea. The

dimensions are 9.8 m (length), 7.5 m (column to column span), 3 m (width), and 3.2 m (height). Table 1 provides the composition ratio of the main structural members used in this standard module. In the beam-column frame system, the upper beam of the lower level unit is connected with the lower beam of the upper level unit. This connection scheme is called the double beam system. As a result, beam members make up a larger portion of the structural components of the standard module, which is 81% as shown in Table 1. The beam members play an important role as they not only contribute greatly to the overall construction cost of modular buildings, but also may affect various factors such as story height and floor vibration. Therefore, the selection of adequate beam members is essential to improving the cost efficiency and performance of modular buildings.

Six-Sigma was first developed by Motorola in the 1980s [5] and became well known in the 1990s when Jack Welch made it central to his business strategy at General Electric. Since the late 1990s, most manufacturing companies in Korea

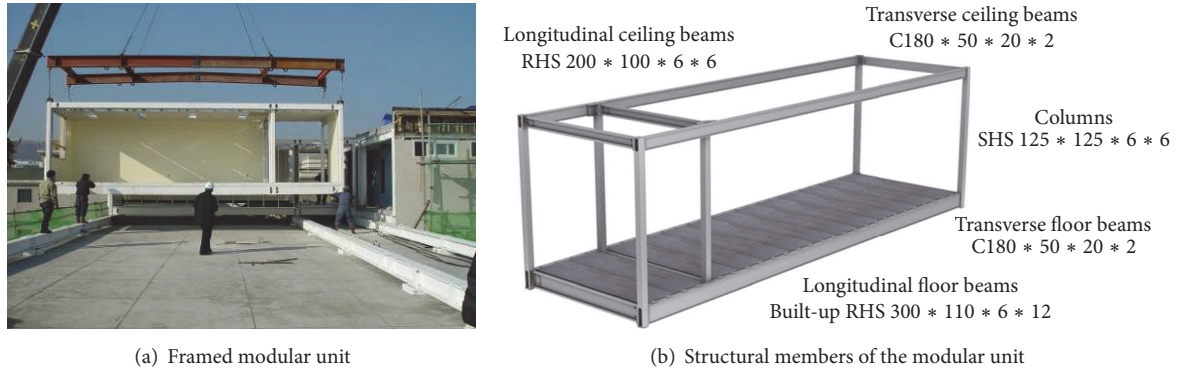


FIGURE 1: Standard modular unit and structural members.

TABLE 1: Composition ratio of main structural members used in the standard module.

Component	Shape	Weight ratio (%)	
Longitudinal floor beams	Built-up rectangular hollow section	41	81
Longitudinal ceiling beams	Rectangular hollow section	32	
Transverse floor and ceiling beams	Roll-formed C shape	7	19
Columns	Square hollow section	19	

have applied the Six-Sigma for productivity enhancement, process improvement, and new product development. While the Six-Sigma has been applied to construction management and housing design on several occasions such as [5, 6], this is one of very few studies where the Six-Sigma concept is employed to develop new steel structural members for modular construction.

In general, Six-Sigma projects follow either the DMAIC or DFSS methodology. The DMAIC focuses on improving an existing business process, while the DFSS aims at creating new products or process designs. Based on this discussion, this study proposes a systematic approach for the development of a steel modular beam section that can be used in the beam-column frame system and validates its effectiveness through a pilot test.

2. QFD Methodology and Derivation of CTQ

2.1. QFD Methodology. The philosophy of the Six-Sigma approach emphasizes the reflection of customers' needs in the development of production processes. In order to achieve this, the identification and categorization of potential customers are required, and the importance of each customer group needs to be evaluated. In the Six-Sigma methodology, these customer requirements are referred to as the voice of customers (VOCs), which are obtained through surveys and interviews and utilized as basic data for product development. According to the results of the interviews, module manufacturers require a decrease in manufacturing cost as well as a

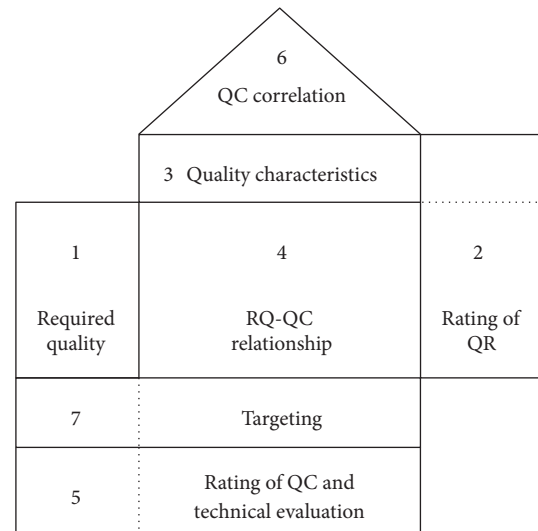


FIGURE 2: HOQ required to conduct QFD.

shortening of order-delivery period, while designers expect various construction-related requirements to be satisfied. The VOC of the building owner is mainly focused on the excellent performance of the manufactured modules.

This study adopts the quality function deployment (QFD) methodology to convert customers' needs into quality characteristics for the products to be developed. The QFD methodology, first proposed by Akao in the 1960s [7], is a tool that can provide a quantitative evaluation on the relation between customer requirements and product characteristics using a correlation matrix [8, 9]. Figure 2 illustrates the house of quality (HOQ), which is required to conduct QFD.

In general, the QFD methodology follows a number of procedures: (1) determination of required quality; (2) importance rating for customers' needs; (3) identification of quality characteristics; (4) correlation analysis between the required quality and quality characteristics; (5) technical evaluation; (6) interrelation analysis of the quality characteristics if required; (7) target specification setup for the quality characteristics. In this study, the required quality is

TABLE 2: Priority rating for the customer requirements.

Customers' required quality	(1) Importance rating	(2) Satisfaction rating	(3) Possible quality levels	(4) Level-up ratio	(5) Sales Point	(6) Absolute priority	Priority Ratios	Ratings
Small steel quantity	4.6	2.8	4	1.4	○	7.7	10%	2
Low manufacturing cost	4.6	2.6	5	1.9	◎	13.1	17%	1
Easy structural design	3.6	3.4	4	1.2		4.3	5%	7
Easy architectural design	3.6	3.4	4	1.2		4.3	5%	7
Easy connection	3.6	3.4	4	1.2		4.3	5%	7
Transportation with low-bed trailer	3.6	3.2	4	1.3		4.7	6%	5
Transportation with cargo truck	3	3	3	1		3	4%	15
Easy installation of plumbing equipment	3.4	3.2	4	1.3		4.4	6%	6
A short time for stocking after order	3.6	2.8	4	1.4	○	6	8%	4
The stock is secured in advance	3	2.6	3	1.2	○	4.3	5%	7
Small manufacturing deformation	3.8	3	4	1.3	◎	7.4	9%	3
Less surface defects	3.6	2.8	3	1.1		4	5%	12
Easy application of high-strength steel	3	2.8	3	1.1		3.3	4%	14
Structural safety	3.6	3.6	4	1.1		4	5%	12
Less floor vibration	4.2	4	4	1		4.2	5%	11

(1) Importance rating: values obtained from customer survey (1~5).

(2) Satisfaction rating: values obtained from customer survey (1~5).

(3) Quality levels that may be obtained from the viewpoint of developers (1~5).

(4) Level up ratio: (3)/(2).

(5) Sales point from the viewpoint of developers (◎: 1.5, ○: 1.2).

(6) Absolute priority: (1)*(4)*(5).

determined from the VOCs obtained from the first round of interviews, and then the quality characteristics are prioritized based on the evaluations of customers and experts. Finally, the target values and importance ratings for the quality characteristics are assigned.

In this study, QFD methodology is used for the development of a new steel modular beam section. The results of priority ratings for the VOCs, where the requirements of both customers and product developers are considered, are provided in Table 2. The item labeled “customers’ required quality” in Table 2 is a reorganization of the VOCs of each customer group for QFD analysis, and its priority ratings are determined based on the results of the customer surveys. From the results of the table, items with high priority are found to have “low manufacturing cost,” “small steel quantity,” “small manufacturing deformation,” and “short time for stocking after order.” In the determination of the priority rating in Table 2, the importance of customers’ requirements and satisfaction with existing products are determined from the surveys. The “planning quality” and “sales point” in Table 2 are the indicators for the attainable quality and sales quantity from the perspective of developers, respectively.

2.2. Derivation of CTQ. From a correlation analysis between the required qualities and quality characteristics, parameters that are critical to quality (CTQ) from the customers’ perspective can be derived. The quality characteristics are given different weight values (◎: 5 points, ○: 3 points, and △: 1 point) depending on the relationship with the corresponding customer requirements. The overall importance can be calculated by summing up the multiplications of the weighted value and absolute importance in Table 3. The quality characteristics with high importance score can be selected as the potential CTQs.

This process of deriving CTQs is important in the Six-Sigma methodology, which reflects the customers’ needs as much as possible. The VOC does not contain any direct statements on the quality characteristic, but it can be converted into designable quality characteristics through QFD analysis. Table 3 lists the importance ratings derived from the correlation analysis on the required quality and quality characteristics.

From the QFD analysis, the quality characteristics with high importance are found to be “weld length per unit length,” “moment of inertia per sectional area of beam,” and “weight of floor beams per unit area of plan.” These items

TABLE 3: Correlation analysis between the required qualities and quality characteristics.

Customers' required quality	Quality characteristic														Priority ratios	Ratings		
	Price of beams				Contribution to competitiveness of modules				Structural performance of beams				Quality of manufacturing					
	Surface area per unit length	Welding length per unit length	Span length	Thickness of webs	Diameter of web opening	Number of webs	Thickness of flanges	Number of openings	Height of ceiling and floor beams	Weight of floor beams per unit area of plan	Moment of inertia per sectional area of beam	Section modulus per sectional area of beam	Lever arm of bolts at the end plate	Number of axes of symmetry	Radius of curved section	Absolute priority	Priority ratios	
Low cost of beams																		
Small steel quantity		⊗		○	○	○	△	○	⊗	⊗	○	○				7.7	10%	2
Low manufacturing cost	○	⊗		○	○	○		○								13.1	17%	1
Easy design of modular building																		
Easy structural design	⊗	⊗	⊗	⊗	○	○	○	○	○	⊗	○	○	⊗	○	○	4.3	5%	7
Easy architectural design	⊗	⊗	⊗	⊗	○	○	○	○	○	⊗	○	○	⊗	○	○	4.3	5%	7
Easy fabrication and transportation				⊗														
Easy connection				⊗				⊗								4.3	5%	7
Transportation with low-bed trailer									⊗							4.7	6%	5
Transportation with cargo truck									⊗				○			3	4%	15
Easy installation of plumbing equipment									⊗				○			4.4	6%	6
Short time for stocking																		
A short time for stocking after order	○	⊗						○								6	8%	4
The stock is secured in advance																4.3	5%	7
High quality of manufacturing																		
Small manufacturing deformation														⊗		7.4	9%	3
Less surface defects															○	4	5%	12
Easy application of high-strength steel	⊗								⊗					○	○	3.3	4%	14
Structural performance																		
Structural safety													⊗			4	5%	12
Small floor vibration									○				⊗			4.2	5%	11
Absolute priority	126	194	116	62	92	90	46	110	95	138	182	72	101	80	48			100%
Priority ratios	8.1%	12.5%	7.5%	4.0%	5.9%	5.8%	3.0%	7.1%	6.1%	8.9%	11.7%	4.6%	6.5%	5.1%	3.1%			
Ratings	4	1	5	13	9	10	15	6	8	3	2	12	7	11	14			

TABLE 4: CTQ definitions and target levels.

CTQ	Definition	Measuring method	Current level		Target level
			Built-up RHS	Channel	
Welding length per unit length	Welding length per 1 m beam length	Measuring welding length	4	0	Less than 2
Moment of inertia per sectional area of beam	Moment of inertia divided by sectional area of beam	Calculation of moment of inertia and sectional area of beams	127 cm ² (7.5 m span)	132 cm ² (7.5 m span)	Larger than 150 cm ² (7.5 m span)
Weight of floor beams per unit area of plan	Total weight of beams used for modules divided by plan area of module	Calculation of weight of beams after redesign of modules	0.30 kN/m ² (7.5 m span)	0.25 kN/m ² (7.5 m span)	Less than 0.28 kN/m ² (7.5 m span)

TABLE 5: Classification of key functions for the steel modular beam section.

Main process	Manufacturing beams	Assembly of modules	Transportation and installing	Ensuring structural performance
Must be functions	—	Welding end-plate Connecting beam and column	Transportation of modules	Flexural strength of beam Shear strength of beam Minimize deflection of beam
		Connecting beam and slab Connecting beam and ceiling track		Minimize floor vibration Earthquake and wind resistance
		Connecting beam and wall track		Fire resistance
Delighter functions	—	—	Plumbing equipment penetration	—
Primary satisfier functions	Minimize a space for stock	—	—	—

are selected as CTQs in the following step and expressed quantitatively. Among the 15 quality characteristics, the top 3 items are selected as CTQs and defined as shown in Table 4, which shows their definitions, measurement methods, current, and target levels. The target levels are determined using the existing built-up RHS (rectangular hollow sections) and channels as references.

3. Product Design Using Pugh Matrix Methodology

3.1. *Function Analysis and Pugh Matrix.* The core functions of the steel modular beam section are determined and its optimal design is developed utilizing the CTQs derived in the previous phase. Table 5 describes the main processes required for the manufacturing of the steel modular beam section and classifies the functions required in each process into one of three functions, namely, the basic function (necessary), attractive function (delighter), and discriminative function (primary satisfier). The basic functions must be satisfied, while the attractive and differentiated functions can be optionally considered in the design process.

Key functions can be determined from a correlation analysis between the quality characteristics and associated functions by applying the same method used to create CTQs in Table 3. Table 6 shows the relationship between the quality

characteristics and the key functions. From this relationship, “minimize deflection and vibration of beam,” “flexural strength of beam,” “earthquake and wind resistance,” and “piping equipment penetration” are selected as key functions.

After derivation of the key functions, an optimal design concept satisfying the derived key functions needs to be developed. In order to achieve this, various methods can be used such as the benchmarking of advanced technologies, brainstorming by experts, TRIZ, and mind mapping. In this study, various solutions that can satisfy the key functions are created, and several possible design options are obtained by combining these solutions. Finally, the Pugh matrix is employed to select the optimal design among the designs obtained.

Table 7 lists the available solutions for each of the key functions of the steel modular beam section. The table indicates that there are two solutions for “piping equipment penetration” and “connecting beam and slab,” four solutions for structural functions, specifically “flexural strength of beam,” “minimize deflection and vibration of beam,” and “earthquake and wind resistance,” and one solution for all of the remaining functions. These solutions can be combined to produce an optimal design concept. By combining the solutions listed in Table 7, seven design concepts are derived. They satisfy various functions required for the floor and ceiling

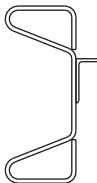
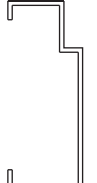
TABLE 6: Correlation between the quality characteristics and key functions.

Quality characteristic	Key function										Secondary function		
	Welding end-plate	Connecting beam and column	Connecting beam and slab	Connecting beam and ceiling track	Connecting beam and wall track	Flexural strength of beam	Minimize deflection and vibration of beam	Earthquake and wind resistance	Fire resistance	Plumbing equipment penetration	Transportation of modules		
Price of beam									⊙				
Surface area per unit length													
Welding length per unit length													
Contribution to competitiveness of module													
Span length													
Thickness of webs			⊙	⊙									
Diameter of web opening													
Number of webs	○	⊙	○	○									
Thickness of flanges													
Number of openings													
Height of ceiling and floor beams													
Weight of floor beams per unit area of plan													
Structural performance of beam													
Moment of inertia per sectional area of beam													
Section modulus per sectional area of beams													
Lever arm of bolts at the end plate	⊙	⊙											
Quality of manufacturing													
Number of axes of symmetry													
Radius of curved section			⊙	○									
Priority ratio	6.5%	9.5%	8.6%	6.7%	4.7%	16.7%	19.7%	11.9%	0.6%	10.1%	4.8%		
Rating	8	5	6	7	10	2	1	3	11	4	9		

TABLE 7: Available solutions for each of the key functions.

Key functions	Solutions			
Piping equipment penetration	Install reinforcing device at penetration Solution A		Penetrate without reinforcing Solution B	
Transportation of modules	Limiting module height less than 3.3 m			
Welding end-plate	Limiting flange width less than 120 mm			
Connecting beam and column	Ensuring bolting space at end-plate			
Connecting beam and slab	Integrate beam and slab support Solution a		Separate beam and slab support Solution b	
Connecting beam and ceiling track	Connect track to web of beam with screw			
Connecting beam and wall track	Ensuring flange width of 60 mm			
Flexural strength of beam	Use hollow flange (flange thickness = web thickness) Solution I	Use hollow flange (flange thickness > web thickness) Solution II	Use open flange (flange thickness = web thickness) Solution III	Use open flange (flange thickness > web thickness) Solution IV
Minimize deflection and vibration of beam				
Earthquake and wind resistance				

TABLE 8: Design concepts obtained by combinations of the available solutions.

Combination of solutions	Solutions A + a + I	Solutions A + b + I	Solutions A + a + II	Solutions A + b + II	Solutions B + a + III	Solutions B + b + III	Solutions B + b + IV
Design concepts							
Manufacturing cost	Very high	High	Very high	Very high	Middle	Middle	Very high
Steel quantity	Very low	Low	Very low	Very low	Low	High	Low
Compatibility between floor and ceiling beam	Not compatible	Compatible	Not compatible	Compatible	Not compatible	Compatible	Compatible

beams of the modular beam-column frame system and show different characteristics with regard to manufacturing cost, steel consumption, and availability for both of ceiling and floor beams. Their characteristics are summarized in Table 8.

In order to select the optimal design among the candidates listed in Table 8, a Pugh matrix is created in Table 9. In this methodology, a relative evaluation is performed on each candidate by comparing it with the reference design for each of the key criteria. The built-up RHS is chosen as the reference design for this comparison. Thus, if a candidate shows better performance than the reference design, it is denoted as +. If the candidate is worse than or is equal to the reference design, it is denoted as - or S, respectively. The candidate with the greatest difference between the sum of pluses and that of minuses is chosen as the optimal design. The results in Table 9 indicate that design concept 2 is the optimal design. Thus, it is selected as the prototype for the steel modular beam section.

The prototype has hollow flanges in both the upper and lower parts of the section as shown in Table 9. It can be manufactured by a roll forming method, in which thin steel sheets are passed through several rolls and are consecutively bent at room temperature. The cross-sectional shape is illustrated in Figure 3. The steel beam member with the cross-sectional shape shown in Figure 3 is hereafter referred to as the modular construction optimized (MCO) beam for convenience.

3.2. Detailed Design of MCO Beams. In this section, a detailed design of the MCO beam is discussed considering the manufacturing process. With the detailed design components, the cross-section has a variable portion as well as an invariable portion as shown in Figure 4. Although MCO beams manufactured through the roll forming process require smaller manufacturing costs than general built-up beams, a variety in depth is also necessary for their applications to modular

TABLE 9: Selection of the optimal design using the Pugh matrix methodology.

Key criteria	Weight	Reference	Concept 1	Concept 2	Concept 3	Concept 4	Concept 5	Concept 6	Concept 7
		Better + Same S Worse -							
Manufacturing cost	5	S	+	+	S	S	+	+	-
Fire proofing cost	4	S	-	-	-	-	-	-	-
Steel quantity	4	S	+	+	+	+	-	-	+
Easy fabrication	3	S	+	+	+	+	+	+	+
New investment	5	S	-	-	-	-	+	+	-
Compatibility	4	S	-	+	-	+	-	+	-
Creativity	3	S	+	+	+	+	S	S	S
Sum of +		0	4	5	3	4	3	4	2
Sum of -		0	3	2	3	2	3	2	4
Sum of S		7	0	0	1	1	1	1	1
Weighted sum of +		0	15	19	10	14	13	17	7
Weighted sum of -		0	13	9	13	9	12	8	18

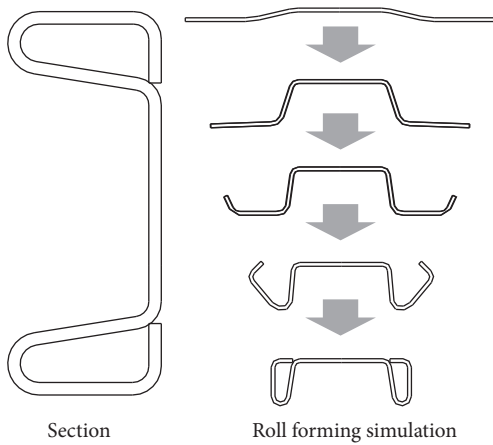


FIGURE 3: Cross-sectional shape of the MCO beam and its roll forming simulation.

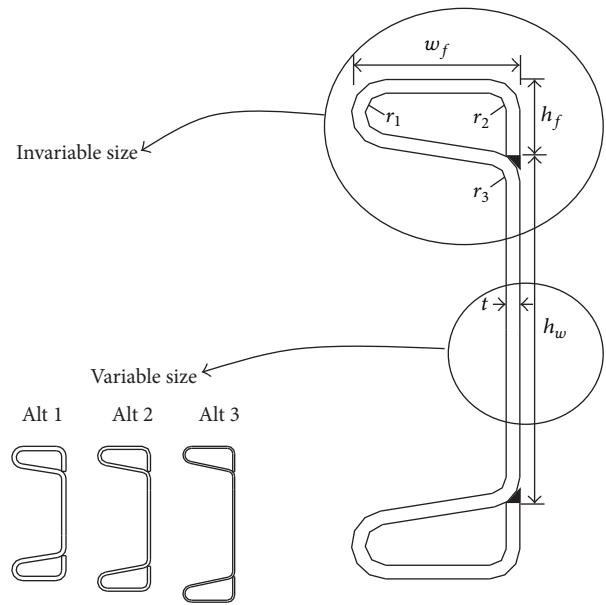


FIGURE 4: Cross-sectional design of the MCO beam.

buildings with diverse spans. Therefore, the upper and lower hollow flange parts are designed as the invariable portion and produced using a single roll. In contrast, the thickness and width of the web section are variable. The design requirements for each design factor of the MCO beam are listed in Table 10. SPA-H steel is used for manufacturing the MCO beams since it has high durability as well as a high tensile strength of 490 MPa.

The design procedures for the MCO beam with invariable cross-section (hollow flange) can be summarized as follows.

Step 1 (setting up the range of the flange width as shown in Figure 5). (i) If the minimum width of the column is 125 mm, the flange width is in the range of 100~120 mm.

(ii) The minimum width of the horizontal flat flange portion must be at least 50 mm.

Step 2 (determination of r_1 and r_2 shown in Figure 6). These parameters are constant regardless of the steel plate thickness if the same roll forming process is used.

(i) Bending capacity of SPA-H steel: if the bending angle is 180 degrees, the inner radius must be at least 1.5 times the flange thickness.

TABLE 10: Design requirements for each design factor of the MCO beam.

Design factor	Design requirement
Invariable section	
Flange width	(i) Limit the flange width to less than the column width (column width: 125 mm or 150 mm) (ii) Require the minimum flat flange width (50 mm) to be connected to the wall stud
Radius of curved section	(i) Minimum radius of curved section less likely to cause a crack
Flange height	(i) Flange to thickness ratio is larger than 61 ($h_f > (h - 61t)/2$)
Welding length	(i) Prevent local buckling
Variable section	
Thickness of steel plate	(i) Variable sections for variable floor loads and spans
Web height	(i) Variable sections for variable floor loads and spans (ii) Able to penetrate pipes

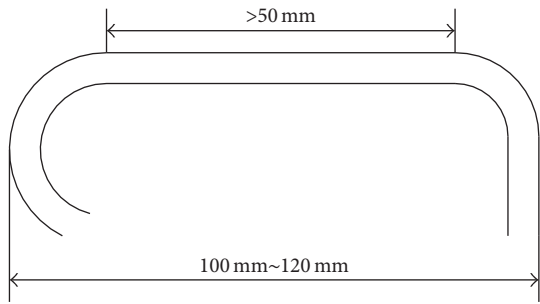


FIGURE 5: Range of the flange width.

- (ii) The maximum steel plate thickness is limited to 10 mm.
- (iii) If the bending angle of r_1 is in the range of 90 to 180 degrees, $r_1 = 15$ mm.
- (iv) If the bending angle of r_2 is 90 degrees, $r_2 = 12$ mm.

Step 3 (determination of the flange width). (i) If the steel plate thickness is 10 mm and r_1 and r_2 are 15 and 12 mm, respectively, the flat flange width is in the range of 53 to 73 mm, thus satisfying the condition in Step 1.

(ii) The flange width is determined as 120 mm, which is the maximum value allowed by the condition in Step 1, considering its easy attachment onto ceilings and floor tracks.

Step 4 (determination of r_3). This value is constant if the same roll forming process is used regardless of the flange thickness.

- (i) If bending angle of r_3 is less than 90 degrees, $r_3 = 12$ mm, which is the same as r_2 .

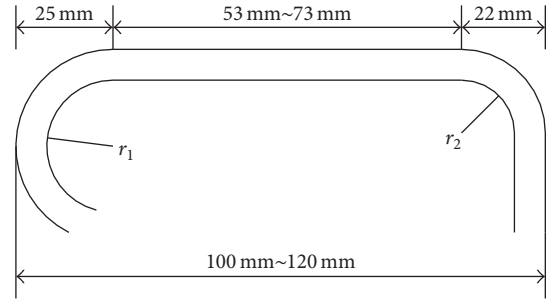


FIGURE 6: Determination of r_1 and r_2 .

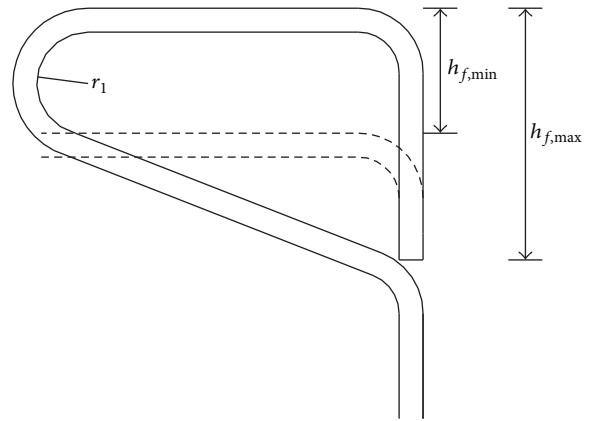


FIGURE 7: Determination of the flange height.

Step 5 (setting up the range of the flange height shown in Figure 7). (i) If it is assumed that the upper and lower flanges are parallel to each other and the flange thickness is 10 mm, $h_{f,min1} = 10 + 15 + 15 + 10 = 50$ mm.

(ii) The flange height can be calculated by considering the maximum beam height of 400 mm and minimum steel plate thickness of 4.5 mm and applying the maximum width-thickness ratio of 61 to prevent elastic local buckling as $h_{f,min2} = (400 - 61 \times 4.5)/2 = 63$ mm.

Step 6 (final selection of invariable dimensions of the upper hollow flange). (i) Front welding is performed on the steel plate connection as shown in Figure 8.

The following design conditions for the variable portion of the MCS beam cross-section are assumed for three module spans of 6, 7.5, and 8.1 m: floor beam load in the range of 2~5 kN/m², floor beam live load in the range of 2~5 kN/m², ceiling beam load in the range of 0.3~0.5 kN/m², and ceiling beam live load in the range of 0.5~1 kN/m². Various cross-sectional shapes for the MCO beam are designed by changing the steel plate thickness and web height as design variables, while satisfying the requirements on the dimensions of the cross-section discussed above. As shown in Table 11, 6 steel plate thickness values and 7 web heights are used as design values. The effective moment of inertia for the cross-sections

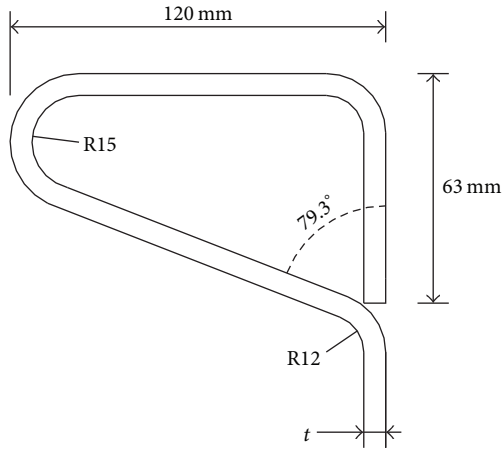


FIGURE 8: Invariable dimensions of the upper hollow flange of the MCO beam.

TABLE 11: Design requirements and values on the variable sectional portion of the MCO beam.

Design factors	Design requirements	Design values
Thickness of steel plate	Use standard steel products	(i) 4.5 mm, 6 mm, 7 mm, 8 mm, 9 mm, 10 mm
Depth of beam	Apply modular coordinate	(i) Floor beam: 270 mm, 300 mm, 330 mm, 360 mm, 390 mm (ii) Ceiling beam: 200 mm, 240 mm

in the table ranges from 1,530 to 18,218 cm⁴. A total of 42 of the designed MCO beam cross-sectional shapes are given in Figure 9.

4. Design Verification and Pilot Test

As the final stage of the DFSS methodology, MCO beam rolls are produced using the roll forming facilities of a local company in Korea, and their formability and welding workability are assessed. Figure 10 shows the procedure for a pilot production of the MCO beam sections developed. A long strip in coiled steel is passed through sets of rolls until a shape with upper and lower hollow flanges is obtained. Then the production of the MCO beam section is completed by performing welding on the roll formed shape. Figure 11 shows an example of the assembled modular unit with the produced MCO beams.

The results of CTQ and productivity assessments on the final products are summarized in Table 12. The deformation level of the MCO beam that occurs during its production is less than 5 mm per 10 m. While some deformation may take place during secondary machining such as welding of brackets and end plates, additional correction can be performed in the process of module assembly, resulting in an error less than 3 mm per unit module. To confirm that

the produced beams have a sufficient moment of inertia per unit cross-sectional area, a total of 150 cases are tested for various floor spans and loading conditions. The results of the test show that the average floor span is 183.38 cm² and the standard deviation is 16 cm². Thus, the average is well above the design target, which is 160 cm². For three spans of 6, 7.5, and 8.1 m, floor beams with optimal cross-sections are selected, and then the weight of the floor beams per unit area is evaluated for each case. It can be seen from the results of the table that target values are met for all of the three cases.

5. Concluding Remarks

In this study, a systematic approach was presented for the development of an efficient steel beam section for modular construction based on Six-Sigma. As the first step of this approach, market studies and surveys are conducted to obtain the opinions of potential customers. Then the opinions of the customers were converted into the quality characteristics for the channel-shaped steel beam using the quality function deployment methodology. A steel hollow flanged channel was chosen as the main modular beam shape, and the design concept was derived and developed by applying the Pugh matrix methodology. A pilot test was performed to validate the effectiveness of the developed beam section. The main conclusions of this study are as follows:

- (1) To reflect customers' needs in the development of production processes, the QFD methodology was applied, and "welding length per unit length," "moment of inertia per sectional area of beam," and "weight of floor beams per unit area of plan" were selected as CTQs. Quantitative target values for these items were also set up.
- (2) Seven design concepts were developed from an analysis on the key functions of the steel modular beam to satisfy the derived CTQs. The Pugh matrix methodology was applied to derive the optimal design of the steel modular beam, which has hollow flanges at the top and bottom.
- (3) In the final product design, the cross-section of the MCO beam has the upper and lower hollow flange parts as the invariable portion and the web section as the variable portion. The results of the pilot production of the MCO beam indicate that the weight of the floor beams per unit area can be reduced to an average of 0.25 kN/m² for the standard 7.5 m span, which is 18% less than the corresponding value for the built-up RHS beam. All the modules assembled with the MCO beam products show an error less than 3 mm per unit module, thus satisfying the target value.
- (4) Based on the DFSS methodology of Six-Sigma, this study proposed a methodology which can effectively reflect customers' needs, such as the reduction of manufacturing cost, less material usage, and reduced structural deformation of modular units, in the product design. It is expected that the proposed method

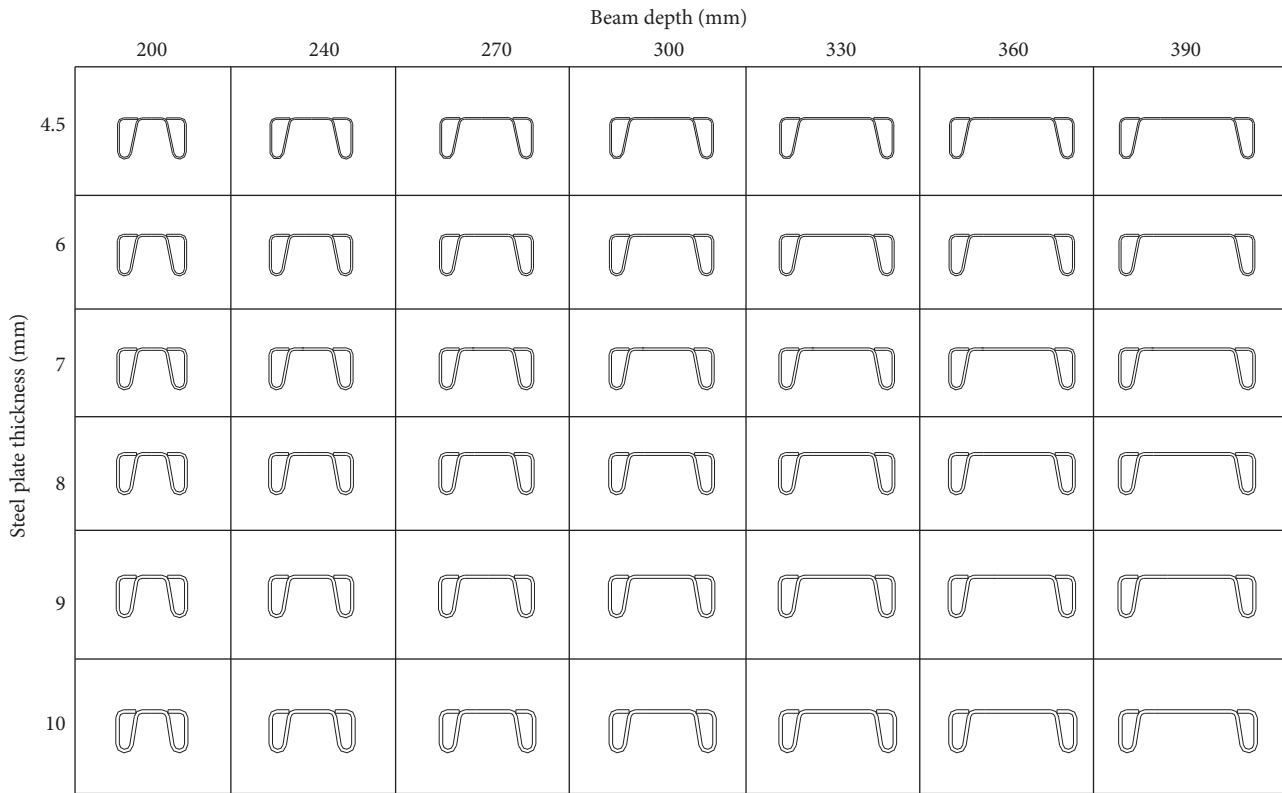


FIGURE 9: Developed cross-sectional shapes for the MCO beam.



FIGURE 10: Pilot production process for the developed MCO beam.

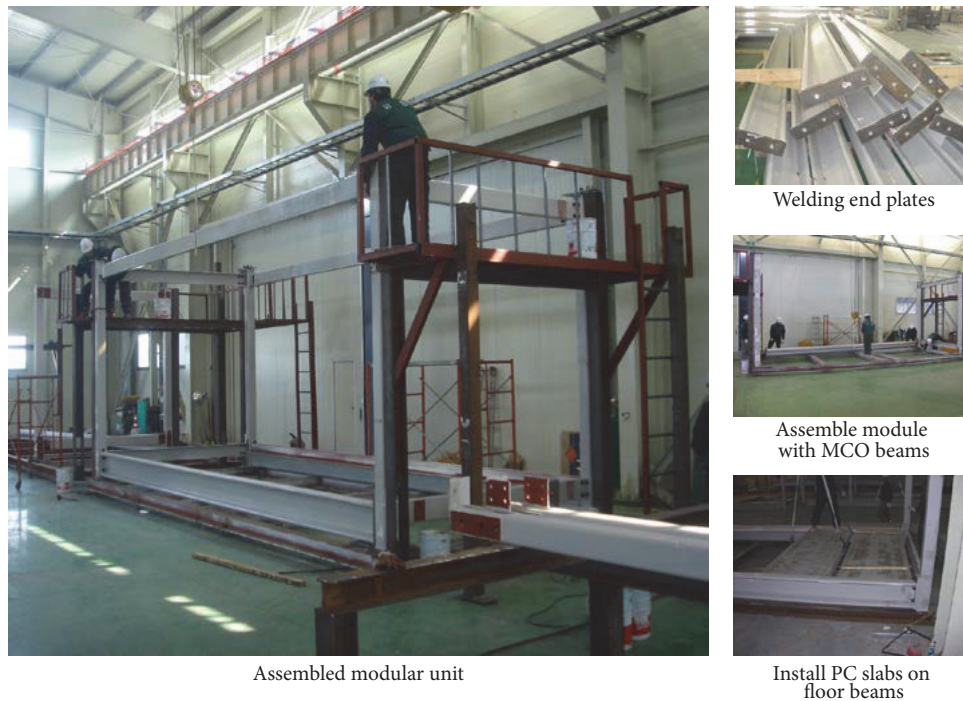


FIGURE 11: Assembled modular unit with the produced MCO beams.

TABLE 12: Design targets and test results for the produced MCO beams.

Design factors	Design targets	Test results
Verification of CTQ		
Welding length per unit length (m/m)	Less than 2	2
Moment of inertia per unit sectional area of beam (cm ²)	Larger than 150	Average 183.86
Weight of floor beams per unit area (kN/m ²)		
6 m span	Less than 0.25	0.18
7.5 m span	Less than 0.28	0.25
8.1 m span	Less than 0.35	0.32
Pilot test		
Pilot production of beam	Flexural deformation is less than 0.05%	Less than 0.05%
Pilot assembly of module	Tolerance of 3 mm	Less than 3 mm

can be utilized to develop other types of structural modular beams and can satisfy the diverse requirements of different customer groups.

Competing Interests

The authors declare that there is no conflict of interests regarding the publication of this article.

Acknowledgments

This research was supported by a grant from the National Research Foundation of Korea (Grant no. NRF-2016 RID1A1B01010615).

References

- [1] R. M. Lawson, R. G. Ogden, and R. Bergin, "Application of modular construction in high-rise buildings," *Journal of Architectural Engineering*, vol. 18, no. 2, pp. 148–154, 2012.
- [2] S.-G. Hong, B.-H. Cho, K.-S. Chung, and J.-H. Moon, "Behavior of framed modular building system with double skin steel panels," *Journal of Constructional Steel Research*, vol. 67, no. 6, pp. 936–946, 2011.
- [3] H.-J. Kim, J.-S. Lee, H.-Y. Kim, B.-H. Cho, Y. Xi, and K.-H. Kwon, "An experimental study on Fire resistance of medical modular block," *Steel and Composite Structures*, vol. 15, no. 1, pp. 103–130, 2013.
- [4] T.-S. Eom, T.-H. Ha, B.-H. Cho, and T.-H. Kim, "Cyclic loading tests on framed stud walls with strap braces and steel sheathing,"

Journal of Structural Engineering, vol. 141, no. 7, Article ID 04014173, 2015.

- [5] L. S. Pheng and M. S. Hui, "Implementing and applying six sigma in construction," *Journal of Construction Engineering and Management*, vol. 130, no. 4, pp. 482–489, 2004.
- [6] J. A. Johnson, H. Gitlow, S. Widener, and E. Popovich, "Designing new housing at the University of Miami: a 'six sigma'© DMADV/DFSS case study," *Quality Engineering*, vol. 18, no. 3, pp. 299–323, 2006.
- [7] Y. Akao, "Development history of quality function deployment," *The Customer Driven Approach to Quality Planning and Deployment*, 1994.
- [8] A. Hassan, A. Siadat, J.-Y. Dantan, and P. Martin, "Conceptual process planning an improvement approach using QFD, FMEA, and ABC methods," *Robotics and Computer-Integrated Manufacturing*, vol. 26, no. 4, pp. 392–401, 2010.
- [9] J. Chun and J. Cho, "QFD model based on a suitability assessment for the reduction of design changes in unsatisfactory quality," *Journal of Asian Architecture and Building Engineering*, vol. 14, no. 1, pp. 113–120, 2015.

Research Article

Structural Behavior of Reinforced Self-Compacted Engineered Cementitious Composite Beams

**Bashar S. Mohammed,¹ M. F. Nuruddin,¹ Muhammad Aswin,¹
Nursyuhada Mahamood,¹ and Hashem Al-Mattarneh²**

¹*Department of Civil and Environmental Engineering, Universiti Teknologi PETRONAS, 32610 Bandar Seri Iskandar, Perak Darul Ridzuan, Malaysia*

²*Civil Engineering Department, Najran University, Najran 11001, Saudi Arabia*

Correspondence should be addressed to Bashar S. Mohammed; bashar.mohammed@petronas.com.my

Received 1 July 2016; Revised 6 September 2016; Accepted 29 September 2016

Academic Editor: Jae-Han Lim

Copyright © 2016 Bashar S. Mohammed et al. This is an open access article distributed under the Creative Commons Attribution License, which permits unrestricted use, distribution, and reproduction in any medium, provided the original work is properly cited.

Eight large-scale reinforced self-compacted engineered cementitious composite (R-SC-ECC) beams with different steel reinforcement ratios have been designed, prepared, cast, cured, and tested to failure at the age of 28 days. The experimental results have been compared with theoretical values predicted using EC2, RILEM, and VecTor2 models. Results show that failure modes in flexure and shear of R-SC-ECC beams are comparable to that of normal reinforced concrete beam. Nevertheless, contrary to VecTor2, models of EC2 and RILEM are not suitable for predicting reasonable ultimate moments for the beams, while results using VecTor2 model have successfully predicted the failure modes and load-deflection curves for all R-SC-ECC beams. It has been concluded that R-SC-ECC fall in the category of ductility class medium to high which gives advantages of using R-SC-ECC beams in regions susceptible to seismic activities.

1. Introduction

The structural applications for plain concrete are limited due to its low tensile strength, low strain capacity, and brittle behavior. Therefore, steel bars have been introduced to resist the tensile stress and achieve ductile behavior of reinforced concrete (RC) element, and, consequently, RC has become a dominant construction material. However, in some structural applications, such as link slab for jointless bridge deck, connection joints, slabs under indentation load, and RC elements subjected to seismic loading, high steel reinforcement ratio is required [1, 2]. This led to unnecessary stiffening of the RC elements and also causes difficulties in proper compaction of fresh concrete around steel bars during concreting which in turn adversely affects the RC composite action. Therefore, fibers have been added to concrete to increase tensile strength and strain capacity and also improve ductility, which subsequently reduces the steel reinforcement ratio in RC elements. To attain tensile elastic-strain hardening behavior accompanied by multiple cracks, high performance fiber

reinforced cementitious composites (HPFRCCs) containing 4% to 20% fibers have been developed [3]. However, researchers reported problems of HPFRCCs such as poor workability, less homogeneity, and fibers balling occurrence [1, 2]. Engineered cementitious composite (ECC) is a special class of HPFRCCs [4]. Unlike HPFRCCs, ECC requires much lower fibers, not greater than 2% volume fraction of polymeric fibers for comparable mechanical properties. ECC has high tensile strength from 4 to 6 MPa [4] and large strain capacity between 3% and 5% [5] and also exhibits high ductility by optimizing the microstructure of the composite [6]. In addition, ECC has the ability to confine crack width up to an average of less than 60 microns up to failure [7]. Further details on ECC properties and behavior have been reported by other researchers [8–11]. On the other hand, self-compacted concrete (SCC) is nonsegregating, nonbleeding, and highly cohesive concrete [12]. It has super fluidity that enables it to fill the formworks by its gravity completely, achieving adequate consolidation and encapsulating reinforcement

TABLE 1: Mix proportions of SC-ECC.

Ingredients	Amount
Cement (OPC), kg/m ³	583
Fly Ash, kg/m ³	700
Fine aggregate, kg/m ³	467
Water-cement ratio	0.32
Polyvinyl alcohol, %	2
Super plasticizer, kg/m ³	9.5

without external mechanical compaction [13]. Other advantages have been also reported on using SCC; for example, it requires a smaller number of workers in pouring concrete and it has reduced noise level associated with vibrating of normal concrete, better durability, time-saving property, and better quality [12–14]. Therefore, the main objective of the work presented in this paper is to investigate the structural behavior of large-scale reinforced self-compacted engineered cementitious composite (R-SC-ECC) beams. Theoretical models such as Eurocode2 model for high strength concrete, RILEM model for fiber reinforced concrete, and finite element VecTor2 model have been investigated as well. Theoretical values have been compared with the experimental results to evaluate their suitability and accuracy in predicting the structural performance of R-SC-ECC beams.

2. Experimental Works

Eight large-scale R-SC-ECC beams were prepared, cast, cured, and tested up to failure at the age of 28 days. All beams have a rectangular cross section of 150 mm breadth and 300 mm height, with a total span length of 2600 mm and effective span (center to center of supports) of 2300 mm.

2.1. Mix Proportions. To improve quality of hardened ECC and also create a better working environment, self-compacting ECC (SC-ECC) has been developed. The necessity of using SC-ECC is to ensure the flow ability of the ECC under its own weight in narrow steel-congested sections. This is important to avoid bleeding and segregation of fresh ECC and also to ensure optimum bonding with steel bars and honeycomb free of hardened ECC. As shown in Table 1, a mix proportion of SC-ECC has been selected and prepared in accordance with the requirements of ACI committee 211.2-98, while the mixing procedure is described by Mohammed et al. [6]. To assess the fresh properties of the SC-ECC, four tests have been conducted: slump flow, $T_{50\text{cm}}$ slump flow, V-funnel, and L-box. Test results are shown in Table 2; the ECC mixture has fresh properties satisfying the self-compacting requirements as shown in Table 3. Samples of the SC-ECC have been prepared, cast, cured, and tested at the age of 28 days to determine the hardened properties as shown in Table 4. Experimental setup for the flexural, compression stress-strain, and direct tensile tests can be seen in Figures 1, 2, and 3. In addition, the air dry density has been found to be 2204 kg/m³.



FIGURE 1: Flexural test for ECC.



FIGURE 2: Compression stress-strain test for ECC.

2.2. Test Specimens. In reinforced concrete (RC) design, concrete tensile strength is assumed as zero; therefore, all tensile forces (below neutral axis of the section) are to be resisted by steel reinforcement in tension. This assumption is true for normal concrete which usually has very low tensile strength. However, fiber reinforced concrete has a more significant value of tensile strength. ECC is a special type of fiber reinforced concrete and exhibits property of steel-like behavior. With the increase of using reinforced ECC components in construction industry, it is important to evaluate the suitability of fiber reinforced concrete (FRC) design models to be used in the design of reinforced ECC members. To achieve this objective, eight large-scale reinforced SC-ECC beams have been designed, prepared, cast, cured, and tested up to failure at the age of 28 days. In view of a single variable as steel reinforcement ratio, all beams have the same cross-sectional area with dimensions of 150 mm width and 300 mm overall height. In this study, the required longitudinal steel reinforcement was determined according to the requirements of EC2 (Section 9.2.1.1). The area of longitudinal steel reinforcement provided in each beam is greater than 112.4 mm² and is not

TABLE 2: Fresh SC-ECC testing.

Slump flow		V-funnel		L-box	
Slump flow diameter (mm)	T_{50} (sec)	t_v (sec)	h_1 (mm)	h_2 (mm)	h_2/h_1
788.5	3	7	102	94	0.92

TABLE 3: Test methods for evaluating the fresh properties of self-compacted concrete.

Test method	Test purpose	Typical range	
		Minimum	Maximum
Slump flow	Viscosity/flow ability	650 mm	800 mm
T_{50} slump flow	Viscosity/flow ability	2 sec	5 sec
V-funnel	Filling ability	6 sec	12 sec
L-box (h_2/h_1)	Passing ability	0.8	1.0



FIGURE 3: Direct tensile test for ECC.

less than 54.6 mm^2 , which is the minimum area of steel reinforcement and is less than the maximum area of steel reinforcement, 1800 mm^2 . Variations of steel reinforcement ratio (ρ) were taken based on the amount of longitudinal steel reinforcement utilized. The steel reinforcement details of beams are shown in Table 5. To support the aim of this study, fiber-full fraction ECC section along the beam has been utilized, while steel reinforcement ratio (ρ) was varied. This is to obtain the effect of various steel reinforcement ratios against ultimate moment capacity, load-deformation relationship, and ductility ratio. The ultimate moment capacity of R-SC-ECC beams was investigated using different design models to achieve an appropriate design model in the designing of reinforced ECC beams.

The shear span (a_p) and concrete cover are kept constant as 766 mm and 20 mm, respectively. Shear design has been carried out in accordance with the requirement of EC2 and shear links are placed along the beam. Closed 8 mm diameter link has been used with spacing of 60 mm center/center to accommodate the shear requirement.

For each beam, two strain gages have been placed on the main tension bars to measure the tensile strains, while

the concrete strain gages have been placed at one side of the beams' surfaces to measure the flexural strains development of SC-ECC during the test. The schematic diagram of the experimental setup is shown in Figure 4. The R-SC-ECC beams have been tested as simply supported using four-point flexural arrangement and constant loading rate of 0.1 kN/sec up to failure. Linear Variable Differential Transducers (LVDTs) have been positioned at the soffit of the beams to measure deflections.

3. Results and Discussion

3.1. Ultimate Moment Capacity. Moment capacity of the beam is the ultimate design moment that brings the beam to the maximum point. Various design codes adopt different safety factors in calculating the moment capacity. However, for normal reinforced concrete, tensile strength of concrete below neutral axis of the equivalent-rectangular stress block is assumed as zero. Therefore, the tensile concrete is negligible and only steel reinforcement in tension is supposed to resist the applied tensile forces, while, for reinforced-fiber reinforced concrete (R-FRC), both reinforcement and FRC are supposed to resist the applied tensile forces as shown in Figure 5. The moment capacity of FRC with ordinary reinforcing bars according to RILEM stress-strain relationship can be computed using

$$M_n = A_s f_y \left(d - \frac{a}{2} \right) + f_{ft} (h - x) b z, \quad (1)$$

where A_s is the area of tension steel reinforcement, f_y is the yield strength of steel reinforcement, d is the effective depth of the section, x is the depth of the neutral axis, $a = \beta_1 x$, β_1 is the coefficient of compressive stress block, f_{ft} is tensile strength of FRC, h is the overall height of the section, z is the internal lever arm and is equal to $0.5(h - x) + x(1 - \beta_1/2)$, and b is the width of the section.

The EC2 [16] model is shown in Figure 6. Using ECC with compressive strength of 86.5 MPa, $0.463 f_{ck} b s = 0.87 f_{yk} A_s$, where $s = 0.71x$; therefore, the ultimate moment capacity is computed using

$$M = F_{st} \times z. \quad (2)$$

Under reinforcement beam, the steel reinforcement is yielded if $x \leq x_b$, where x is the depth of neutral axis and x_b is the depth of neutral axis for balance condition. To determine x_b for the R-ECC section (Figure 7), ultimate strain of ECC, $\epsilon_{cu2} = 0.0026$ (from Table 3.1 of the EC2), and yield strain, ϵ_y , for steel bars diameters 10, 12, and 16 mm are 0.00235, 0.00222, and 0.00243, respectively.

Finite element modelling package of VecTor2 [17] has also been used in the analysis of R-ECC beams in this study.

TABLE 4: Properties of hardened ECC.

SC-ECC hardened property	Testing method	Number of samples and size	Unit	Average of the three samples
Compressive strength	ASTM C39/C39M-04 A	3 cylinders of 100 mm dia. and 200 mm height	MPa	86.5
Splitting tensile strength	ASTM C496/C496M-04	3 cylinders of 100 mm dia. and 200 mm height	MPa	6.18
Flexural strength	ASTM C293-02	3 beams of 100 × 24 × 500 mm	MPa	10.42
Elastic modulus	ASTM C469-02	3 cylinders of 100 mm dia. and 200 mm height	GPa	22
Direct tensile strength	ASTM C 39; ASTM E 4	3 samples with the prism dog bone shape	MPa	4.87

TABLE 5: Steel reinforcement details of R-SC-ECC beams.

Beam number	Steel bar reinforcement	Yield stress (MPa)	Section area (mm ²)	$\rho = 100A_s/bd$ (%)
B1	2 ϕ 12	443	226.19	0.558
B2	2 ϕ 10	470	157.08	0.388
B3	2 ϕ 16	486	402.12	0.993
B4	2 ϕ 12 + 1 ϕ 10	443; 470	304.7	0.752
B5	2 ϕ 16 + 1 ϕ 12	486; 443	515.2	1.272
B6	3 ϕ 16	486	603.2	1.49
B7	4 ϕ 16	486	804.2	1.986
B8	4 ϕ 16 + 1 ϕ 12	486; 443	917.29	2.03

VecTor2 is a nonlinear finite element package to analyse two-dimensional reinforced concrete members. It has been theoretically developed and experimentally verified to predict load-deformation response for reinforced concrete elements which exhibit good crack distribution when subjected to short-term static monotonic, cyclic, and reverse cyclic loading.

The theoretical bases of VecTor2 are the Modified Compression Field Theory (MCFT) [18] and the Disturbed Stress Field Model (DSFM) [19], in which analytical models are subjected to normal and shear stresses for predicting the response of reinforced concrete elements. VecTor2 deals with cracked concrete as an orthotropic material with smearing and rotating cracks. MCFT assumes that the rotations of principle stress and strain fields are equal ($\theta = \theta_\sigma = \theta_\epsilon$), so that the prediction of shear stiffness and strength is always overestimated. DSFM can address the systematic deficiencies of MCFT, where the rotation of principal stress field tends to lag compared with the greater rotation of principal strain field ($\theta_\sigma < \theta_\epsilon$). Therefore, VecTor2 is an appropriate package for analysing reinforced ECC as it contains concrete, reinforcement, and bond models which can be selected based on trial and error to obtain the most appropriate model. A total of 628 elements have been used in the developing of R-ECC beams model. Three types of elements have been utilized, which are 264 rectangular elements, 216 triangular elements, and 148 truss elements, with total nodes of 439.

As shown in Table 6 and Figure 8, the ratios of ultimate moment using VecTor2 model to experimental results are closer to 1 compared to RILEM and EC2 models. This is due to the ability of VecTor2 model to accommodate the actual properties of ECC which contributes to the accurate prediction of R-ECC beams behavior. RILEM model conservatively predicts the ultimate moments of R-ECC beams for small steel reinforcement ratio up to 0.752, while for higher ratios the model underestimates the moments. This is due to the

increase in the steel reinforcement ratio which leads to the increase of x as well, which leads to a decrease in the ECC tensile force ($F_{fc,t}$) as shown in

$$F_{fc,t} = f_{ft} (h - x) b. \quad (3)$$

However, EC2 model has failed to predict reasonable moment capacity due to negligence of tensile strength of the ECC as the model assumes that tensile strength of ECC is equal to zero.

3.2. Failure Modes and Crack Pattern. Two failure modes have been observed from testing R-SC-ECC beams, which are flexural failure for beams B1 to B6 as shown in Figure 9 and shear failure mode for beams B7 and B8 as shown in Figure 10. In general, the flexural failure of R-SC-ECC beams is comparable to that of normal reinforced concrete beams. Vertical hair cracks first appeared at the constant-moment zone. Due to the test loading increase, hair cracks extended upward and became more inclined toward the center of the beams combined with increasing cracks thickness until main steel bars yielded. The yielding of the steel bars is marked by the beams failure; however, beams continued to resist the applied load until the crushing of ECC occurred in the compression zone [20]. Yielding strain of longitudinal steel reinforcement has been surpassed in beams B1 to B6 as shown in Figure 11. The general requirement of EC2 is that RC crack width, W_{max} , shall be limited so that it does not adversely affect the durability or functioning or appearance of the structure. Therefore, from Table 7.2N of EC2, the maximum theoretical crack width for beams B1, B2, and B4 is 0.3 mm and for beams B3, B5, and B6 is 0.4 mm. For cracking control, the minimum area of longitudinal steel reinforcement provided in each beam has been satisfied in accordance with the requirements of EC2 (Section 9.2.1.1). However, as shown in Table 7, flexural crack widths of R-SC-ECC beams at service loads have exceeded the limit.

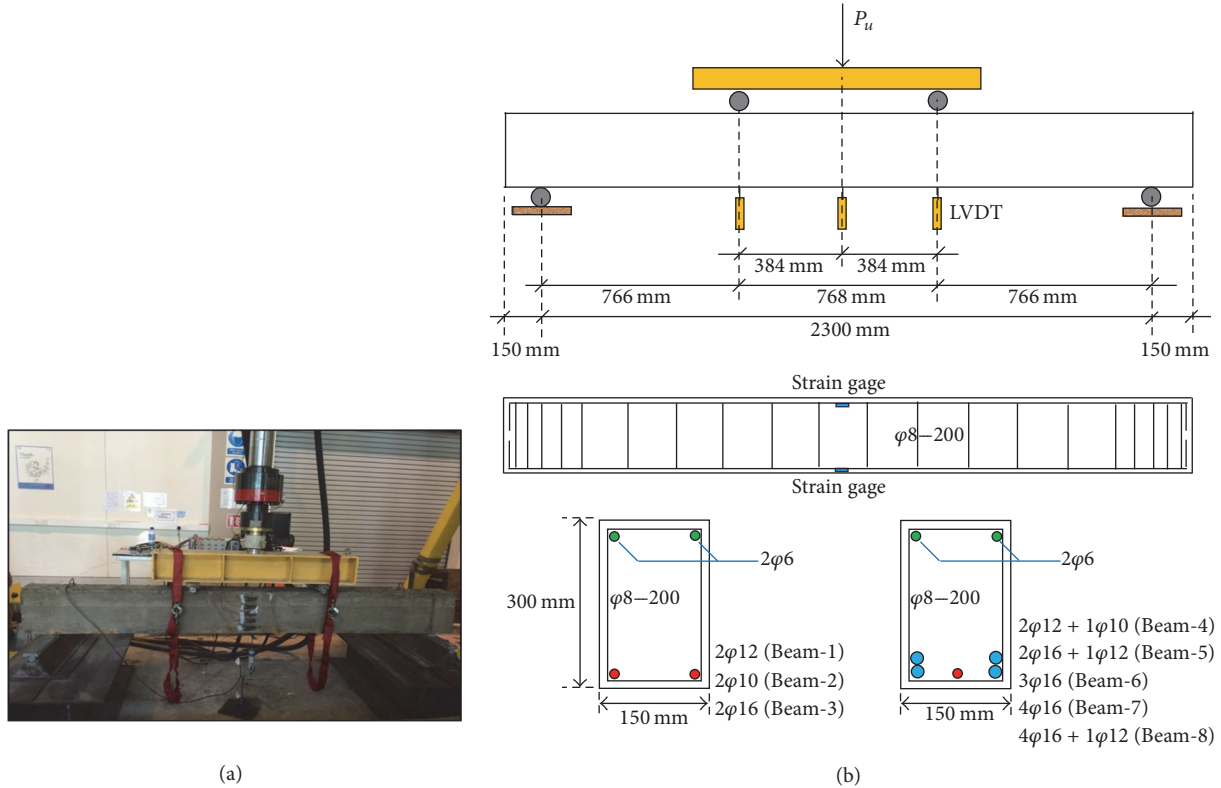


FIGURE 4: Test setup and details for R-SC-ECC beams.

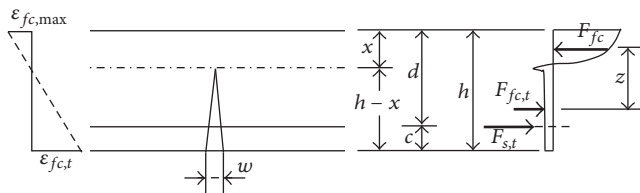


FIGURE 5: Stress-strain relationship, RILEM [15].

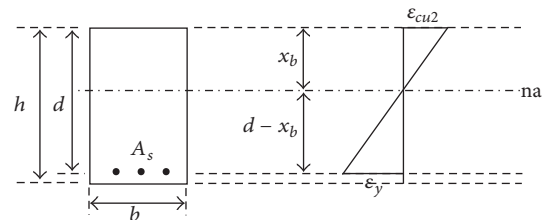


FIGURE 7: Strain diagram of R-ECC according to EC2.

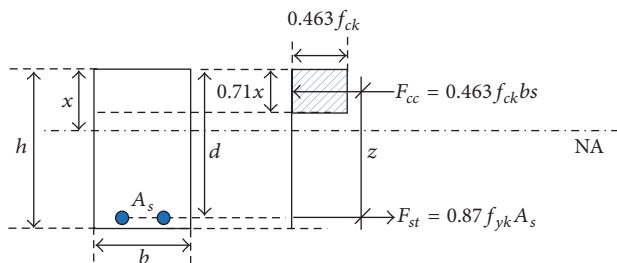


FIGURE 6: Equivalent stress block diagram for HSC, EC2 [16].

Although all beams have been designed to resist shear forces in accordance with the requirements of EC2, nevertheless, beams B7 and B8 have failed in shear. As shown in Table 6, the differences in ultimate moments between values predicted using EC2 guidelines and experimental values increase as the steel reinforcement ratio increases. This is due to the fact that EC2 models are neglecting tensile strength of SC-ECC and,

therefore, are unable to predict the accurate tensile force in tension zone.

The shear span to effective depth ratio (a_v/d) is 2.79 in this study. The failure mode of beams B7 and B8 is classified as shear failure mode and identified as a diagonal tension failure which is comparable to normal reinforced concrete failure [21]. The initial bending crack becomes inclined at early loading stage and propagates slowly to the loading point and then extends along the tension steel bar. The failure has occurred due to destruction of the bond between the tension steel and the concrete as shown in Figure 10. The tension reinforcement steel does not reach the yield values as indicated in Figure 11.

As long as the ECC in the compression zone has not reached the maximum compressive strain, the moment capacity of R-SC-ECC beam increases as steel reinforcement ratio increases. For beams B7 and B8 (with higher steel reinforcement ratio), flexural moment capacity had been

TABLE 6: Ultimate moment ratio for R-SC-ECC.

Beam number	Steel reinf. ratio, ρ	Ultimate moment, M_u (kNm)				Ultimate moment ratio		
		Exp	Analysis		FEM	EC2/Exp	R/Exp	Vec2/Exp
			EC2	RILEM	VecTor2			
		M_u^{Ex}	M_u^{EC}	M_u^R	M_u^{Vec2}	M_u^{EC}/M_u^{Ex}	M_u^R/M_u^{Ex}	M_u^{Vec2}/M_u^{Ex}
B1	0.558	33.42	22.56	50.41	45.12	0.67	1.51	1.35
B2	0.388	35.14	16.81	45.53	40.75	0.48	1.30	1.16
B3	0.993	80.78	42.48	67.5	81.2	0.53	0.84	1.01
B4	0.752	46.94	31.01	57.27	50.82	0.66	1.22	1.08
B5	1.272	91.35	51.48	76.42	93.53	0.56	0.84	1.02
B6	1.49	115.31	61.92	84.57	117.8	0.54	0.73	1.02
B7	1.986	113.17	77.42	98.49	128.23	0.68	0.87	1.13
B8	2.03	111.87	83.72	106.74	131.98	0.75	0.95	1.18
Mean (M)						0.61	1.03	1.12
Standard deviation (S)						0.09	0.26	0.11
Coefficient of variation (CoV)						0.15	0.25	0.09

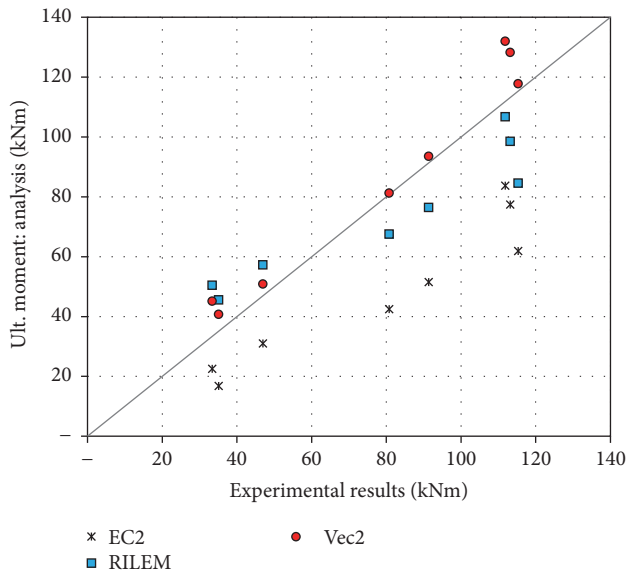


FIGURE 8: Distribution of ultimate moment ratio.

TABLE 7: Cracks width for R-SC-ECC beams at service load.

Beam number	Flexural cracks width at service load, mm
B1	0.69
B2	0.61
B3	0.57
B4	0.52
B5	0.49
B6	0.47

increased which consequently led to an increase in shear stress. However, these beams failed in shear as the shear reinforcement was kept constant throughout the beams.

The stress flow and map cracks at failure of the R-SC-ECC beams have been developed using VecTor2 FEM analysis.

The stress flow and map cracks for beams B1–B6 and B7–B8 are shown in Figures 12, 13 and 14, 15, respectively. The VecTor2 FEM analysis results are in good agreement with the experimental results. For beams B1 to B6, the stress flows and cracks occurred in constant-moment zone dominantly (Figures 12 and 13), while, for beams B7 and B8, the stress flows and cracks occurred in the shear zone as well and were more concentrated (Figures 14 and 15).

3.3. Ductility Class for R-SC-ECC. Ductility is the ability of structural component to undergo large deformations beyond yielding point without breaking [22]. In this study, ductility of R-SC-ECC beam is the area under the load-deflection curve of the beam measured by dividing the final deflection over deflection at yielding point. It is an important feature of reinforced concrete structures as the failure of the beam will be gradual and gives signs of failure. Eurocode8 has specified three ductility classes, q : low class with behavior factor less than 1.5, medium class with behavior factor between 1.5 and 4, and high class with behavior factor greater than 4. The ductility class, q , can be computed from

$$q = \frac{F_{el}}{F_y}, \quad (4)$$

where F_{el} is the maximum load and F_y is the yield load. However, as the test is a static test, therefore the ductility class q is equal to the ductility ratio μ , whereas the ductility ratio is equal to the ratio of the deflection at final failure D_u to deflection at yielding D_y . The load versus deflection curve for each R-SC-ECC beam is shown in Figure 16 and the ductility ratio for beams has been computed as shown in Table 8. For beams B1 to B6, in which the beams failed in flexure mode, at lower steel reinforcement ratio (up to 0.558), beams exhibited middle ductility and fell in the range of ductility class medium with ductility ratio higher than 1.5. Nevertheless, the beams that have higher steel reinforcement ratio (larger than 0.752 and less than 1.986) showed ductility ratio greater than 4, which classifies them as ductility class high.

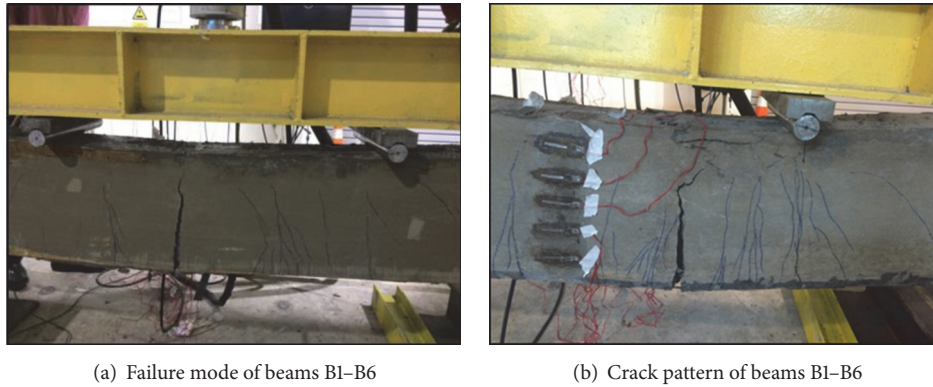


FIGURE 9: Typical flexural failure modes for beams B1 to B6.

TABLE 8: Ductility ratio for R-SC-ECC beams (experimental results).

Beam	Deflection at yield, D_y (mm)	Deflection at failure, D_u (mm)	Ductility ratio, D_u/D_y
B1	8.76	18.41	2.1
B2	5.2	17.84	3.43
B3	7.16	32.08	4.48
B4	6.13	26.45	4.31
B5	8.95	41.41	4.62
B6	8.25	40	4.84
B7	10.04	18.33	1.83
B8	7.45	16.84	2.26



FIGURE 10: Typical shear failure mode of beams B7 and B8.

Eurocode8 suggests that, in regions with medium to high seismic activities, beams with ductility class medium to high can be used. This is necessary to ensure that the beams have the ability to absorb energy.

Although beams B7 and B8 failed in shear, nevertheless, these beams exhibited good ductility ratios, which are 1.83 and 2.26, respectively. It is worth noting that B7 and B8 are categorized as ductility class medium. This is due to ECC ductility superiority compared to normal concrete, in which tailoring of ECC (mechanical interactions between the fibers, matrix, and interface) can provide good performance even if the cracks' width is wider (Li [23]). In this study, it was found

that the optimum ductility has been achieved by beam B6 with steel reinforcement ratio (ρ) of 1.49.

The behavior of ECC structural elements has been investigated and elaborated [6, 24–27]. In this study, superiority of ECC can be proved compared to normal concrete such as behavior of ECC in direct tensile test and compression stress-strain test as shown in Figures 17 and 18, respectively.

According to this investigation, ECC has high tensile strength of 4.87 MPa (2.44-fold higher compared to normal strength concrete) and its strain capacity is larger by 545% compared to normal strength concrete (NSC). ECC exhibits strain hardening and its descending curve is quite smooth (softening) after postpeak condition, whereas compression stress-strain curve of ECC exhibits an ascending pattern at prepeak condition with smaller tangential angle compared to VecTor2 prepeak models due to lower elastic modulus of 22 GPa for ECC. Based on ACI provision (2008), ECC was categorized as high strength concrete (HSC), in which ECC has compressive strength of 86.5 MPa. Unlike ECC, elastic modulus of HSC is usually greater than 24 GPa and exhibits sudden and explosive crushing. Nevertheless, due to the strong bonding between fibers and cementitious matrix, the peak condition of ECC is always attained on slow pace and the ECC crushing is always marked by bulging behavior. The ECC behavior is specific and rather different compared to available VecTor2 prepeak models. Basically, the compression stress-strain curve of VecTor2 prepeak models is based on

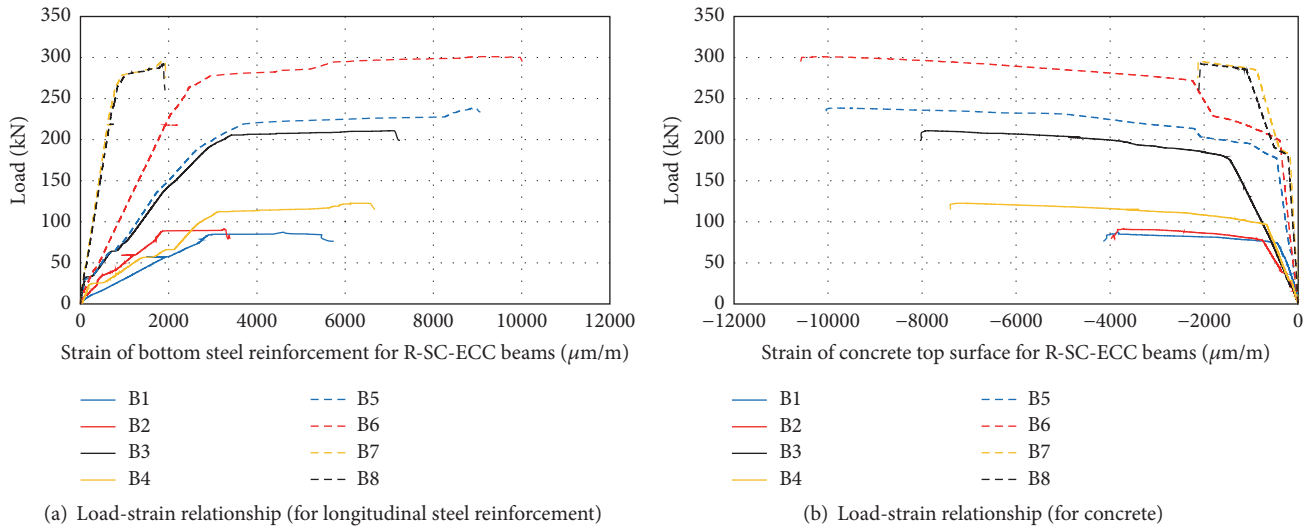


FIGURE 11: Strain of steel bars and concrete.

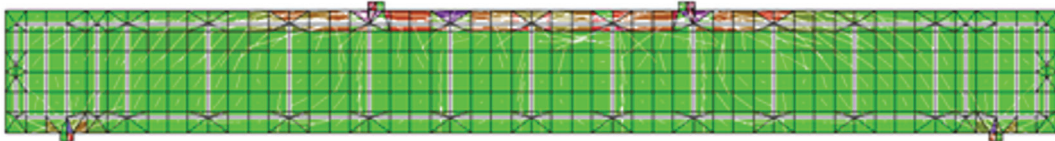


FIGURE 12: Typical stress flow at flexural failure modes of beams B1–B6 (VecTor2 analysis).

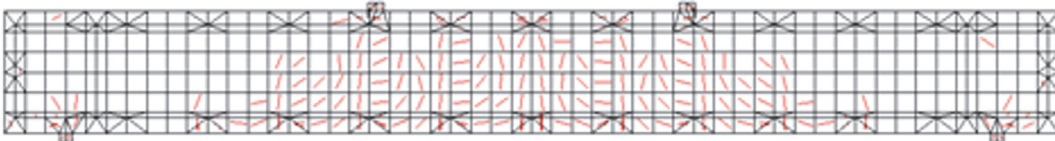


FIGURE 13: Typical map cracks in flexure region of beams B1–B6 (VecTor2 analysis).

elastic modulus of larger than 24 GPa, even though it utilizes Popovic-HSC models. In this study, all available prepeak models of VecTor2 have been investigated and ECC properties (experimental results) have been utilized to simulate the most appropriate model. Therefore, load-deformation curves of R-SC-ECC beams exhibit smaller tangential angle compared to curves obtained from VecTor2 analysis as shown in Figures 20 and 21.

As indicated in the previous sections, RILEM and EC2 models are not suitable for predicting ultimate moments for R-SC-ECC beams. However, VecTor2 FEM analysis results showed good agreement in predicting the ultimate moments capacities and cracks patterns. To evaluate further the suitability of the VecTor2 FEM analysis, load versus deflection for all beams has been created as shown in Figure 19 and the predicted ultimate loads have been compared with the experimental values as shown in Table 9. The predicted ultimate loads using VecTor2 FEM analysis have shown good agreement with the experimental ultimate loads values.

Comparisons of experimental results with VecTor2 analysis at load-deflection relationships for R-SC-ECC beams

are shown in Figures 20 and 21. For prepeak condition, it has been noticed that Popovic-high strength concrete (HSC) model yields larger tangential angle compared to experimental results. And after postpeak condition, the curve of VecTor2 model shows some fluctuations. Basically, to obtain appropriate models in VecTor2, ECC actual properties have been utilized. In addition, VecTor2 models have been selected on trial-and-error basis, in which the following postpeak models have been considered: Popovic/Mander (as compression postpeak model), Vecchio 1992 (as compression softening model), Modified Bentz 2003 (as tension stiffening model), Nonlinear Yamamoto (as tension softening model), Selby (as confined strength model), Variable-Montoya with limit (as dilatation model), and Mohr-Coulomb Stress (as cracking criterion model).

The behavior of the postpeak models becomes comparable to the experimental results after the models reach the maximum stage up to final failure. The predicted ultimate loads and final deflections by VecTor2 are in good agreement with the experimental results as shown in Table 9 and Figures 20 and 21.

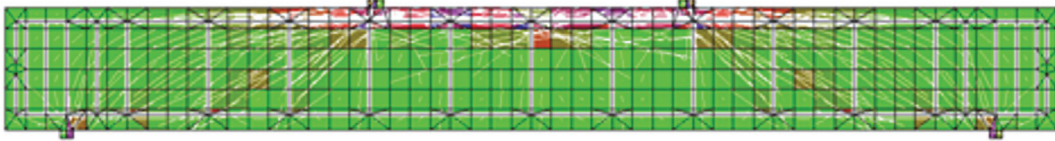


FIGURE 14: Typical stress flow at shear failure modes of beams B7-B8 (VecTor2 analysis).

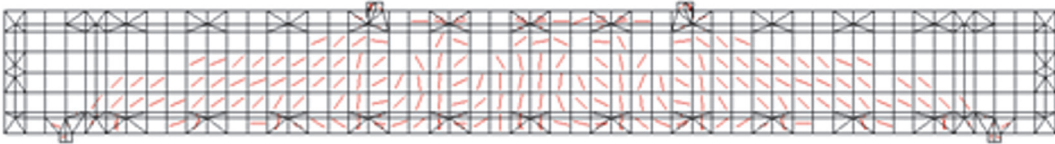


FIGURE 15: Typical map cracks in shear region of beams B7-B8 (VecTor2 analysis).

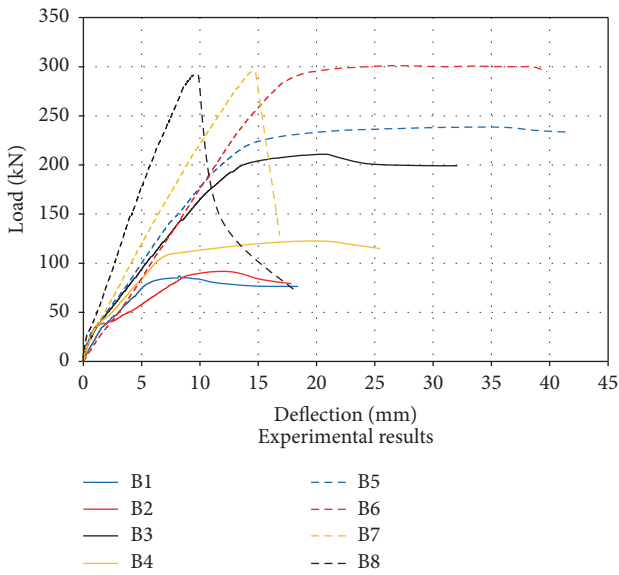


FIGURE 16: Load-deflection relationships for R-SC-ECC beams.

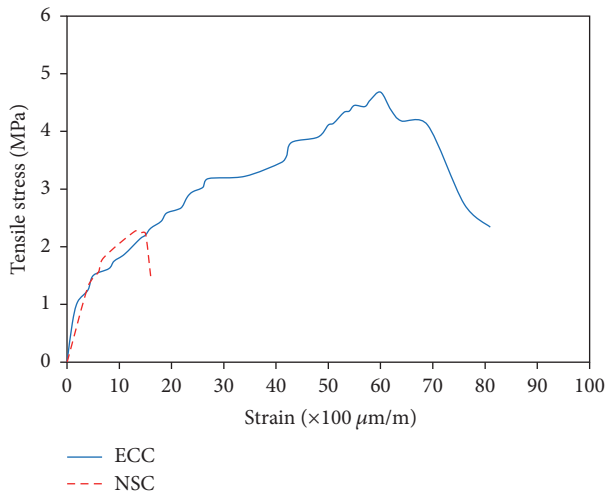


FIGURE 17: Direct tensile strength: ECC and NSC.

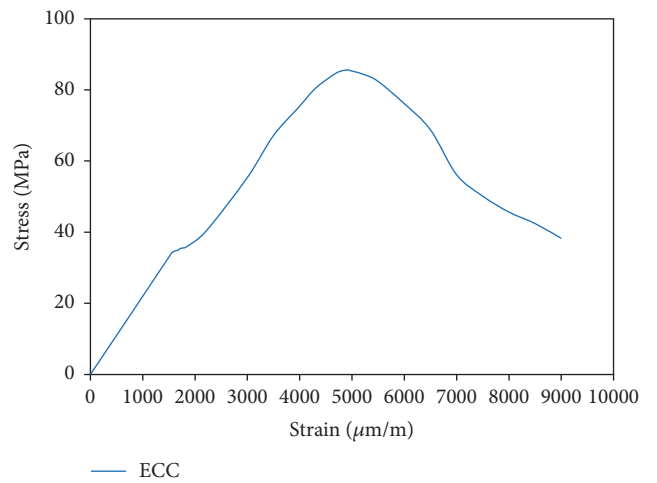


FIGURE 18: Compression stress-strain curve: ECC.

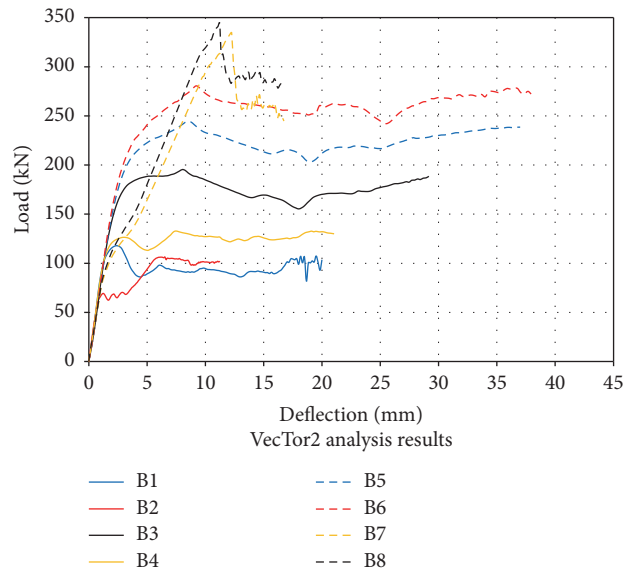
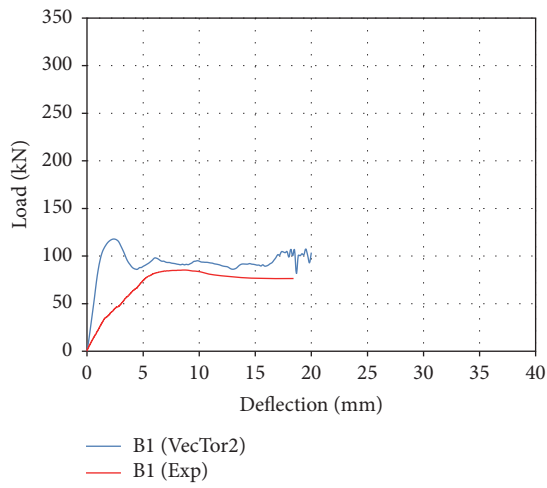
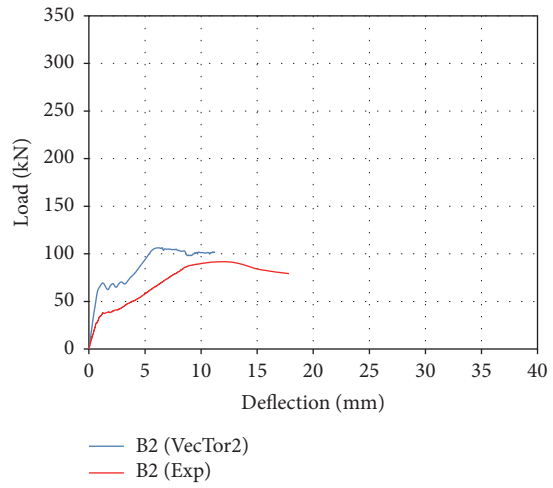


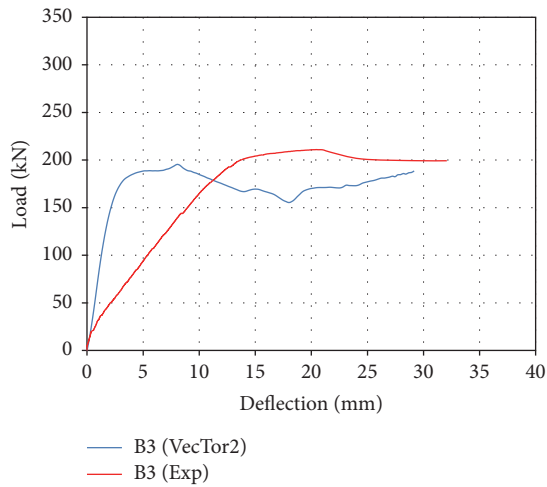
FIGURE 19: Load-deformation relationships for R-SC-ECC beams.



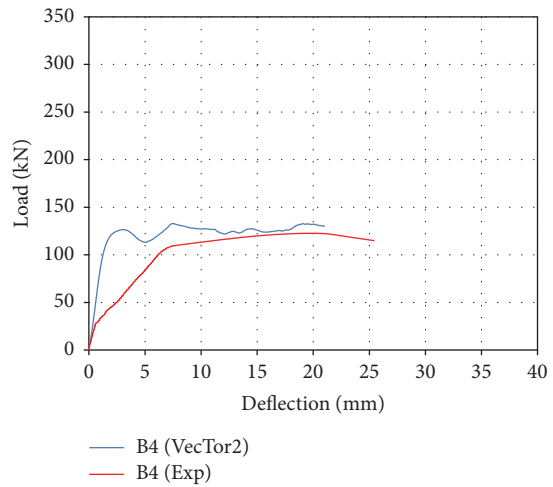
(a) Beam B1



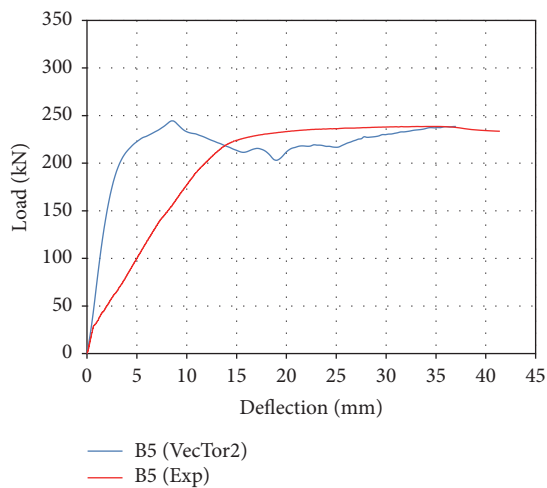
(b) Beam B2



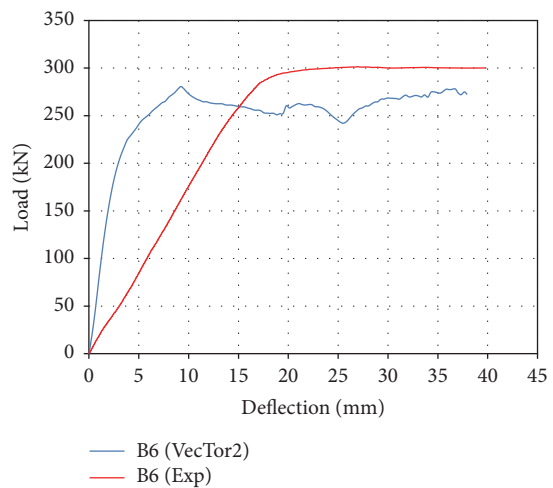
(c) Beam B3



(d) Beam B4



(e) Beam B5



(f) Beam B6

FIGURE 20: Load-deflection relationships for R-SC-ECC beams.

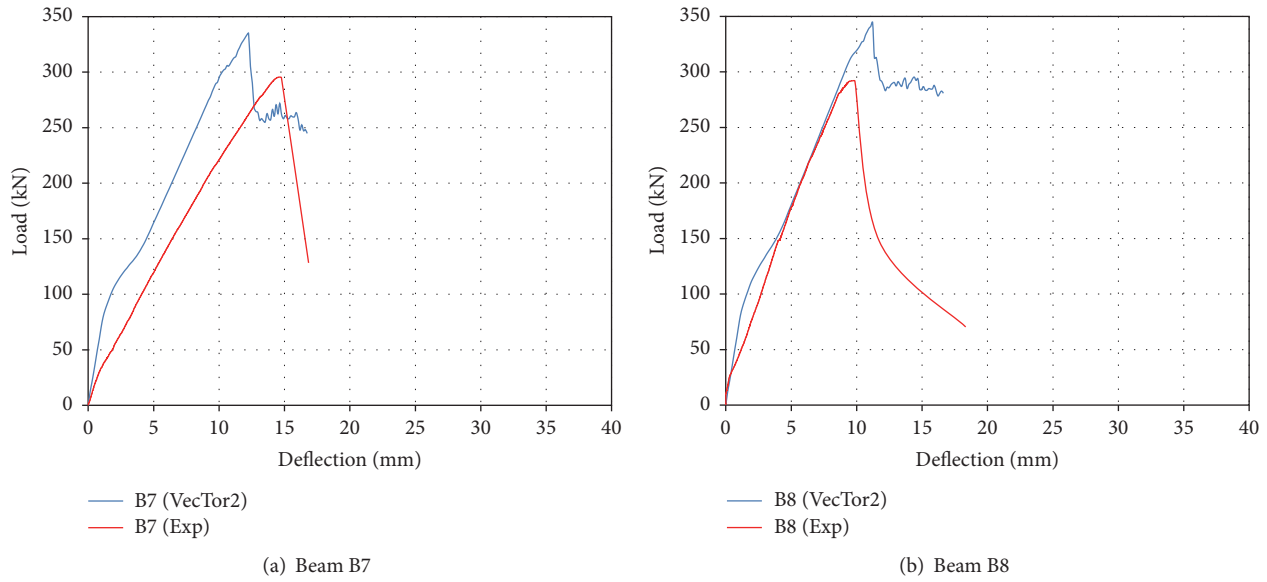


FIGURE 21: Load-deflection relationships for R-SC-ECC beams.

TABLE 9: Ultimate load deflection: VecTor2 and experimental results.

Beam number	Steel reinf. ratio, ρ	Load at ultimate stage (kN)		Deflection at rupture (mm)		Ratio	
		Exp (P_{Ex})	VecTor2 (P_{Vec2})	Exp (D_{Ex})	VecTor2 (D_{Vec2})	P_{Vec2}/P_{Ex}	D_{Vec2}/D_{Ex}
B1	0.558	87.27	117.8	18.41	19.99	1.35	1.09
B2	0.388	91.76	106.4	17.84	11.24	1.16	0.63
B3	0.993	210.92	195.4	32.08	29.17	0.93	0.91
B4	0.752	122.55	132.7	26.45	21.04	1.08	0.80
B5	1.272	238.5	244.2	41.41	36.99	1.02	0.89
B6	1.49	301.08	280.5	40.00	37.94	0.93	0.95
B7	1.986	295.48	334.8	18.33	16.74	1.13	0.91
B8	2.03	292.08	344.6	16.84	16.60	1.18	0.91
Mean						1.10	0.90

Therefore, to obtain reasonable structural behavior of R-SC-ECC, VecTor2 is an appropriate package as it contains concrete models, reinforcement models, and bond models. The concrete models include compression prepeak and post-peak response, compression softening, tension stiffening and softening, tension splitting, confined strength, and crack, whereas reinforcement models include hysteretic response, dowel action, and buckling.

4. Conclusions

The following conclusions can be drawn from this study:

- (1) The flexural and shear failure modes for R-SC-ECC beams are comparable to failure modes of normal reinforced concrete beams.
- (2) Predicting the ultimate moments of R-SC-ECC beams using EC2 models yields very conservative results

due to neglecting tensile strength of SC-ECC in the computing of ultimate strengths.

- (3) RILEM models are suitable for predicting ultimate strength of R-SC-ECC beams with small reinforcement ratios. However, as reinforcement ratio increases, RILEM models will yield results that are more conservative.
- (4) Finite element models using VecTor2 package have successfully predicted the structural behavior of R-SC-ECC beams including failure modes, ultimate moments, failure loads, and deflections.
- (5) R-SC-ECC beams exhibit ductility class medium to high. Therefore, ECC is very suitable for regions with seismic activities as ECC has the ability to absorb energy.

Competing Interests

The authors declare that they have no competing interests.

References

- [1] S. H. Said and H. Abdul Razak, "Structural behavior of RC engineered cementitious composite (ECC) exterior beam-column joints under reversed cyclic loading," *Construction and Building Materials*, vol. 107, pp. 226–234, 2016.
- [2] S. H. Said and H. A. Razak, "The effect of synthetic polyethylene fiber on the strain hardening behavior of engineered cementitious composite (ECC)," *Materials and Design*, vol. 86, pp. 447–457, 2015.
- [3] C.-C. Hung, W.-M. Yen, and K.-H. Yu, "Vulnerability and improvement of reinforced ECC flexural members under displacement reversals: experimental investigation and computational analysis," *Construction and Building Materials*, vol. 107, pp. 287–298, 2016.
- [4] S. H. Said, H. A. Razak, and I. Othman, "Flexural behavior of engineered cementitious composite (ECC) slabs with polyvinyl alcohol fibers," *Construction and Building Materials*, vol. 75, pp. 176–188, 2015.
- [5] Q. Zhang and V. C. Li, "Development of durable spray-applied fire-resistive Engineered Cementitious Composites (SFR-ECC)," *Cement and Concrete Composites*, vol. 60, pp. 10–16, 2015.
- [6] B. S. Mohammed, M. Aswin, W. H. Beatty, and M. Hafiz, "Longitudinal shear resistance of PVA-ECC composite slabs," *Structures*, vol. 5, pp. 247–257, 2016.
- [7] C.-C. Hung and Y.-S. Chen, "Innovative ECC jacketing for retrofitting shear-deficient RC members," *Construction and Building Materials*, vol. 111, pp. 408–418, 2016.
- [8] Z. Pan, C. Wu, J. Liu, W. Wang, and J. Liu, "Study on mechanical properties of cost-effective polyvinyl alcohol engineered cementitious composites (PVA-ECC)," *Construction and Building Materials*, vol. 78, pp. 397–404, 2015.
- [9] Z. Zhang, S. Qian, and H. Ma, "Investigating mechanical properties and self-healing behavior of micro-cracked ECC with different volume of fly ash," *Construction and Building Materials*, vol. 52, pp. 17–23, 2014.
- [10] J. Yu, J. Lin, Z. Zhang, and V. C. Li, "Mechanical performance of ECC with high-volume fly ash after sub-elevated temperatures," *Construction and Building Materials*, vol. 99, pp. 82–89, 2015.
- [11] A. R. Sakulich and V. C. Li, "Nanoscale characterization of engineered cementitious composites (ECC)," *Cement and Concrete Research*, vol. 41, no. 2, pp. 169–175, 2011.
- [12] K. Amini, I. Mehdipour, S. D. Hwang, and M. Shekarchi, "Effect of binder composition on time-dependent stability and robustness characteristics of self-consolidating mortar subjected to prolonged agitation," *Construction and Building Materials*, vol. 112, pp. 654–665, 2016.
- [13] L. Señas, C. Priano, and S. Marfil, "Influence of recycled aggregates on properties of self-consolidating concretes," *Construction and Building Materials*, vol. 113, pp. 498–505, 2016.
- [14] M. M. Kamal, M. A. Safan, Z. A. Etman, and B. M. Kasem, "Mechanical properties of self-compacted fiber concrete mixes," *HBRC Journal*, vol. 10, no. 1, pp. 25–34, 2014.
- [15] L. Vandewalle, "Recommendations of RILEM TC 162-TDF: Test and design methods for steel fibre reinforced concrete," *Materials and Structures/Materiaux et Constructions*, vol. 33, no. 225, pp. 3–5, 2000.
- [16] Eurocode2, Design of concrete structures, Part 1-1: General rules and rules for buildings, 2004.
- [17] F. J. Vecchio and P. S. Wong, *VecTor2 & Formworks User's Manual*, University of Toronto, Toronto, Canada, 2002.
- [18] F. J. Vecchio and M. P. Collins, "The modified compression field theory for reinforced concrete elements subject to shear," *ACI Journal*, vol. 83, no. 2, pp. 219–231, 1986.
- [19] F. J. Vecchio, "Disturbed stress field model for reinforced concrete: formulation," *ASCE Journal of Structural Engineering*, vol. 126, no. 9, pp. 1070–1077, 2000.
- [20] B. S. Mohammed, W. L. Foo, and M. Abdullahi, "Flexural strength of palm oil clinker concrete beams," *Materials and Design*, vol. 53, pp. 325–331, 2014.
- [21] B. S. Mohammed, W. L. Foo, K. M. A. Hossain, and M. Abdullahi, "Shear strength of palm oil clinker concrete beams," *Materials and Design*, vol. 46, pp. 270–276, 2013.
- [22] Eurocode8, *Design of Structures for Earthquake Resistance, Part 1: General Rules, Seismic Actions and Rules for Buildings*, 2004.
- [23] V. C. Li, "Hygral behavior of Engineered Cementitious Composite (ECC)," *International Journal for Restoration of Buildings and Monuments*, vol. 9, pp. 513–534, 2003.
- [24] M. Aswin, B. S. Mohammed, M. S. Liew, and Z. I. Syed, "Shear failure of RC dapped-end beams," *Advances in Materials Science and Engineering*, vol. 2015, Article ID 309135, 11 pages, 2015.
- [25] H. M. E.-D. Afefy and M. H. Mahmoud, "Structural performance of RC slabs provided by pre-cast ECC strips in tension cover zone," *Construction and Building Materials*, vol. 65, pp. 103–113, 2014.
- [26] M. Maalej, S. T. Quek, S. F. U. Ahmed, J. Zhang, V. W. J. Lin, and K. S. Leong, "Review of potential structural applications of hybrid fiber Engineered Cementitious Composites," *Construction and Building Materials*, vol. 36, pp. 216–227, 2012.
- [27] S. Qudah and M. Maalej, "Application of Engineered Cementitious Composites (ECC) in interior beam-column connections for enhanced seismic resistance," *Engineering Structures*, vol. 69, pp. 235–245, 2014.

Research Article

Effect of Water-Cement Ratio on Pore Structure and Strength of Foam Concrete

Zhongwei Liu,^{1,2} Kang Zhao,¹ Chi Hu,² and Yufei Tang¹

¹Department of Materials Science and Engineering, Xi'an University of Technology, Xi'an 710048, China

²Sichuan College of Architectural Technology, Deyang 618000, China

Correspondence should be addressed to Kang Zhao; kzhao@xaut.edu.cn

Received 4 August 2016; Revised 18 September 2016; Accepted 22 September 2016

Academic Editor: Sumin Kim

Copyright © 2016 Zhongwei Liu et al. This is an open access article distributed under the Creative Commons Attribution License, which permits unrestricted use, distribution, and reproduction in any medium, provided the original work is properly cited.

Foam concrete with different dry densities (400, 500, 600, 700, and 800 kg/m³) was prepared from ordinary Portland cement (P.O.42.5R) and vegetable protein foaming agent by adjusting the water-cement ratio through the physical foaming method. The performance of the cement paste adopted, as well as the structure and distribution of air pores, was characterized by a rheometer, scanning electron microscope, vacuum water saturation instrument, and image analysis software. Effects of the water-cement ratio on the relative viscosity of the cement paste, as well as pore structure and strength of the hardened foam concrete, were discussed. Results showed that water-cement ratio can influence the size, distribution, and connectivity of pores in foam concrete. The compressive strength of the foam concrete showed an inverted V-shaped variation law with the increase in water-cement ratio.

1. Introduction

Foam concrete has been widely used in roofing materials, wall materials, sound absorbing materials, underground backfill, and other applications because of the material's characteristic light weight, good thermal insulation, excellent seismic behavior, and low noise and pollution [1]. At present, related studies mainly focus on the effect of admixture on the performance of foam concrete [2–5], as well as the correlation of pore structure and absolute dry density of foam concrete with the material's strength, thermal conductivity, and sound absorption. w/c ratio is an important factor that influences foam concrete performance [6–11]. Existing research on the effect of w/c ratio on the pore structure and performance of foam concrete mainly emphasizes high-porosity foam concrete (porosity > 85%) [12–14]. By contrast, few studies have discussed the influences of w/c ratio on the pore structure and performance of ordinary foam concrete (porosity < 85%) [15]. Jiang et al. [13] investigated the effect of w/c ratio on the pore structure of high-porosity foam concrete. The scholars found that when w/c < 0.8, the pores were small, irregularly shaped, and highly connected. When w/c > 0.8, the pores were round and expansive, accompanied with

a widened pore diameter distribution range. Krämer et al. [16, 17] explored the formation of pore shells in foam concrete and the pore shell enhancement mechanism of volcanic ash. She found that adding volcanic ash when preparing foam concrete can enhance foam concrete strength. Ley et al. [18] studied the physical and chemical properties of pore shells in cement paste and found that air entraining agents could influence the pore shells to a certain extent. Chen et al. [3] prepared foam concrete using circulating fluidized bed fly ash. The group found that bubbles in cement paste of high consistency are easily broken during stirring and the density of the corresponding concrete increases during such process. Paste consistency could be adjusted by adding a water reducer. Meanwhile, Hilal et al. [19, 20] analyzed the coupling relationship between bubbles under natural and stress states during foam concrete coagulation and pores in hardened foam concrete. The scholars found that the bubbles combined during the stirring and coagulation of foam concrete, thereby expanding the pore diameter distribution of the foam concrete and reducing the foam concrete's strength. Yang and Lee [21] studied the influences of water-binder ratio and fly ash content on foam concrete performance. The scholars reported that, with the increase in water-binder ratio, the amount of

TABLE 1: The physical properties of cement.

Material	Blaine fineness (m ² /kg)	Initial setting time (min)	Final setting time (min)	Soundness	3 d compressive strength (MPa)	28 d compressive strength (MPa)
P.O42.5R	343	91	210	qualified	28.7	48.9

TABLE 2: The main chemical composition of cement (wt%).

Compositions (%)	SiO ₂	Al ₂ O ₃	Fe ₂ O ₃	CaO	MgO	SO ₃	Na ₂ O	K ₂ O	Loss of ignition
Content	21.6	4.9	2.50	63.4	1.80	2.14	0.14	0.37	3.15

microcapillaries decreased, whereas those of macrocapillaries and artificial pores increased. Such occurrence resulted in the higher porosity and lower strength of the resultant foam concrete. Wei et al. [22] investigated the coagulation and hardening behaviors of foam concrete and discovered that shortening the coagulation time by accelerating hydration can effectively enhance foam concrete stability.

Although these works have analyzed many factors influencing the pore structure of ordinary foam concrete and the effect of w/c ratio on high-porosity foam concrete, none explored the effect of w/c ratio on the pore structure of ordinary foam concrete. In this paper, we discussed the effects of w/c ratio on cement paste liquidity and pore structure and foam concrete strength. Results could provide reference for the preparation of lightweight, high-strength foam concrete.

2. Experimental

2.1. Materials. The cement used was P.O.42.5R cement produced by the Sichuan Deyang Lisen Cement Co., Ltd. The physical properties and chemical composition of the cement are shown in Tables 1 and 2, respectively. Meanwhile, the foaming agent employed was vegetable protein foaming agent manufactured by Sichuan Xinhan Corrosion Protection Engineering Co., Ltd.

2.2. Preparation. According to Table 3, cement and water were poured into a 15 dm³ horizontal type mixer (GH-15, Beijing Guanggui Jingyan Foamed Concrete Science & Technology Co., Ltd.) and mixed at a rate of 40 rpm for 120 s at 25°C to generate paste. Meanwhile, the foaming agent was diluted with water at the proportion 1:15. Next, protein foam produced by a foam generator (ZK-FP-20, Beijing Zhongke Zhucheng Building Materials Co., Ltd.) was injected into a foam concrete mixer and stirred for 120 s. Next, the foam concrete was poured into a mold and maintained in static for 24 h. After demolding, the foam concrete was subjected to standard maintenance (20 ± 2°C; RH > 95%) for 28 days.

2.3. Test Method. Relative viscosity was tested using a rotary viscometer (NXS-IIA, Chengdu Instrument Factory, China). The microstructures of the specimens were determined by scanning electron microscopy (SEM; Hitachi JSM-7500F). Next, black-white binarization processing of images was conducted. Finally, pore structure parameters (e.g., pore diameter

and distribution) were acquired directly using the Image-Pro Plus 6.0 image analysis software (launched “Count/siz” under the Measure menu in Windows).

Volume density and compressive strength tests of the foam concrete complied with the Chinese *Foamed Concrete* standard (JG/T 266-2011). The compressive strength of the specimens was measured by a fully automatic, constant stress testing machine (JYE-300A, Beijing Jiwei Testing Instrument Co., Ltd., China) under a loading rate of 200 N/s. The true density (ρ_1) of the specimens was tested in accordance with the *Cement Density Measurement Method* standard (GB/T 208-2014). The absolute dry volume density of the specimens was denoted by ρ_2 . Then, the porosity of specimens was determined using the following formula:

$$P = \frac{\rho_1 - \rho_2}{\rho_1} \times 100\%, \quad (1)$$

where P is the porosity of the specimens (%), ρ_1 is the true density of the specimens (kg/m³), and ρ_2 is the volume density of the specimens (kg/m³).

The open porosity of the foam concrete was assessed. The testing principle involved the pressing of water into the open pores inside the foam concrete by exploiting negative pressure. The open pores were filled with water, and the absorbed water volume corresponds to the volume of the open pores. An intelligent concrete vacuum water saturation instrument (SW-6, Beijing Shengshi Weiye Science & Technology Co., Ltd.) was used in the test. After the specimens were placed, the air cock of the vacuum chamber was switched on until the vacuum reached lower than -0.08 MPa. This negative pressure was then maintained for 3 h, after which water was injected. Next, we applied vacuum for another 2 h and then allowed the vacuum chamber to recover to normal pressure. The foam concrete was removed and weighed 22 h later. Open porosity (P_O) and closed porosity (P_C) were calculated using (1), (2), and (3).

P_O of the specimens was calculated as

$$P_O = \frac{m_2 - m_1}{V} \times \frac{1}{\rho_W} \times 100\%, \quad (2)$$

where m_1 is the dry material mass (kg), m_2 is the material mass under the water-saturated state (kg), ρ_W is the water density (kg/m³), and V is the natural volume of the material.

TABLE 3: Mix proportions of raw materials.

Mixes designation	Design density (kg/m ³)	Cement (g)	Water (g)	w/c	Foam (mL)
400-0.40	400	2909	1164	0.40	5883
400-0.45	400	2909	1309	0.45	5737
400-0.50	400	2909	1455	0.50	5592
400-0.55	400	2909	1600	0.55	5446
400-0.60	400	2909	1745	0.60	5301
500-0.40	500	3636	1454	0.40	5353
500-0.45	500	3636	1636	0.45	5171
500-0.50	500	3636	1818	0.50	4990
500-0.55	500	3636	2000	0.55	4808
500-0.60	500	3636	2182	0.60	4626
600-0.40	600	4364	1746	0.40	4824
600-0.45	600	4364	1964	0.45	4606
600-0.50	600	4364	2182	0.50	4387
600-0.55	600	4364	2400	0.55	4169
600-0.60	600	4.364	2618	0.60	3951
700-0.40	700	5091	2036	0.40	4294
700-0.45	700	5091	2291	0.45	4040
700-0.50	700	5091	2546	0.50	3785
700-0.55	700	5091	2800	0.55	3531
700-0.60	700	5091	3055	0.60	3276
800-0.40	800	5818	2327	0.40	3765
800-0.45	800	5818	2618	0.45	3474
800-0.50	800	5818	2909	0.50	3183
800-0.55	800	5818	3200	0.55	2892
800-0.60	800	5818	3491	0.60	2601

Meanwhile, P_C of the specimens were determined as follows:

$$P_C = P - P_O. \quad (3)$$

3. Results and Discussion

3.1. Effect of w/c Ratio on the Rheological Properties of Cement Paste. Foam concrete density is mainly adjusted through foam dosage; hence, cement pastes with same w/c ratios exhibit consistent rheological properties. In this experiment, the rheological properties of the cement pastes of different w/c ratios (0.40, 0.45, 0.50, 0.55, and 0.60) were evaluated and used to interpret the effect of the bubble maintenance of the cement pastes on the pore structure of hardened foam concrete. Cement paste is a kind of non-Newtonian fluid, and its relative viscosity equals the shear stress/shear rate:

$$\eta = \frac{\tau}{D_S}, \quad (4)$$

where η is the relative viscosity, τ is the shear stress, and D_S is the shear rate.

The effect of w/c ratio on the rheological properties of cement paste is shown in Figure 1. We calculated from (4) that the relative viscosities of cement pastes with 0.40, 0.45, 0.50, 0.55, and 0.60 w/c ratios were 0.4075, 0.2737, 0.0594, 0.0255, and 0.0159 Pa-s, indicating that the relative viscosity

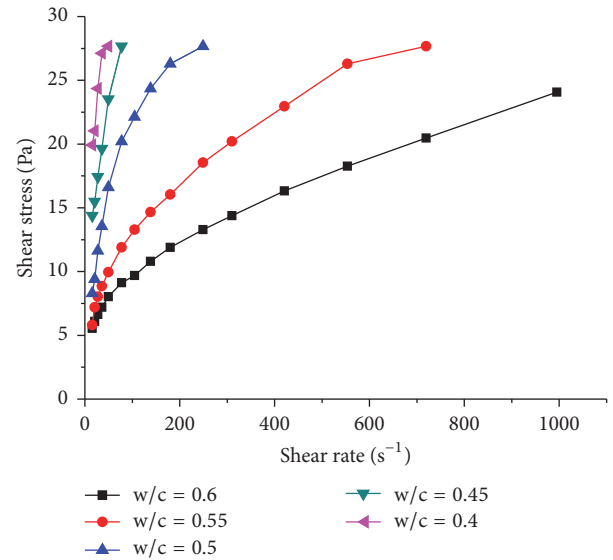


FIGURE 1: Effect of w/c on the rheological properties of cement paste.

of cement paste decreases gradually with the increase of w/c ratio. This result is achieved because the water film on the cement particle surface thickens with the increase in w/c ratio, thus reducing the relative viscosity of cement paste [23].

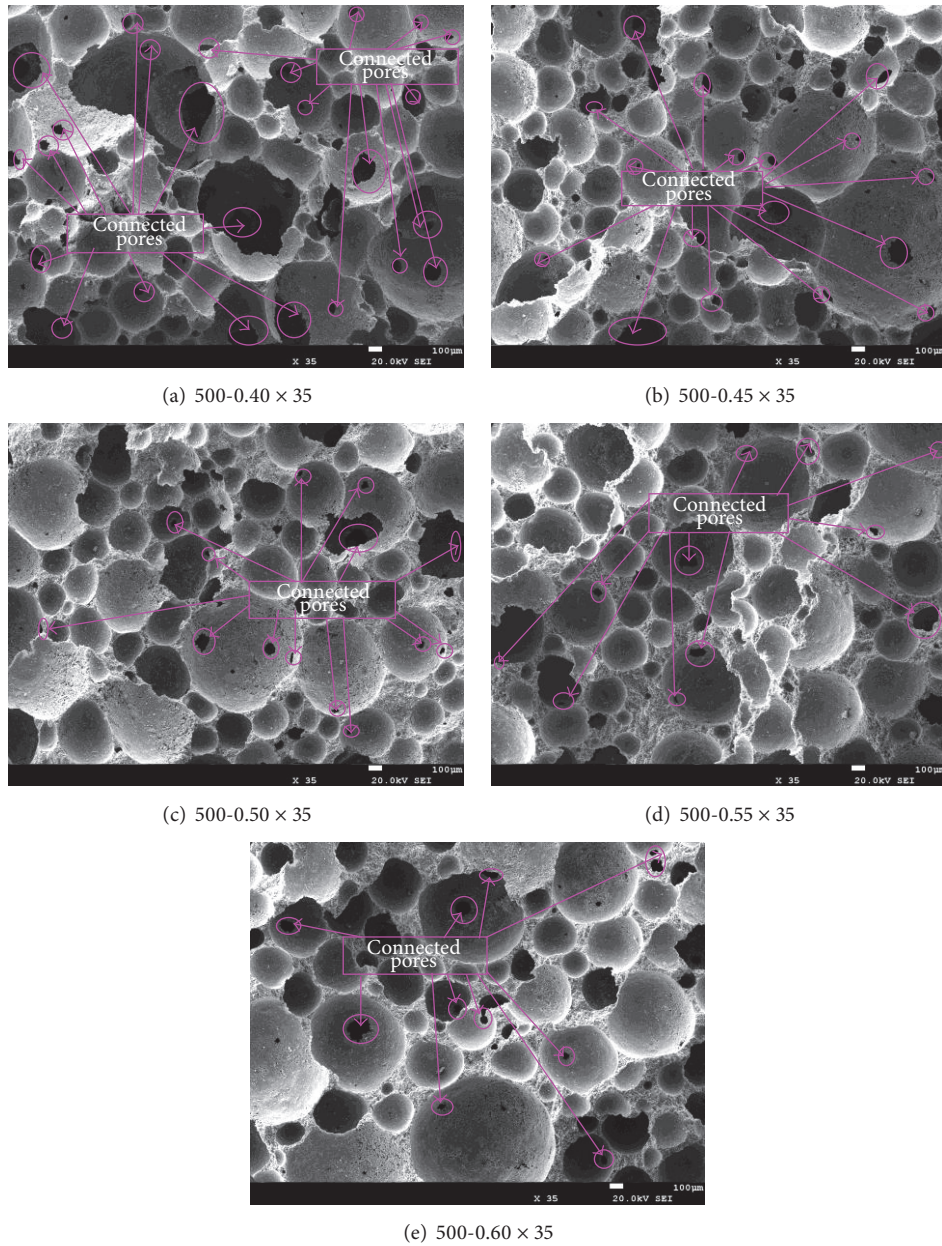


FIGURE 2: SEM images of the 500 kg/m³ foam concrete of different w/c ratios.

3.2. Effect of w/c Ratio on the Foam Concrete Pore Structure.

Figures 2 and 3 show the SEM images of 500 and 800 kg/m³ foam concrete samples of different w/c ratios. (1) The foam concrete with smaller w/c ratio exhibited a greater number of connected pores. This result may be due to the notion that the smaller w/c ratio would bring a higher proportion of small pores in foam concrete and a larger surface area, finally resulting in thinner pore walls and more connected pores [24]. (2) The foam concrete with smaller dry density displayed more connected pores because higher bubble proportions would involve a smaller proportion of the paste and weaker resistance against bubble connection [25].

The numerical values of the pore characteristics of the specimens calculated by the Image-Pro Plus 6.0 software in

accordance with Figures 2 and 3 are listed in Table 4. With the increase in w/c ratio, the average pore diameter of the foam concrete increased gradually and the pores became more rounded (Table 4). This finding may be due to the gradual decrease in relative viscosity of cement paste as the w/c ratio increased, thus weakening the bubble-maintaining capacity of the paste. Small bubbles in the paste were easily combined and readily expanded during the stirring process [14]. Meanwhile, the frictional force in the paste reduced, rendering the bubbles increasingly round. Furthermore, the higher dry density of the foam concrete caused decreased the average pore diameter and rendered the pores rounder. A higher paste proportion would generate a smaller bubble proportion, making bubble combination and expansion difficult.

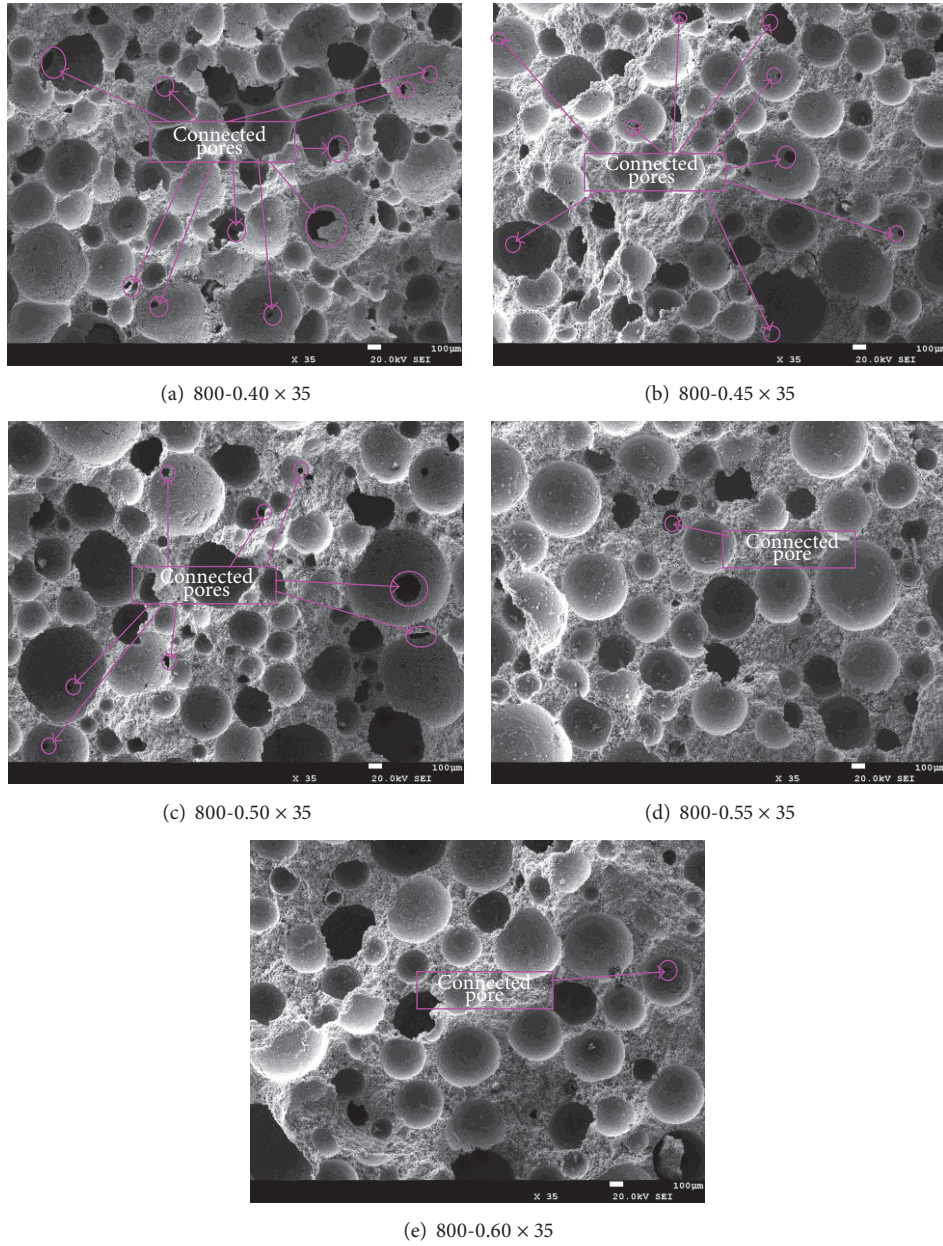


FIGURE 3: SEM images of the 800 kg/m³ foam concrete of different w/c ratios.

The effect of w/c ratio on the pore diameter distribution of the 500 kg/m³ foam concrete is shown in Figure 4(a). Small pores (<100 µm) in the 500-0.40, 500-0.45, 500-0.50, 500-0.55, and 500-0.60 samples accounted for 23.97%, 21.82%, 20.51%, 16.0%, and 11.91%, respectively, of the volume. By contrast, the large pores (>400 µm) occupied 10.74%, 10.00%, 7.69%, 12.0%, and 15.48%, respectively. The pore proportions (100~400 µm), which determined the foam concrete strengths, were 65.29%, 68.18%, 71.79%, 72.00%, and 72.62%, respectively. Results showed that most of the pore diameters in the foam concrete samples ranged between 0 and 400 µm. With the increase in w/c ratio, the proportion of small pores (<100 µm) lowered. Meanwhile, the proportion of the pores

determining foam concrete strength (100–400 µm) changed slightly, whereas the proportion of the large pores (>400 µm) was extremely small.

The effect of w/c ratio on the pore diameter distribution of 800 kg/m³ foam concrete is shown in Figure 4(b). Small pores (<100 µm) in the 800-0.40, 800-0.45, 800-0.50, 800-0.55, and 800-0.60 samples accounted for 23.81%, 19.15%, 17.86%, 11.76%, and 8.45%, respectively, of the volume of the concrete. By contrast, the large pores (>400 µm) occupied 7.77%, 9.64%, 3.57%, 10.59%, and 14.08%, respectively. The proportions of pores (100–400 µm) that determined the foam concrete strength were 68.42%, 71.21%, 78.57%, 77.65%, and 77.46%. The pore diameter distribution range

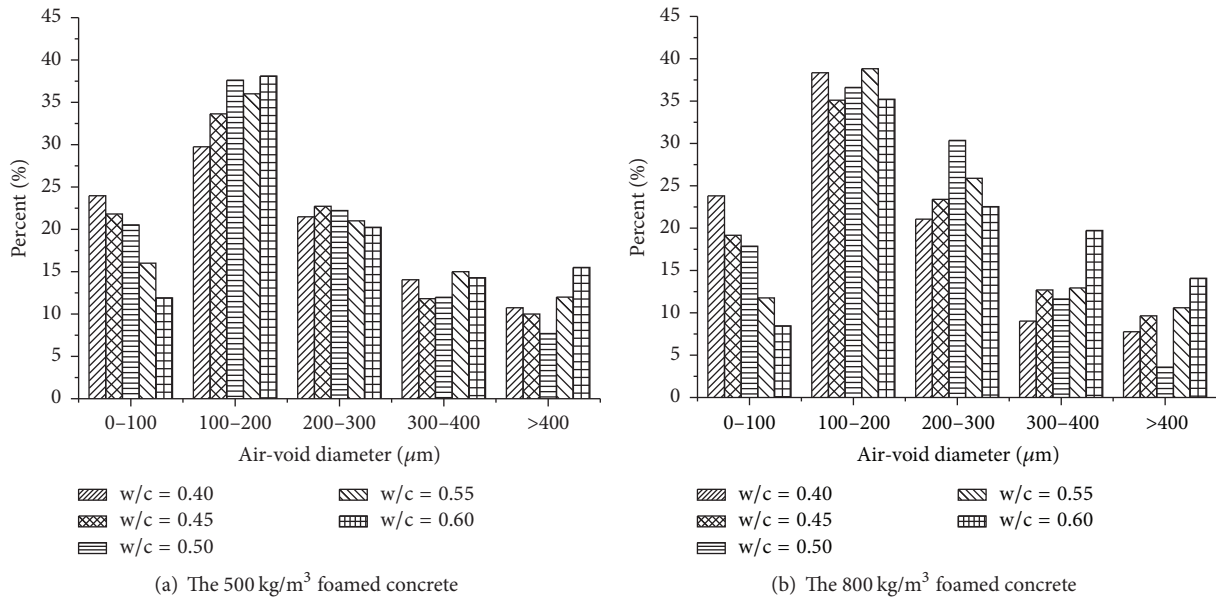


FIGURE 4: Effects of w/c ratio on the pore diameter distribution.

TABLE 4: Characteristics of air pores of the test specimens.

Specimens	Mean diameter (μm)	Average value of roundness
500-0.40	208.0	1.46
500-0.45	216.3	1.41
500-0.50	217.7	1.37
500-0.55	228.1	1.31
500-0.60	256.1	1.30
800-0.40	192.5	1.40
800-0.45	197.6	1.38
800-0.50	217.0	1.36
800-0.55	226.3	1.30
800-0.60	245.6	1.28

in the 800 kg/m^3 foam concrete was narrower than that of the 500 kg/m^3 foam concrete (Figure 4). Moreover, lower proportions of small and large pores were observed. These findings reveal the attributes not beneficial to the strength of the 800 kg/m^3 foam concrete compared with that of the 500 kg/m^3 foam concrete.

The effect of w/c ratio on the porosity of the 500 kg/m^3 foam concrete is illustrated in Figure 5(a). The open porosity of the 500-0.40, 500-0.45, 500-0.50, 500-0.55, and 500-0.60 samples decreased from 49.35% to 43.70% gradually, whereas the closed porosity increased from 28.90% to 34.36%. This finding can be explained by the following reasons. On one hand, the relative viscosity decreased and more bubbles combined with the increase in w/c ratio of the foam concrete, thus reducing the total bubble surface area. The cement paste on the bubble surface increased and the pore wall thickened accordingly, as manifested by the reduced open porosity and increased closed porosity. On the other hand, ion enrichment ensued during cement hydration; the solubilities of the

different ingredients and migration speeds of the ions differed from one another significantly. Generally, most of the Ca^{2+} , SO_4^{2-} , and Al^{3+} entered the solution and deposited around the bubbles. The higher w/c ratio provided conditions for the migration of Ca^{2+} , SO_4^{2-} , and Al^{3+} [26]. Consequently, calcium hydroxide and ettringite were enriched on the bubble surfaces and formed pore shells. The thickness of pore shells was positively correlated with w/c ratio [27]; hence, the open porosity reduced significantly, whereas the closed porosity increased substantially.

The effect of w/c ratio on the porosity of the 800 kg/m^3 foam concrete is shown in Figure 5(b). The open porosity of the 800-0.40, 800-0.45, 800-0.50, 800-0.55, and 800-0.60 samples decreased from 40.15% to 39.70% gradually, whereas the closed porosity increased from 22.92% to 24.08%. However, the variation was not as distinct as that of the 500 kg/m^3 foam concrete. This result is related to the thicker pore walls and fewer open pores in the 800 kg/m^3 foam concrete than in the 500 kg/m^3 sample. Therefore, pore walls may have thickened with the increase in w/c ratio. *With the increase in the w/c ratio, then free water evaporated and the amount of capillaries increased [28], which resulted in more capillaries in the 800 kg/m^3 foam concrete than in the 500 kg/m^3 sample, gradually decreasing the open porosity and incrementally augmenting the closed porosity.*

3.3. Effect of Pore Structure on the Mechanical Properties of Foam Concrete. The fitting relationships between the measured 28-day strength and dry density of foam concrete are shown in Figure 6. The power exponential relationships between 28-day strength and dry density varied with w/c ratio (0.4, 0.45, 0.5, 0.55, and 0.6).

The effect of w/c ratio on the strength of foam concrete is shown in Figure 7. With the increase in w/c ratio, the

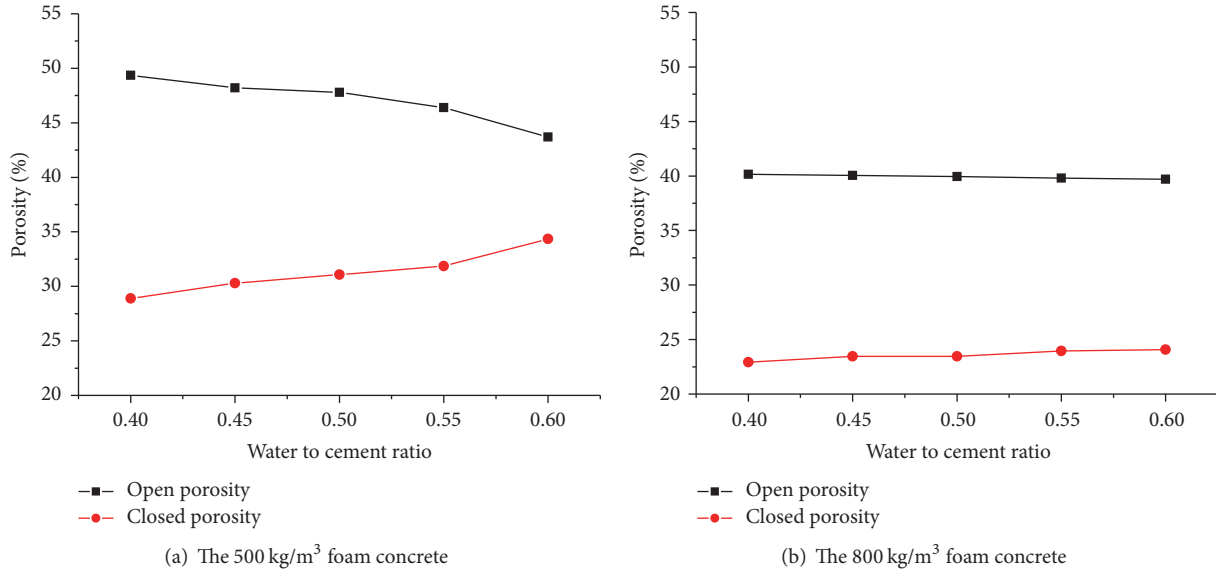


FIGURE 5: Effect of the w/c ratio on the porosity of the foam concrete.

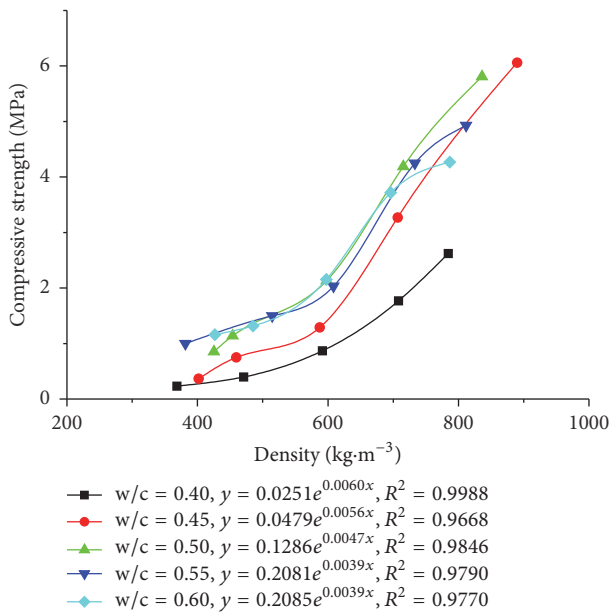


FIGURE 6: The fitting relationships between the strength and dry density of foam concrete.

compressive strength of foam concrete increased first and then decreased. This result was achieved because, on one hand, when the w/c ratio was smaller than the optimal ratio, a smaller w/c ratio generated higher proportions of small thin-walled, connected, and irregular pores. The strength of the foam concrete declined upon the stress concentration derived from external forces. On the other hand, the w/c ratio that exceeded the optimal level resulted in a weaker bubble-maintaining capability of the paste. Moreover, the bubbles in the paste easily combined during stirring and resulted in reduced pores, increased pore diameter, and uneven pore distribution. This occurrence would cause stress concentration,

and redundant free water would form capillary channels after the hydration reaction of cementing materials or evaporation, negating the compactness of the pore walls and consequently reducing the strength of the foam concrete.

Lower foam concrete dry density generated higher optimal w/c ratio (Figure 7). This finding may be explained by the notion that the lower foam concrete dry density was accompanied by a larger pore distribution range and higher proportions of small and large pores. Small and large pores can introduce defects, causing stress concentration. The defects introduced by small pores, such as connected pores and irregular pores, achieve more serious stress concentrations. Increasing w/c ratios can reduce the proportion of small pores effectively, thus enabling the reduction of stress concentration caused by open, connected, and irregular pores. The optimal w/c ratios of the prepared 400, 500, 600, 700, and 800 kg/m³ were 0.62, 0.59, 0.57, 0.55, and 0.53. The slump values of cement pastes were 215, 208, 204, 200, and 198 mm, respectively. We noted a linear relationship between dry density and the optimal w/c ratio expressed as $y = -0.0002x + 0.69$, where $R^2 = 0.991$.

4. Conclusions

- (1) Given the same density of foam concrete, a higher w/c ratio would result in a lower relative viscosity and a weaker bubble-maintaining capacity in cement paste. Moreover, bubbles more easily combine into larger ones. The proportion of small pores reduces, the average pore diameter increases, and the pores become increasingly round.
- (2) Given the same foam concrete w/c ratio, lower dry density would widen the pore diameter distribution range and increase the proportions of small and large pores.

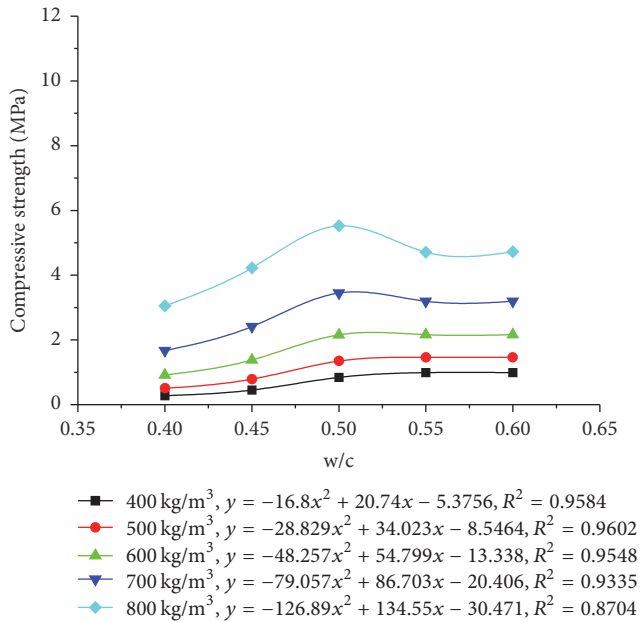


FIGURE 7: Effect of w/c ratio on the strength of foam concrete.

- (3) Water-cement ratio influences the size, shape, distribution, and connectivity of pores in foam concrete. The power exponential relationship between 28-day strength and dry density of the foam concrete varies with different w/c ratios.
- (4) A linear relationship exists between dry density and optimal w/c ratio expressed as $y = -0.0002x + 0.69$, where $R^2 = 0.991$. The optimal w/c ratios of the prepared 400, 500, 600, 700, and 800 kg/m³ were 0.62, 0.59, 0.57, 0.55, and 0.53, respectively.

Competing Interests

The authors declare that there is no conflict of interests regarding the publication of this paper.

Acknowledgments

The authors would like to acknowledge the support from the National Natural Science Foundation of China (no. 51372199).

References

- [1] Y. H. Mugahed Amran, N. Farzadnia, and A. A. Abang Ali, "Properties and applications of foamed concrete; a review," *Construction & Building Materials*, vol. 101, pp. 990–1005, 2015.
- [2] P. Chindapasirt and U. Rattanasak, "Shrinkage behavior of structural foam lightweight concrete containing glycol compounds and fly ash," *Materials and Design*, vol. 32, no. 2, pp. 723–727, 2011.
- [3] X. Chen, Y. Yan, Y. Liu, and Z. Hu, "Utilization of circulating fluidized bed fly ash for the preparation of foam concrete," *Construction & Building Materials*, vol. 54, pp. 137–146, 2014.
- [4] K. Jitchaiyaphum, T. Sinsiri, and P. Chindapasirt, "Cellular lightweight concrete containing pozzolan materials," *Procedia Engineering*, vol. 14, no. 11, pp. 1157–1164, 2011.
- [5] J.-Y. Wang, M.-H. Zhang, W. Li, K.-S. Chia, and R. J. Y. Liew, "Stability of cenospheres in lightweight cement composites in terms of alkali-silica reaction," *Cement & Concrete Research*, vol. 42, no. 5, pp. 721–727, 2012.
- [6] C. Hu, H. Li, Z. Liu, and Q. Wang, "Research on properties of foamed concrete reinforced with small sized glazed hollow beads," *Advances in Materials Science and Engineering*, vol. 2016, Article ID 5820870, 8 pages, 2016.
- [7] A. A. Sayadi, J. V. Tapia, T. R. Neitzert, and G. C. Clifton, "Effects of expanded polystyrene (EPS) particles on fire resistance, thermal conductivity and compressive strength of foamed concrete," *Construction and Building Materials*, vol. 112, pp. 716–724, 2016.
- [8] M. Y. J. Liu, U. J. Alengaram, M. Z. Jumaat, and K. H. Mo, "Evaluation of thermal conductivity, mechanical and transport properties of lightweight aggregate foamed geopolymer concrete," *Energy & Buildings*, vol. 72, pp. 238–245, 2014.
- [9] U. Johnson Alengaram, B. A. Al Muhit, M. Z. bin Jumaat, and M. L. Y. Jing, "A comparison of the thermal conductivity of oil palm shell foamed concrete with conventional materials," *Materials & Design*, vol. 51, pp. 522–529, 2013.
- [10] Z. Zhang, J. L. Provis, A. Reid, and H. Wang, "Mechanical, thermal insulation, thermal resistance and acoustic absorption properties of geopolymer foam concrete," *Cement & Concrete Composites*, vol. 62, pp. 97–105, 2015.
- [11] S. Wei, C. Yiqiang, Z. Yunsheng, and M. R. Jones, "Characterization and simulation of microstructure and thermal properties of foamed concrete," *Construction & Building Materials*, vol. 47, no. 10, pp. 1278–1291, 2013.
- [12] G.-C. Sang, Y.-Y. Zhu, G. Yang, and H.-B. Zhuang, "Influence of water-cement ratio on property of light weight cement based foam material," *Journal of Materials Science and Engineering*, vol. 33, no. 3, pp. 339–342, 2015.
- [13] J. Jiang, Z. Lu, Y. Niu, J. Li, and Y. Zhang, "Study on the preparation and properties of high-porosity foamed concretes based on ordinary Portland cement," *Materials & Design*, vol. 92, pp. 949–959, 2016.
- [14] G. Sang, Y. Zhu, G. Yang, and H. Zhang, "Preparation and characterization of high porosity cement-based foam material," *Construction & Building Materials*, vol. 91, pp. 133–137, 2015.
- [15] T.-H. Wee, S. B. Daneti, and T. Tamilselvan, "Effect of w/c ratio on air-void system of foamed concrete and their influence on mechanical properties," *Magazine of Concrete Research*, vol. 63, no. 8, pp. 583–595, 2011.
- [16] C. Krämer, M. Schauerte, T. L. Kowald, and R. H. F. Trettin, "Three-phase-foams for foam concrete application," *Materials Characterization*, vol. 102, pp. 173–179, 2015.
- [17] C. Krämer, T. L. Kowald, and R. H. F. Trettin, "Pozzolanic hardened three-phase-foams," *Cement & Concrete Composites*, vol. 62, pp. 44–51, 2015.
- [18] M. T. Ley, R. Chancey, M. C. G. Juenger, and K. J. Folliard, "The physical and chemical characteristics of the shell of air-entrained bubbles in cement paste," *Cement & Concrete Research*, vol. 39, no. 5, pp. 417–425, 2009.
- [19] A. A. Hilal, N. H. Thom, and A. R. Dawson, "On entrained pore size distribution of foamed concrete," *Construction & Building Materials*, vol. 75, pp. 227–233, 2015.

- [20] A. A. Hilal, N. H. Thom, and A. R. Dawson, "On void structure and strength of foamed concrete made without/with additives," *Construction & Building Materials*, vol. 85, pp. 157–164, 2015.
- [21] K. Yang and K. Lee, "Tests on alkali-activated slag foamed concrete with various water-binder ratios and substitution levels of fly ash," *Journal of Building Construction & Planning Research*, vol. 1, no. 1, pp. 8–14, 2013.
- [22] S. Wei, Z. Yunsheng, and M. R. Jones, "Using the ultrasonic wave transmission method to study the setting behavior of foamed concrete," *Construction & Building Materials*, vol. 51, no. 51, pp. 62–74, 2014.
- [23] A. K. H. Kwan, W. W. S. Fung, and H. H. C. Wong, "Water film thickness, flowability and rheology of cement–sand mortar," *Advances in Cement Research*, vol. 22, no. 1, pp. 3–14, 2010.
- [24] Z. Qian, L. Li, Z. Gao, and F. Hu, "Research on the effect of different superplasticizers on the properties of foam concrete," *Coal Ash*, no. 6, pp. 44–46, 2014.
- [25] M. Zhu, F.-G. Wang, X.-L. Zhang, and F.-Z. Wang, "Research on the relationship between pore structure and thermal conductivity of foamed concrete," *Journal of Wuhan University of Technology*, vol. 35, no. 3, pp. 20–25, 2013.
- [26] L. Wang, Y. Chen, and G. Du, "Influence mechanism of microstructure of foam concrete on macroscopic properties," *China Powder Science and Technology*, vol. 21, no. 5, pp. 63–68, 2015.
- [27] Y. Xie, D. J. Corr, F. Jin, H. Zhou, and S. P. Shah, "Experimental study of the interfacial transition zone (ITZ) of model rock-filled concrete (RFC)," *Cement & Concrete Composites*, vol. 55, pp. 223–231, 2015.
- [28] X. Li, M. Liu, B. Ma, S. Jian, L. Su, and Z. Zhao, "Influence of pore structure on foam concrete and controlling method," *Materials Review*, vol. 26, no. 4, pp. 141–144, 2012.